Spatial organization and dynamics of multiple DNA molecules confined in a nanofluidic cavity

Zezhou Liu

Supervised by Dr. Walter Reisner

Doctor of Philosophy

Department of Physics

McGill University, Montreal

A Dissertation Submitted to the Faculty of Graduate Studies in Partial

Fulfillment of the Requirements for the Degree of Doctor of Philosophy

Abstract

The mechanisms of bacterial chromosome segregation and plasmid partitioning are among the most intriguing phenomena in cells. In the past decades, phase transition based phenomena have gained great appreciation for being a potential driving force for chromosome segregation and plasmid partitioning. In particular, DNA chains are predicted to demix depending on the aspect ratio of the confinement geometry. While recent Monte Carlo and molecular dynamics simulations have provided insights into this phenomenon and its connection to bacterial systems, fundamental questions such as the spatial distribution of the segregated chains, the role of the confinement geometry and the dynamics of the chains remain elusive. In this thesis, we develop a nanofluidic device as an artificial model to quantify the interaction of multiple double-stranded DNA (dsDNA) molecules in a cavity with controlled geometry. We demonstrate that two DNA chains of equal size segregate spontaneously when confined in the cavity. These two chains occupy different poles as the cavity aspect ratio increases. We also show that when a plasmid is confined with a large dsDNA in an anisotropic cavity (T_4-DNA), the plasmid adopts an annular distribution with a preference for the poles. We propose that the non-uniform plasmid distribution can be explained if the plasmid is postulated to undergo Brownian diffusion on a free energy landscape composed of wall repulsion and volume exclusion with the large DNA molecule. Finally, we generalize our two-chain experiments to three chains, introducing an additional plasmid into the nanocavity along with the large DNA and the single plasmid. We find that the plasmid distribution becomes more uniform as the

plasmid number increases, resulting from the repulsive interaction between plasmids. In the absence of the large DNA, the plasmid distribution shifts from being uniform to slightly annular due to the effect of depletion interactions induced by the plasmids with respect to each other. We observe that in a square cavity, plasmids tend to accumulate at the cavity corners, suggesting plasmid clusters in bacteria may form near boundaries with greater curvature. Finally, we propose a general formalism–the transition matrix method–to quantify the dynamics systematically given a certain specified degree of system coarse graining.

Abrégé

Les mécanismes de ségrégation des chromosomes bactériens et de partitionnement des plasmides sont parmi les phénomènes cellulaires les plus intrigants. Au cours des dernières décennies, les phénomènes basés sur la transition de phase ont acquis une grande appréciation en tant que force motrice potentielle pour la ségrégation des chromosomes et la partition des plasmides. En particulier, il est supposé que les chaînes d'ADN se démixent en fonction du rapport d'aspect de la géométrie de confinement. Alors que de récentes simulations de Monte Carlo ont fourni des informations sur ce phénomène et sa connexion aux systèmes bactériens, des questions fondamentales telles que la distribution spatiale des chaînes ségrégées, le rôle de la géométrie de confinement et la dynamique des chaînes restent élusives. Dans cette thèse, nous développons un dispositif nanofluidique comme modèle artificiel pour quantifier l'interaction de plusieurs molécules d'ADNdb dans une cavité à géométrie contrôlée. Nous démontrons que deux chaînes d'ADN de taille égale se séparent spontanément lorsqu'elles sont confinées dans la cavité. Ces deux chaînes occupent des pôles différents à mesure que le rapport d'aspect de la cavité augmente. Nous montrons également que lorsqu'un plasmide est confiné avec une large molécule d'ADNdb dans une cavité anisotrope (T_4 ADN), le plasmide adopte une distribution annulaire avec une préférence pour les pôles. Nous proposons que la distribution plasmidique non uniforme peut être expliquée si le plasmide subit une diffusion brownienne sur un paysage d'énergie libre composé de répulsion de paroi et d'exclusion de volume avec la grande molécule d'ADN. Enfin, nous généralisons nos expériences avec deux

chaînes à trois chaînes, en introduisant un plasmide supplémentaire dans la nanocavité avec le grand ADN et le premier plasmide. Nous constatons que la distribution des plasmides devient plus uniforme à mesure que le nombre de plasmides augmente, résultant de l'interaction répulsive entre les plasmides. En l'absence du gros ADN, la distribution des plasmides passe d'uniforme à légèrement annulaire en raison de l'effet des interactions de déplétion induites par les plasmides les uns par rapport aux autres. Nous observons que dans une cavité carrée, les plasmides ont tendance à s'accumuler aux coins de la cavité, ce qui suggère que des amas de plasmides dans les bactéries peuvent se former près des régions de frontière cellulaire avec une plus grande courbure. Enfin, nous proposons un formalisme général–la méthode des matrices de transition–pour quantifier systématiquement la dynamique pour un certain degré spécifié d'approximation du système.

Acknowledgements

This work would not have been possible without the help of many people. First and foremost, I would like to thank my supervisor, Prof. Walter Reisner, for his exceptional supervision and his many insightful suggestions. He guided me through my Ph.D. study as a supervisor, and also as a great colleague who encourages me all the time. I will be grateful to Prof. Reisner for the rest of my life.

I thank Prof. Rodrigo Reyes-Lammothe in the department of biology at McGill University, for helping me apply the knowledge we learned from physics to biology.

I thank Xavier Capaldi, a member of our group, for many days of working together in the cleanroom, many insightful discussions on research ideas, many chill afternoon coffee breaks, and too many memories to list them all.

I thank Yuning Zhang, a former member of our group, for providing me with many invaluable suggestions and help in both work and life.

I thank Seyed Imman Isaac Hosseini and Lili Zeng, for discussing the DNA confinement experiment and data analysis ideas. I appreciate all the help.

I thank all other members of the Reisner group, former or current, for providing me so much help during my Ph.D. study.

I thank all McGill Nanotools staff, who trained and helped me countless times with the micro/nanofabrication tools.

I thank all staff of LMN at INRS, who guided me on the device fabrication.

I thank all my doctoral committee members, who devoted their precious time and energy to my dissertation.

I thank all my friends, from whom I received so much support.

Lastly, I profoundly thank my wife and my eternal love, Hang Li, for these years of love and support.

Contribution to original knowledge

In this doctoral thesis, my key contribution is to develop a nanofluidic system that allows us to trap multiple polymer chains in an isolated cavity with variable anisotropy and use this system to quantify the interactions of the multiple confined chains. The dissertation is written in manuscript based format, including two manuscripts (one published and one ready for submission).

Chapter 1–a general introduction with motivations.

Chapter 2–background related to the manuscripts.

Chapter 3–construction of the nanofluidic device and related works.

Chapter 4–a published manuscript on DNA chains confined in a nanofluidic cavity.

Confinement anisotropy drives polar organization of two DNA molecules interacting in a nanoscale cavity Zezhou Liu, Xavier Capaldi, Lili Zeng, Yuning Zhang, Rodrigo Reyes-Lamothe & Walter Reisner. *Nature Communications 13, 4358 (2022)*

Chapter 5–a manuscript on multiple DNA chains confined in a nanofluidic cavity for ready submission.

Multiple Polymer Chains Confined in a Nanoscale Cavity: How Entropic Forces Alter Plasmid Dynamics Zezhou Liu, Sarah Christensen, Xavier Capaldi, Rodrigo Reyes-Lamothe & Walter Reisner. *ready for submission*

Chapter 6–conclusion and discussion

The first manuscript in this dissertation provides a pathway to isolate the role of entropy in bacterial chromosome segregation and plasmid segregation, and how the con-

finement anisotropy alters the system configuration. Z. Liu and W. Reisner conceived the idea. Z. Liu and X. Capaldi fabricated the chips. Z. Liu performed the simulation with L. Zeng's help. Z. Liu designed and conducted the experiments with Y. Zhang's help. R. R. Lamothe assisted in the project/experiment design. Z. Liu performed the data analysis. Z. Liu and W. Reisner wrote and revised the manuscript. W. Reisner and Z. Liu managed the project. All authors contributed to discussions and paper revisions.

The second manuscript extends the first manuscript in two ways: (1) explore the effect of adding additional plasmids to the cavity system and (2) the effect of adding variable pole curvature. Z. Liu and W. Reisner conceived the idea. Z. Liu and X. Capaldi fabricated the chips. Z. Liu and S. Christensen conducted the experiments. Z. Liu performed the simulation. R. R. Lamothe assisted in the project/experiment design. Z. Liu performed the data analysis. Z. Liu and W. Reisner wrote and revised the manuscript. W. Reisner and Z. Liu managed the project. All authors contributed to discussions.

Table of Contents

List of Figures

Chapter 1

INTRODUCTION

1.1 Introduction

Since the concept of entropy was introduced in the early 19^{th} century, numerous spontaneous phenomena, such as binary separation and mixing of polymer solutions [1] and the isotropic-nematic phase transition of a liquid crystal [2], are understood to arise from entropy. The binary phase separation of the polymer system arises from the reduction of the entropy gain from chain connectivity, and the liquid crystal phase transition is related to the excluded volume of the constituent rod-like molecules, leading to a counter-intuitive apparent entropically favourable increase in system organization.

Biological systems also exploit phase separation physics to maintain their proper functioning. Liquid-liquid phase separation occurs when a liquid of uniform composition demixes into two liquid phases. Theoretical and experimental studies have shown evidence for liquid-liquid phase separation in several materials, such as supercooled water [3, 4, 5], liquid carbon [6] and liquid phosphorus [7]. In biological systems, the demixing of liquid-disordered phase and liquid-ordered phase lipids are observed in cellular lipid membranes across a wide range of compositions and temperatures [8]. Liquid-liquid phase transitions are believed to drive the formation of membrane-less organelles, such

as P granules [9]. Liquid-liquid phase separation may also account for reducing the noise of protein expression in cells by forming heterogeneous regions [10]. In those cases, phase separation is induced by numerous small molecules and the weak interaction between them.

Phase separation can also be induced by the interaction of larger but less numerous dsDNA polymer molecules. Theoretical studies suggest that the segregation of bacterial chromosomes may be driven by the entropic demixing of replicated dsDNA molecules [11]. Multiple dsDNA molecules may adopt mixed or demixed phases depending on the confining geometry [12]. In vivo observation shows that small circular plasmids adopt an uneven distribution in bacterial cells [13]. The formation of the plasmid favourable regions may be attributed to the phase separation of the biological system.

This dissertation presents two closely related experimental projects that explore the mixing and demixing dynamics of multiple polymer molecules confined in a model nanofluidic system consisting of a single nanocavity. The first project focuses on how the confinement geometry–specifically the anisotropy of the confinement–alters a system consisting of two polymer chains. The second project generalizes the two-chain system to a multi-chain system and presents a new approach, the state transition matrix method, for analyzing the dynamics of the multi-chain interaction. Chapter 1 provides a general introduction to the topic including a detailed motivation for the project. Chapter 2 reviews the background relevant to the related polymer physics models. Chapter 3 introduces the nanofluidic confinement chips and the microscopy setup used in the experiments. Chapter 4 presents the results and discussion of the two dsDNA molecules in anisotropic confinement experiments. Chapter 5 presents the results and discussion of the multiple dsDNA confinement experiments. Chapter 6 summarizes the results and provides a future perspective.

This introductory chapter introduces the fundamental problem of polymer entropic segregation under confinement and provides examples of biological systems that may

exploit entropic segregation. Examples of polymer phase separation in both soft-matter and biological systems are discussed, focusing in particular on the role of confinement geometry anisotropy in modulating the propensity of polymers to segregate. We also introduce the concept of transverse trapping nanofluidics, the experimental system used to perform our study of multiple polymer confinement.

1.2 Entropic force in polymer physics: mixing vs demixing

Polymer phase separation is the spontaneous formation of two distinct phases from a homogeneous polymer mixture. The internal energy balances the entropy of the system, causing the system to spontaneously transit to a configuration with minimal free energy. Polymer phase separation has been studied extensively in various contexts, for example, polymer solutions, polymer blends [14, 1] and biological systems [15]. In these examples, numerous small polymer molecules with short-range interactions are involved.

Polymer phase separation can also be observed in systems with less numerous but longer polymer chains. While entropy maximization favours the mixing of small polymer chains in the absence of attractive interactions [14], entropy maximization can favour the demixing of long polymer chains due to the large excluded-volume of one chain with respect to the other. This entropic demixing effect is more pronounced in anisotropic (tube-like) confinement. To appreciate why excluded-volume has such a strong effect, we introduce the concept of blobs. A blob is a coarse-grained structure containing segments that maintain the same size scaling as the bulk chain. In essence, within a blob the scaling of coil spatial extension with segment number is indistinguishable from that of the bulk chain; for scales above the blob scale, departures from bulk behaviour can be observed (e.g. due to confinement, presence of neighbouring chains). Let the scale ξ characterize the 'blob' scale. The bulk chain performs a self-avoiding walk so that $\xi \sim a g_b^{\nu}$ where a is the size of a monomer, g_b is the number of monomers in a blob and $\nu = 3/(2+d)$ is

the Flory exponent and d is the number of dimensions (note $\nu = 3/5$ in 3D). As a classic example of the power of the blob concept, the blob argument can be used to deduce the scaling law for the extension of a self-avoiding chain in a channel (due to de Gennes) [1, 16]. We imagine that the conformation of a confined chain corresponds to a string of blobs, with the blob scale $\xi \sim D$ where D is the channel diameter (of course each blob must fit within the channel). This leads to $g_b \sim \left(\frac{\xi}{a}\right)^{1/\nu} = \left(\frac{\xi}{a}\right)^{\frac{5}{3}}$. We expect the extension of the chain along the channel is just proportional to the extent of each blob times the total number of blobs, or $R \sim D(\frac{N}{g_b}) \sim Na\left(\frac{a}{D}\right)^{\frac{2}{3}}$.

We now use the blob concept to explain why chains segregate in anisotropic confinement. We do this by calculating the free energy difference between two chains that are segregated and two chains that overlap in a cylindrical tube of diameter D with open ends. First, note each blob has a free energy on the order of k_BT. When the two chains are segregated (see Fig. 1.1a), the confinement free energy of the two-chain system is $F_{\text{seg}}/k_BT \sim \frac{N}{g_b} \sim N(\frac{D}{a})^{-1/\nu} \sim (\frac{R}{R_F})^{1/(1-\nu)}$, where N is the number of monomers in the chain, R_F is the flory radius of the chain (proportional to the chain size). For the mixing case (see Fig. 1.1b), the size of the blob decreases, leading to an increase of the number of blobs. The diameter of the blob is $D_{\text{eff}} = D/\sqrt{2}$, as each chain can be viewed as trapped in a smaller imaginary cylinder. The choice of $\sqrt{2}$ accounts for the fact that each chain occupies $1/2$ the cross-sectional area of the original channel [17]. The mixing free energy F_{mix} can thus be calculated as twice that of a chain trapped in the reduced diameter tube; the segregated free energy F_{seg} is twice that of one of the chains trapped in a tube of diameter D. This leads to $F_{\text{mix}} = 2^{1/2\nu}F_{\text{seg}}$ [11], so that the free energy of the mixed configuration is greater than the free energy of the segregated configuration and the mixed configuration is disfavored. Note that this picture assumes the confined chains have linear ordering. Polson et al.[18] verified that this scaling model qualitatively gives the free energy difference between mixing and demixing via molecular dynamics simulation. As the aspect ratio of the cylindrical confinement decreases, the free energy penalty from mixing de-

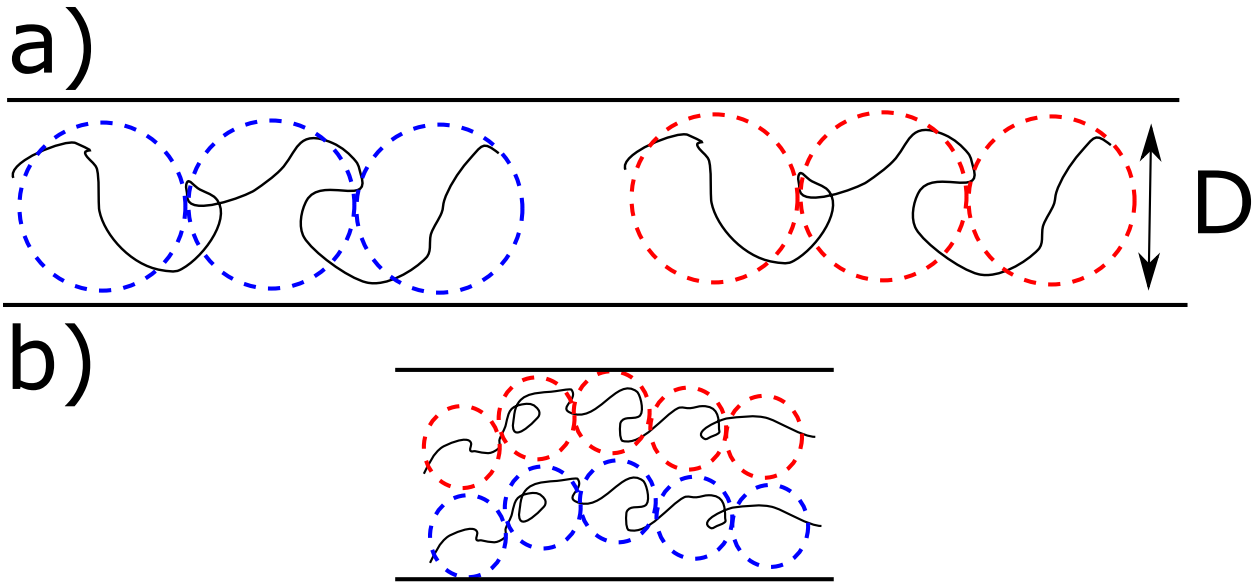

Figure 1.1: Schematic of mixed and segregated polymer chains. a) Segregated polymer chains. b) Mixed polymer chains.

creases. In spherical confinement, the two-chain system is predicted to have the same free energy for both the mixed and the demixed configuration [19].

1.3 Entropic force in biological systems: chromosome segregation and plasmid localization

Bacterial systems contain many large dsDNA molecules (primary/secondary chromosomes [20], plasmids [21]). Bacteria lack a nucleus so these molecules interact within the confined cell volume. Note that while the well-studied *E. coli* system has a rod-like cell geometry, bacteria can adopt a wide-range of cell geometries [22], including ovid/spherical (cocci), spiral and even square-shaped (as in *H.walsbyi* [23], an archea that is found worldwide in brine pools). The soft-matter problem of how multiple confined polymers interact in a space of varying anisotropy is thus highly relevant to understanding how bacteria organize their interiors. Below we discuss two specific problems in depth, chromosome segregation and plasmid partitioning.

Despite extensive study, the mechanisms of chromosome segregation and partitioning are still among the most mysterious phenomena in biology. The model bacterial system, *Escherichia coli*, contains a single ring-shape chromosome packaged inside a rod-like cell shape. The chromosome is segregated and partitioned in a coordinated fashion with the cell division cycle. The chromosome replication starts from the origin of replication (*ori*), and the two replicated forks end at the terminus (*ter*) symmetrically opposite *ori*. The replicated chromosomes segregate and partition into the divided cells during the chromosome replication process [24, 25]. Two types of mechanisms might be responsible for the synchronized replication and partition: 1) active partition mechanisms relying on specific proteins and organelles by consuming energy from ATP and 2) passive partition mechanisms arising from entropy. Typically, an active partition system consists of two proteins and one or more partition sites on a chromosome. One of those proteins is anchored at the cell pole and they bind to a specific DNA site (partition site in this case) to prevent chromosomes from moving to undesired locations. The second protein (an ATPase or GTPase protein) uses energy to move chromosomes to promote partitioning. Partition loci of *E. coli* and *Bacillus subtilis* have been visualized [26, 27]. However, the first type of mechanism faces difficulty in explaining the drastic size difference between the chromosomes and the proteins. The stretched length of the chromosome from a lysed *E. coli* cell can easily be 1000 times of the cell size ($\sim 1\,\mu$m) [24]. Replication related proteins and anchor structures, however, usually have a size on the order of 10 nm [24]. This order of magnitude size difference between proteins and chromosomes makes it difficult to understand how the replication proteins and anchor proteins unwind, move and bind a very specific site of the chromosome with reasonable time scale and energy consumption. The second type of mechanism involves spontaneously demixing and partitioning chromosomes in different daughter cells with minimum metabolism cost. However, several fundamental questions remain to justify the existence and the role of this type of mechanism. Chromosomes do not constitute simple swollen random coils [28]. A bacterial chromosome is

a several Mbp size circular molecule condensed 1000-fold into a structure known as the nucleoid. The bacterial chromosome appears as a radially confined helical fiber with a longitudinal extent less than the overall bacterial length. At the most basic level, the bacterial chromosome is organized into topologically insulated supercoiled domains around 10-100 kbp. These domains are further stabilized and condensed by a family of nucleoid associated proteins (NAPs) that introduce bending and cross-linkages. The domains appear as plectonemically looped "bristles" emerging from a dense chromosomal core [29]. The nucleoid is further compacted by molecular crowding–small macromolecules such as proteins and lipids–inducing attractive depletion forces within the chromosome [30]. In a polymer physics description, the chromosome is coarse-grained into spherical units with size defined by the topologically insulated domain. The detailed chromosomal local structures do NOT alter the global conformation of the chromosome. Given the structural complexity of chromosomes and the prescription of polymer physics, it is reasonable to ask: will replicated chromosomes mix or demix in a cell-like confinement space? If the chromosomes demix, how is the global organization of the two demixed chromosomes controlled by the cell? What is the relative contribution of the active mechanism and the passive mechanism? These remaining questions make the entropic segregation mechanism still controversial among biologists.

Plasmids–small circular DNAs commonly found in bacteria–contain genes that are critical for cell metabolism, pathogenesis and evolution [21]. While plasmids replicate and partition autonomously, plasmids are still able to maintain a stable inheritance in the offspring cells. Depending on the copy number, plasmids have evolved different partition mechanisms to achieve inheritance stability. Low copy number plasmids (lcn plasmids)–plasmids that only have a few copies in a cell–have encoded partition (*par*) system that actively moves plasmids to both halves of the diving poles, reducing the randomness from the thermal fluctuations [31]. High copy number plasmids (hcn plasmids) usually have tens or even hundreds of copies in a bacteria cell. So far, it is generally believed that

hcn plasmids partition randomly (binomial) due to lack of the *par* system and the large number of copies. Studies [32, 13, 33], however, have shown that the spatial distribution of the hcn plasmids is non-uniform. Some copies of hcn plasmids diffuse randomly while many remain clustered in the nucleoid-free regions. The non-uniform distribution of the plasmids is closely related to the plasmid partitioning and the stability of the plasmid inheritance [34]. To expand on this point, if the hcn plasmids were perfectly uniformly distributed and randomly partitioned, this would lead to a loss rate–the probability of forming a plasmid-less cell per cell per generation–smaller than 10^{-6}, given there are more than 10 copies of plasmids at the time of division [35, 36]. In contrast, the experimental work [37] measures a higher loss rate between 10^{-2} and 10^{-5}. They attribute the instability of certain ColE1-derivative plasmids to multimerization (clustering), suggesting the non-uniform distribution of the hcn plasmids affects the partitioning. The spatial distribution of plasmids at the time of division also affect the partitioning. Plasmids that are closer to a given pole have higher probability to be partitioned into the daughter cell containing this pole than the daughter cell containing the other pole [21].

The uneven hcn plasmid distributions share certain patterns. The radial distribution of the plasmid fluorescent signal shows that the plasmid distribution has a donut shape, indicating that the hcn plasmids are mainly located outside the nucleoid at the inner periphery of the bacteria as either clustered aggregates or as freely diffusing single copies [13]. Besides the donut-like distribution, a pole preference of the plasmids is observed in *E. coli* [32]. However, the mechanism behind the plasmid periphery distribution, pole preference and the formation of clustering remain unclear.

The aforementioned questions regarding chromosome segregation and plasmid localization may be answered from the entropy perspective. For chromosome partitioning, numerical studies [19, 38] have revealed that multiple self-avoiding chains will demix spontaneously in an elongated confinement geometry. This spontaneous demixing can aid chromosome segregation without increasing the metabolite burden. Note the geome-

try, especially the aspect ratio, of the confinement can directly affect the demixing. In vivo studies [39, 40] altered the geometry of the bacteria via a microfluidic chip and they find the elongated cell geometry promotes the chromosome segregation. The scaling based phase diagram of two-chain demixing parametrized by the chain concentration and geometry aspect ratio is famously proposed and verified numerically. [12, 41, 38, 42]. For plasmid partitioning, the exclusion between the plasmid and the nucleoid has been suggested as the potential mechanism leading to the plasmid non-uniform distribution [43, 13, 32]. Plasmids are expected to localize to the nucleoid free region which potentially gives the donut-like distribution observed in vivo.

While the idea that chromosome segregation and plasmid localization may be related to entropy is not new, there are considerable challenges in experimentally testing the physical mechanism in biological systems due to their immense complexity. In bacteria, a vast number of molecular processes overlap in time and it is impossible independently control physically essential system parameters without drastically altering cellular phenotype and functionality (for example the geometry of the bacteria or the background crowder concentration). Biology has classically taken a "top-down" approach, creating mutants with single-gene "knock-outs" and observing the effect on organism function. This approach is very powerful, but may obscure underlying biological mechanisms that have a strong physical and global character, involving the coordinated interaction of many molecules or large macromolecular complexes across the cell. A physical approach is to develop a "minimal model" that isolates components involved in the partitioning process. In particular, a minimal model is simple enough that it can be explored over a large parameter space, much larger than is possible from the study of in vivo systems that might occupy only a few distinct points in parameter space. While a minimal model may well fail to account for the observed phenomena, it is still successful if it establishes an effective physical baseline. This baseline can then clarify the role of any complementary active mechanisms (e.g. ATP-driven) that entail metabolic cost.

1.4 A nanofluidic device for biopolymer confinement and analysis

The field of nanofluidics has been extensively developed over the past two decades. Sub-100 nm features, such as nanochannels and nanocavities, can be written by ebeam lithography in parallel and transferred to substrate materials reliably via reactive ion etching (RIE). The high precision and high yield achieved via parallel processing of nanofluidic features enable nanofluidic devices to perform single molecule level analysis in parallel over large molecular ensembles.

Over the past two decades, great effort has been devoted to developing platforms allowing single molecule level manipulation. Nanochannels with widths ranging from ~ 30 nm to $\sim 1\,\mu$m and lengths in hundreds of microns have been used to trap and linearize DNA to nearly their full extension [44, 45, 46, 47]. Denatured DNA chains can be optically barcoded when a sequence specific stain is applied to the chain [48]. Nanochannel arrays potentially allow high-throughput DNA barcoding in a lab-on-chip system. Nanopores are another powerful technology allowing single molecule level sensing. Nanopores are small holes with an internal diameter usually in sub 10 nm scale. A single DNA chain can be threaded through the pore by applying trans-pore electric field. The DNA chain is partially confined inside the pore, creating a blockage of the ionic current signal that gives the molecular conformation and structural information [49, 50]. In these technologies, a single DNA chain is targeted as the confinement features are not completely isolated from the environment.

Confinement approaches that achieve complete isolation are critical to study chromosome segregation and plasmid partition in a cell-like confinement geometry. When multiple chains are introduced in a structure with open ends, for example, nanochannels or nanopores, the strong exclusion between the DNA chains inhibits configurations that remain in close proximity [1, 16]. The DNA chains can escape the confinement and dif-

fuse into the bulk solution. A mechanism based on mechanical actuation is one pathway to achieve such complete confinement. After introducing multiple chains into the confinement feature, the "gate" can be actively closed and chains are forced to remain close together. Unger Ma *et al.* developed a polydimethylsiloxane (PDMS) based microfluidics valve to control the fluid flow [51]. The ceiling of the PDMS made microfluidic channels are deflected pneumatically and the channels are sealed mechanically. Convex lens-induced confinement (CLIC) applies mechanical force to a cover glass via a piezoelectric controlled pushing lens. The thin cover glass is deflected and confines DNA chain in a slit-like confinement with sub-5 nm thickness. Various confinement features can be etched in the slit region [52]. The dimple machine is a related approach that applies negative pressure (vacuum) to a PDMS bonded fluidic cell to actuate and seal off confined cavities [53].

In chapter 3, we introduce a nanofluidic platform that utilizes pneumatic deflection of a thin bonding lid to confine multiple chains to a small cavity (see Fig. 3.4). We use LPCVD silicon nitride membrane–a thin, chemically stable and pinhole-less material–to perform actuation instead of PDMS and cover glass (see Fig. 3.4a, b). The use of a nitride membrane minimizes the liquid evaporation and false sealing of the compartments commonly reported from the PDMS and glass based actuation device. The nitride membrane lid is deflected downward when pressure is applied to seal off the cavities (see Fig. 3.4c). In principle, our nanofluidic chip allows us exploring DNA chains under different confinement geometries, i.e. the nanochannel confinement, the nanoslit confinement and the nanocavity confinement (see Fig. 3.4d). This nitride based confinement device is used to carry out all experiments exploring polymer chain interactions covered in this thesis.

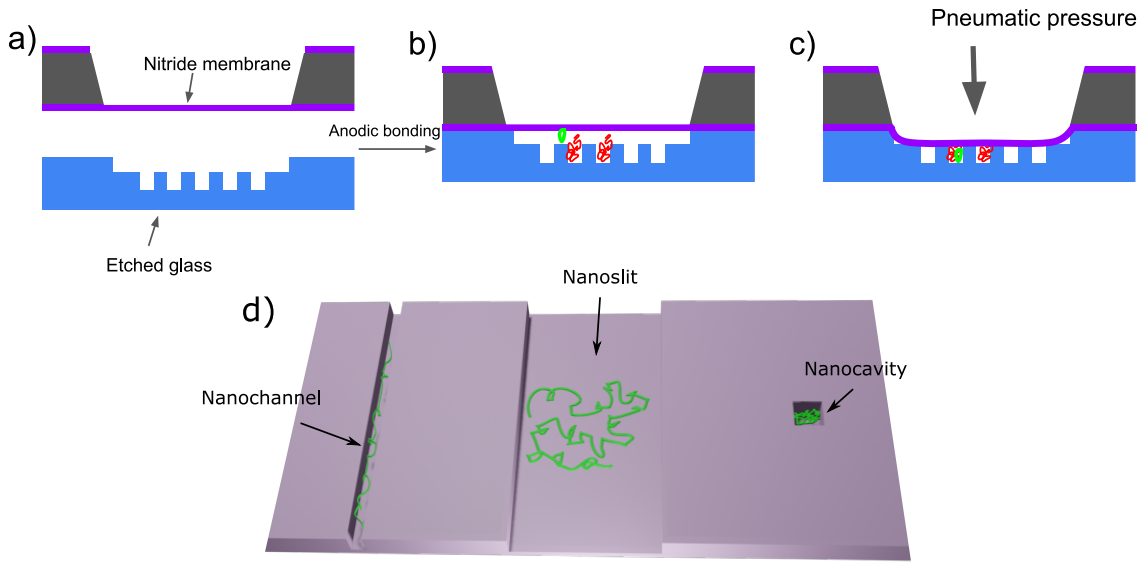

Figure 1.2: Schematic of the nanofluidic platform. a) A silicon frame with free standing silicon nitride membrane and an etched glass bottom substrate. Nanoscale features are defined by EBL and transferred to glass via RIE. The free standing membrane constituting the lid is used to seal off and isolate the nanofluidic features. b) An anodically bonded device. Differentially stained DNA chains are introduced into the trapping region. c) The membrane lid is deflected downward to seal the nanofluidic features. d) Illustrations of a nanoslit, a nanochannel and a nanocavity.

Chapter 2

BACKGROUND

2.1 Properties of DNA chains

DNA has long been used as a model semiflexible polymer in polymer confinement experiments [54]. A semiflexible chain is rigid at very short length scales and flexible at larger scales where the chain coils into a random-walk configuration. The persistence length gives the scale at which the chain begins to coil appreciably. A semiflexible polymer chain can be approximately described as a chain of "rods", as in Fig. 2.1, with each rod one Kuhn length long (with one Kuhn length equal to twice the persistence length). DNA chains explore different conformations depending on the confinement geometry. The chain conformation can be described by key physical parameters, in particular the chain contour length (L), the persistence length (P) and the effective width (w) which we briefly review.

The *contour length* L is the full length of a DNA stretched end-to-end. The contour length is simply the product of the number of base pairs of the DNA molecule with the length of a base pair. The average length of a base pair in B-state double-stranded DNA is 0.34 nm [55]. The contour length of the DNA can be much larger than the cell/virus containing it. For example, λ phage packages DNA, which is commonly used in polymer

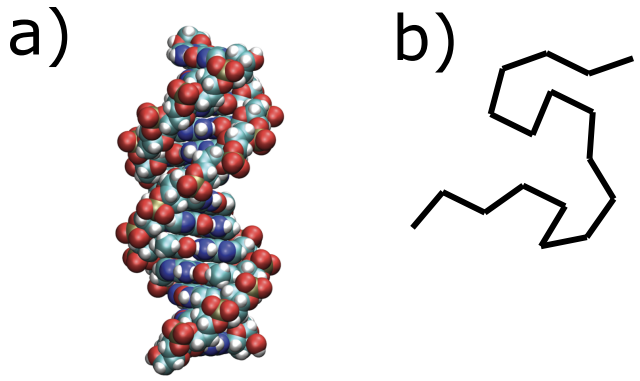

Figure 2.1: Schematic of a semiflexible DNA chain. a) The DNA chain with atomistic details. b) The coarse-grained DNA chain with the semiflexible chain model. Adapted with permission from *Assenza, Salvatore, and Rubén Pérez. "Accurate Sequence-Dependent Coarse-Grained Model for Conformational and Elastic Properties of Double-Stranded DNA." Journal of chemical theory and computation 18.5 (2022): 3239-3256.*. Copyright 2022 American Chemical Society.

confinement experiments, with a contour length 16.5 μm, while the capsid size of the λ phage virus is only around 50 nm. The chromosome of *E. coli* has a ring shape topology with 4.6 Mbp. The contour length of a *E. coli* chromosome is around 1.6 mm, while the *E. coli* cell is only about 2 μm. The human genome has a contour length about 2 m long while the size of a human zygote is usually less than 1 mm. The drastic contrast between the DNA contour length and the size of the containing cell leads to a tight confinement environment for the DNA chains.

The *persistence length* P measures the rigidity of the dsDNA chain. The persistence length is defined formally as the length scale along the chain contour at which the tangential vectors become uncorrelated. Suppose a DNA chain starts at position 0 with a unit length tangent vector $t(0)$, the autocorrelation of t satisfies $\langle t(0)t(s)\rangle = e^{-s/P}$, where $\langle \ldots \rangle$ denotes the ensemble average. Note that the persistence length is dependent upon the local chemical environment around the DNA chain (it is not a fundamental physical constant). For instance, at a typical buffer condition–1X tris buffer–at 300 K, the persis-

tence length of a dsDNA is close to 50 nm. In low salt condition–0.01X-0.1X tris buffer for example–P can reach 80 nm due to the increase of the debye length [54].

The *effective width* w measures the range of interaction perpendicular to the dsDNA backbone. The effective width can be estimated by the physical width of the dsDNA plus two Debye lengths in a given buffer. This method underestimates the dsDNA width, however. Schellman and Stigler [56] have further refined the theoretical estimation of w by using an interaction potential from solving the linearized Poisson-Boltzmann equation for a charged rod and applying the solution at the Stern layer. Experimental results from light scattering and the probability of finding knots in crystalized DNA consistently agree with this refined theoretical expression [56].

The *excluded volume* v is a geometry effect that two monomers cannot occupy the same physical space. It is defined as[1]:

$$\mathrm{v} = \int (1 - exp[-U(r)/(k_B T)]) d^3 r, \tag{2.1}$$

where r is the position vector originating from the monomer of interest, and $U(r)$ is the pair interaction function between monomers. The excluded volume is sensitive to the solvent temperature. A simplified model to estimate the excluded volume of an artificial chain interacting via the van der Walls effect is $\mathrm{v} = v_0(1 - \Theta/T)$ [1], where Θ is the temperature such that $\mathrm{v} = 0$ and the chain becomes ideal. The quantity v_0 is the athermal excluded volume. At a high temperature limit, the solvent is named as *athermal* as v does not change with temperature. The solvent is considered as *good solvent* when $\mathrm{v} > 0$ and *poor solvent* when $\mathrm{v} < 0$. The volume exclusion increases the scaling exponent v for the end-to-end chain size in athermal solvent $R \sim N^{\nu}$ from 0.5 to the Flory value of 0.6 (note the exact value is 0.588, obtained from renormalization group calculation [57]). Note that the van der Walls model applies only to artificial neutral polymers, not electrolytes like

DNA, which interact via repulsive electrostatics. For DNA, the excluded volume or a given Kuhn segment scales as wP^2 [54].

The *radius of gyration* R_g gives the spatial extent of a coiled DNA chain. The gyration radius R_g is defined as:

$$R_g = \sqrt{\frac{\sum_i m_i \langle (\mathbf{r}_\mathrm{i} - \mathbf{r}_0)^2 \rangle}{\sum_i m_i}}, \tag{2.2}$$

where $\mathbf{r_0}$ is the center of mass of the DNA and the quantities m_i and $\mathbf{r}_\mathrm{i}$ correspond respectively to the mass and position of the i^{th} polymer unit. Note the size of the DNA chain depends on the excluded volume of the DNA chain. The average conformation of a DNA chain is NOT always symmetric when under confinement.

The end-to-end distance R is another commonly used quantity to describe the chain size. The end-to-end distance is defined as $\langle R^2 \rangle = \langle |\mathbf{r}_\mathrm{N} - \mathbf{r}_0|^2 \rangle$, where $\mathbf{r}_\mathrm{N}$ is the vector of the monomer at the end of the chain. Note that the end-to-end distance and the radius of gyration scale identically with N (i.e. as $\sim N^{1/2}$ for an ideal chain and $\sim N^{3/5}$ for a Flory chain).

2.2 DNA chain: semiflexible chain or flexible with self-avoidance

For weak to moderate confinement the DNA chain can be described as a sequence of blobs of scale ξ within which monomers perform a bulk random walk. Recall that within a blob the chain has no "knowledge" of confinement; the conformation inside a blob is identical to that of the bulk chain (also be aware that a blob is always defined in an ensemble average sense and reflects average chain scaling properties). Globally the chain conformation corresponds to a stacking of blobs of scale ξ; the blobs stack linearly in a tube and perform a self-avoiding random walk in nanoslit confinement. Under very strong confinement, the rigidity of the DNA chains dominates and the conformation of DNA

is described as a sequence of deflection lengths [58, 59]. Here we discuss the transitions between those two possible pictures.

First, we briefly discuss the conformation of a bulk chain. In the absence of excluded volume (i.e. $w = 0$ thus $\mathrm{v} = 0$), the chain performs a random walk with the ideal scaling $R \sim (PL)^{1/2}$. If the excluded volume effect is very strong (i.e. w very large), then the chain performs a self-avoiding random walk giving rise to the swollen coil scale $R \sim (Pw)^{1/5}L^{3/5}$ [54]. For the excluded volume of "intermediate" strength, we introduce a special scale called the "thermal blob" ξ_T which gives the chain spatial scale beyond which the excluded volume is significant. The chain follows an ideal scaling below ξ_T and exhibits a self-avoiding random walk scaling above. To find the thermal blob scale, we find the scale at which thermal energy balances the volume exclusion energy: $k_BT\mathrm{v}(\frac{g_T^2}{\xi_T^3}) = k_BT$ (with g_T the number of chain units in a thermal blob of scale ξ_T). As we can assume an ideal scaling at the threshold, or $\xi_T \sim Pg_T^{1/2}$, we find that $g_T \sim (P/w)^2$ and $\xi_T \sim P^3/w^2$ using $v \sim wP^2$. This implies that stiffer chains exhibit more ideal chain behaviour (i.e. have a larger thermal blob scale).

In Fig. 2.2, a DNA chain is confined in a cylindrical tube. By decreasing the cross-section size of the tube, the crossover for different regimes occurs. For $D \gg \xi_T$ (Fig. 2.2a), the confined chain is in the de Gennes regime and the chain can be viewed as a sequence of spherical blobs with the size equal to the cylindrical pore cross-section. As D decreases down to scales comparable with or less than ξ_T, these blobs will be elongated along the long axis of the cylinder, but a classic scaling $R \sim 1/D^{2/3}$ persists (this regime is sometimes called the "extended" de Gennes regime). As D continues to decrease, the stiffness of the chain dominates and the chain enters Odijk regime where the chain is deflected by the confinement wall in every deflection length λ. Note this regime requires D to be smaller than the persistence length of the chain.

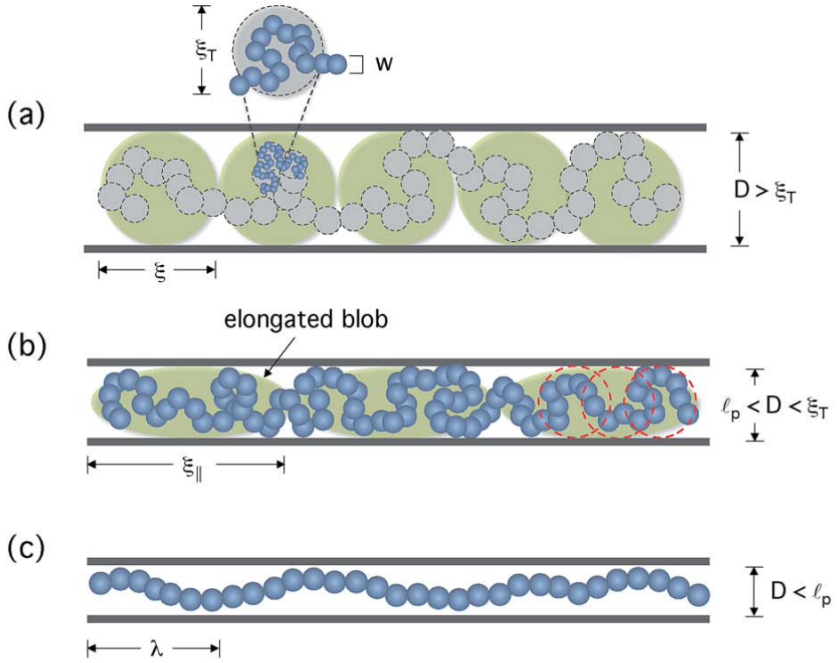

Figure 2.2: Organization of polymers with self-avoidance in a cylindrical space characterized by a few regimes. Adapted (with modifications) with permission from *Bae-Yeun Ha and Youngkyun Jung. "Polymers under confinement: single polymers, how they interact, and as model chromosomes." Soft Matter, 2015, 11, 2333.* Copyright The Royal Society of Chemistry 2015. a) de Gennes regime: for $D \gg \xi_T$ the blob-scaling picture remains relevant: $R \sim ND^{1-1/\nu}$ and $F \sim ND^{-1/\nu}$ b) Extended de Gennes regime: for $P \ll D \ll \xi_T$, $R \sim ND^{1-1/\nu}$ as in a) and $F \sim ND^{-2}$ as for an ideal chain. c) Odijk regime: when $D \ll P$, the chain is deflected by the confinement wall with a deflection length λ. Over the scale λ, the confined chain does not feel the effect of confinement and local stiffness dominates.

2.3 DNA chains under confinement

By harnessing nanofabrication technology, it is possible to investigate how DNA chains behave in confined environments [54]. Nanofeatures such as nanoslits, nanochannels and nanocavities create spatial restrictions on the DNA chain (see fig. 3.4). These restrictions lead to the conformational change of the DNA when the scale of confinement falls below or comparable to the chain gyration radius. Fluorescence microscopy enables us to observe the chain conformation and the dynamics. While DNA chains are stained with

a fluorescent dye (YOYO-1 for example) and confined in the nanofeatures, fluorescent videos can be recorded and analyzed [54].

2.3.1 DNA conformation in a nanochannel

A nanochannel is a quasi-1D tube-like geometry where DNA chains are confined in x- and y- directions and almost no confinement in z- direction. As the channel cross-section becomes smaller, DNA chains elongate to almost their full extension. While the increase of DNA extension with decreasing channel size seems intuitive, the theory has proven to be very non-trivial. For a channel width $D > P$, the chain extension is described via a blob regime. The chain extension scales as $R \sim (Pw)^{1/3}/D^{2/3}L$ in this regime, as described in the introduction. At around $D \sim P$ there is a transition to the regime where chain back-bending is completely suppressed described in terms of Odijk deflection segments of the DNA with the channel [54].

2.3.2 DNA conformation in a nanoslit

A nanoslit is a quasi-2D slab like geometry where DNA chains are confined in z- direction and almost no confinement in x- and y- direction. DNA chains confined in a nanoslit adopt a pancake shape, where the size of the chain is described by the 2D radius of gyration. For confinement of chains in slits with height h, in a regime where $h \gg P$ than the "pancake" extent scales as $R \sim (Pw)^{1/4}/h^{1/4}L^{3/4}$. Similar to the nanochannel confinement, DNA chains transit from bulk coil to blob picture to a picture based on deflection segments as the slit height decreases [60].

2.4 DNA solution

While the equilibrium properties of single chains in confinement have been extensively studied, we have a relatively poor understanding of confined multiple chain systems,

i.e., confined polymer solutions. A DNA solution refers to the homogeneous liquid phase substance when DNA chains are dissolved in a good solvent such as 1X tris buffer. Depending on the average distance r between the neighbouring DNA chains, the solution can be classified as lying in a dilute, semi-dilute or concentrated regime. In a dilute solution, DNA chains are far apart ($r \gg R_g$). The DNA single chain conformation is identical to the conformation in bulk. In semi-dilute solution, DNA chains start to touch each other ($r \sim R_g$). In a concentrated regime, the chains strongly overlap and the DNA solution approaches a melt. The transition concentration between dilute and semi-dilute solution is:

$$\phi^\star \sim \frac{Na^3}{R^3} = \frac{1}{\sqrt{N}}, \tag{2.3}$$

where a is the length of a monomer and R is the spatial extent of a chain. Polymer solutions with concentrations higher than $\phi^\star$ are considered semi-dilute. Therefore when DNA chains are confined in a cavity with size comparable to the R_g, the confined chains can be described as a semi-dilute DNA solution [1]. Note the chain concentration is still very low ($\phi^\star < \phi \ll 1$). Therefore, we can imagine a monomer in a semi-dilute DNA solution is surrounded mostly by solvent. The correlation length ξ measures the average distance between two different chains in a semi-dilute solution. The correlation length also corresponds to a blob scale ξ: monomers within ξ interact mostly with solvent and the same chain. The correlation length decreases with increasing concentration as a power law: $\xi \sim b(\frac{b^3}{\mathrm{v}})^{(2\nu-1)/(3\nu-1)}\phi^{-v/(3\nu-1)}$ [1]. We can view a semi-dilute solution consisting of a 3D packing of blobs of extent ξ. In each blob, DNA monomers perform a self-avoiding walk since they can NOT reach other chains. On the chain scale, blobs are performing random walk [19]. The number of blobs can be calculated as $\frac{N}{N_{sub}}$ where N is the number of monomers for a chain and $N_{sub} = (D/a)^{1/(3\nu-1)}N^{(2\nu-1)/(3\nu-1)}$ is the number of monomers in each blob where $\nu = 3/(d+2)$ is the Flory exponent and d is the number of dimensions, D is the diameter of the confinement region and a is the density of monomers in the confinement region [19].

We expand the semi-dilute solution discussion by providing details of the DNA size scaling. The semi-dilute solution can be further divided into three different scaling regimes based on ξ. On scales up to the size ξ_T, the chain size scales as $N^{1/2}$. On length scale between ξ_T and ξ, the excluded volume interaction dominates the thermal energy while no chain-chain interaction presents. The chain size scales as self-avoiding chain N^{ν}. On length scales larger than ξ, the chain size scales as $N^{1/2}$ because of the exclusion screening by the overlapping chains [19].

2.5 Mean-field approximation for the concentration of a semi-dilute DNA solution

Semi-dilute flexible polymer solution in confinement was first described by de Gennes at the scaling level [16]. However, DNA chains are semiflexible. A semiflexible chain is fairly stiff within a short contour length (persistence length), i.e. polymer segements are pointing approximately the same direction, and flexible beyond the persistence length. The DNA chain orientation is correlated for a length scale below the persistence length P (around 50 nm in 1X tris buffer condition). Semiflexible chains can have special scaling regimes in confinement and in bulk where mean-field descriptions apply and the classical de Gennes blob theory for flexible chains is incorrect (in flexible chain theory, concentration fluctuations have a non-negligible effect on scaling exponents). The question of which theory applies to DNA chains in confinement is highly nontrivial. Complex scaling phase spaces that determine the appropriate description exist as a function of chain size and confinement geometry. Two studies [61, 62] previously conducted in our group involving compressing single DNA or multiple chains against a nanochannel barrier suggest the mean-field behaviour holds in channels with widths from ~ 300 nm to $\sim 1\,\mu$m. In this dissertation, we show that the mean-field method holds well for cavities with lower aspect ratios and smoother confinement walls (larger radius of curvature). However, we

observe the mean-field description gradually breaks down locally as the aspect ratio of the cavity increases. Here we review the methodology of the mean-field method and its self-consistent solution.

We assume DNA monomers are subjected to an external field $U(\mathbf{r})$. For DNA solution, this external potential is created by the density of other chains near the monomer of interest. The external field is represented as $U(\mathbf{r}) = T\mathrm{v}c(\mathbf{r})$, where T is the temperature, v is the excluded volume of the monomer and $c(\mathbf{r})$ is the DNA concentration at position $\mathbf{r}$. The "external" potential is proportional to the monomer concentration in a mean-field manner. The local exclusion between neighbouring segments is ignored. However, given the volume fraction ϕ of DNA chains is small ($\phi \ll 1$), this assumption is appropriate.

It is feasible to evaluate $U(\mathbf{r})$ and thus the monomer concentration iteratively by assuming $U(\mathbf{r})$ is external. The premise of the self-consistent calculation is as follows. We assume a concentration profile $c(\mathbf{r})$ initially. Then we solve the DNA chains $c'(\mathbf{r})$, where c' represents the concentration profile in the next iteration, as if the chain is confined in the potential field $U(\mathbf{r}) = T\mathrm{v}c(\mathbf{r})$. Then we go through the same process again and get $c''(\mathbf{r})$. This calculation continues until $U_n = T\mathrm{v}c_n(\mathbf{r})$ converges. Then the solution is considered self-consistent.

We show the derivation of the equation for semi-dilute DNA solution concentration in an external potential field. We assume the confined DNA chain has N monomers. The concentration profile of the DNA solution is $c(r)$ on a lattice grid with constant a. Thus, the element of the partition function is:

$$exp(-\frac{1}{T}[U(\mathbf{r_1}) + U(\mathbf{r_2}) + ... + U(\mathbf{r_N})]) \tag{2.4}$$

The partition function of a chain starting at $\mathbf{r}$ and end at $\mathbf{r}'$ is:

$$z^N G_N(\mathbf{r}', \mathbf{r}) = \sum^{M} exp(-\frac{1}{T}[U(\mathbf{r_1}) + U(\mathbf{r_2}) + ... + U(\mathbf{r_N})]), \tag{2.5}$$

where z is the number of neighbours pulled out from the summation and M is the number of possible chain configurations from $\mathbf{r}$ to $\mathbf{r}'$.

By adding 1 extra monomer, we find:

$$G_{N+1}(\mathbf{r}', \mathbf{r}) = \frac{1}{z} \sum_{\mathbf{r}''}^{'} G_N(\mathbf{r}', \mathbf{r}'') exp(-\frac{1}{T}[U(\mathbf{r})]), \tag{2.6}$$

where the prime means that the summation is restricted to the nearest neighbours of $\mathbf{r}$.

Assuming the DNA chain is very long compared with the lattice size and $U(\mathbf{r})/T$ is sufficiently small, we can safely expand the $G_{N+1}(\mathbf{r}', \mathbf{r})$ as:

$$G_{N+1}(\mathbf{r}', \mathbf{r}) = \frac{1}{z}(1-\frac{U(\mathbf{r})}{T}) \sum_{\mathbf{r}''}^{'} G_N(\mathbf{r}', \mathbf{r}) + (\mathbf{r}-\mathbf{r}'') \frac{\partial G_N(\mathbf{r}', \mathbf{r})}{\partial \mathbf{r}} + \frac{1}{2}(\mathbf{r}_\alpha - \mathbf{r}'')(\mathbf{r}_\beta - \mathbf{r}'') \frac{\partial^2 G_N(\mathbf{r}', \mathbf{r})}{\partial \mathbf{r}_\alpha \partial \mathbf{r}_\beta} + ..., \tag{2.7}$$

The prime means the summation is restricted to the neighbour sites of $\mathbf{r}$. Note the $\mathbf{r} - \mathbf{r}''$ term vanishes because of the symmetry of the lattice. We get:

$$G_{N+1}(\mathbf{r}', \mathbf{r}) - G_N(\mathbf{r}', \mathbf{r}) \cong \frac{\partial G_N}{\partial N} = -\frac{U(\mathbf{r})}{T} G_N(\mathbf{r}', \mathbf{r}) + \frac{a^2}{6} \Delta G_N(\mathbf{r}', \mathbf{r}) \tag{2.8}$$

where $\frac{1}{6}$ comes from the geometrical sum property for a cubic lattice in 3D. Therefore, we get:

$$-\frac{\partial G_N}{\partial N} = -\frac{a^2}{6} \Delta G_N + \frac{U(\mathbf{r})}{T} G_N, \tag{2.9}$$

where a is the length of a unit lattice. This equation is identical to the diffusion equation describing a random walker in an external field with time replaced by the number of monomers N. Each configuration of the chain represents a trajectory of a random walker.

The eigenvalue problem of the above partial differential equation is:

$$(-\frac{a^2}{6} \Delta + \frac{U(\mathbf{r})}{T}) u(\mathbf{r}) = \epsilon u(\mathbf{r}), \tag{2.10}$$

where ϵ and $u(r)$ are the eigenvalue and the eigenvector of the eq. 2.10. Note ϵ_k is a sequence of possible eigenvalues starting from a minimal value ϵ_0 which we call the ground state. The orthogonality and the completeness of the eigenvector $u_k(r)$ can be proven trivially. Therefore, $G_N(\mathbf{r}', \mathbf{r})$ can be expanded as:

$$G_N(\mathbf{r}', \mathbf{r}) = a^3 \sum_k u_k^*(\mathbf{r}') u_k(\mathbf{r}) exp(-N\epsilon_k) \tag{2.11}$$

The expansion has an exponential term that gives higher weight to lower eigenvalues. For chains with a sufficiently large N , it is sufficient to only keep the ground state term ϵ_0 (ground state dominance). Study [62] has shown that T_4-DNA–sample used in this dissertation–can be described well by the mean-field theory with the ground-state dominance assumption.

The concentration $c(\mathbf{s})$ of the DNA solution can be calculated by weighting $G_N(\mathbf{r}', \mathbf{r})$ at the position of interest s:

$$\Phi(\mathbf{s}) = a^3 c(\mathbf{s}) = \frac{\sum_{\mathbf{r}'} \sum_{\mathbf{r}} \sum_{\mathbf{N}'=\mathbf{0}}^{N} G_{N'}(\mathbf{r}', \mathbf{s}) G_{N-N'}(\mathbf{s}, \mathbf{r})}{\sum_{\mathbf{r}'} \sum_{\mathbf{r}} G_N(\mathbf{r}', \mathbf{r})} \tag{2.12}$$

Note $\Phi(\mathbf{s})$ is the fraction concentration normalized to unity. If there are multiple uncorrelated chains, we can multiply $\Phi(\mathbf{s})$ by the total number of chains.

For ground-state dominance situation, the eq. 2.12 can be further simplified as:

$$c(\mathbf{s}) = N|u_0(\mathbf{s})|^2 \tag{2.13}$$

The self-consistent potential can be introduced to eq. 2.10 by replacing $U(\mathbf{r})$ with $T\mathrm{v}|u_0(\mathbf{r})|^2$. The mean-field partial differential equation becomes:

$$-\frac{a^2}{6}\Delta u(\mathbf{r}) + \mathrm{v}u(\mathbf{r})^3 = \epsilon u(\mathbf{r}), \tag{2.14}$$

This equation also has the form of a nonlinear Schrödinger equation, reminiscent of equations used to model a confined Bose gas.

The pseudocode for solving Eq. 2.14 is:

Algorithm 1 Self-consistent DNA solution concentration calculation

$eps = 1$
$u_0^0 = 0$
$n = 1$
while $eps > 1e^{-16}$ **do**
  solve $(-\frac{a^2}{6}\Delta + v(u_0^{n-1})^2)u_0^n = \epsilon u_0^n$
  where ϵ is minimized
  $eps = \int (u_0^n - u_0^{n-1})^2 d\mathbf{r}$
  $n = n + 1$
end while

2.6 Finite element analysis for the semi-dilute DNA solution

We solve the Eq. 2.14 in 2D numerically by finite element method. The cavity is divided into small triangles with a value assigned to each vertex (see Fig. 2.3a). We translate the equation with Galerkin method [63] to create the weak formulation (weakform). The weakform is a finite-element technique that transforms a partial differential equation into an integral equation by multipling test functions, usually the basis of the mesh, to both sides of the equation and integrate over the mesh. We assume the ground-state dominance since the DNA chains have a sufficient number of monomers. We iteratively solve the self-consistent potential (see Algorithm. 1). Here we walk through the methodology of the finite element method.

We solve eq. 2.14 by minimizing the residue of the weakform. If the eq. 2.14 holds, for any given trial function $h(\mathbf{r}) = \sum_i a_i h_i$ where h_i is a base function from the discretized

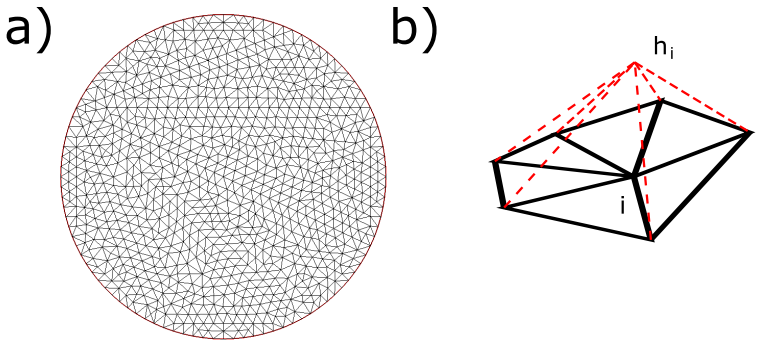

Figure 2.3: Mesh and base functions for finite element analysis. Here the cavity in our experiment is discretized into a triangle mesh and the solution is defined by the value on the nodes. a) mesh of a circular finite element space. b) hat function h_i at node i

mesh and a_i is a scalar coefficient, the following integral should be satisfied:

$$\int (-\frac{a^2}{6}\Delta u^n + v(u^{n-1})^2 u^n) h_i d\mathbf{r} = \epsilon \int u^n h_i d\mathbf{r} \tag{2.15}$$

We use piecewise linear continuous finite element (hat function in Fig. 2.3b) as the base function. It has a value of unity at node i and zeros elsewhere.

The solution $u^n(\mathbf{r})$ can be expanded by the base function as:

$$u^n(\mathbf{r}) = \sum_i c_i h_i(\mathbf{r}) \tag{2.16}$$

where c_i is a scalar coefficient. We substitute eq. 2.16 into eq. 2.15 and take the integral by part:

$$\sum_j c_j \int \frac{a^2}{6} \nabla h_j \nabla h_i + v(u^{n-1})^2 h_j h_i d\mathbf{r} = \epsilon \sum_j c_j \int h_j h_i d\mathbf{r} \tag{2.17}$$

This equation can be simplified as:

$$\mathbf{A}\mathbf{c} = \epsilon \mathbf{B}\mathbf{c} \tag{2.18}$$

where $\mathbf{A}_{\mathrm{i,j}} = \int \frac{a^2}{6} \nabla h_j \nabla h_i + v(u^{n-1})^2 h_j h_i d\mathbf{r}$, $\mathbf{B}_{\mathrm{i,j}} = \int h_j h_i d\mathbf{r}$.

After assembling the matrix $\mathbf{A}$ and matrix $\mathbf{B}$, the eigenvalue problem of the form $\mathbf{A} - \epsilon\mathbf{B}$ can then be fed into ARPACK++ to be solved. The discretization, matrix assembling

and the interface to ARPACK++ have been implemented in the open-source PDE solver FreeFEM++ [64].

2.7 Problem of chromosome segregation and partition

Jun *et al.* [65] developed a two-chain system phase diagram and demonstrated that chromosomes can spontaneously demix under cellular confinement. Remarkably, the phase diagram predicts that the chain mixing/demixing strongly depends on the geometry, especially the anisotropy, of the confinement. A tube-like confinement structure promotes the spontaneous demixing of the confined DNA chain (as observed in the introduction), while mixing arises in isotropic confinement (spherical confinement). This phenomenon is predicted by classic scaling theories and verified numerically by molecular dynamics simulation. Here, we review the theoretical phase diagram of the polymer mix/demixing. The phase diagram indicates how multiple polymers are spatially organized and fluctuate in confinement with varying anisotropy and how the organization of multiple chains scales with chain size and confinement.

2.8 Phase diagram of the polymer mixing and demixing

The phase diagram of a single chain confined in a cylindrical pore was proposed by Lal *et al.* [66]. Jun *et al.* extended the single-chain system picture to two-chain system. They propose a two-chain mixing/demixing phase diagram by incorporating the piston picture and scaling arguments [12]. In their formulation, two independent polymer chains are confined in a syringe-like structure with a piston on the side. The syringe has a fixed volume to keep the chain concentration the same. The correlation length ξ_{bulk} gives the size of a blob when the chain is in bulk with a given concentration.

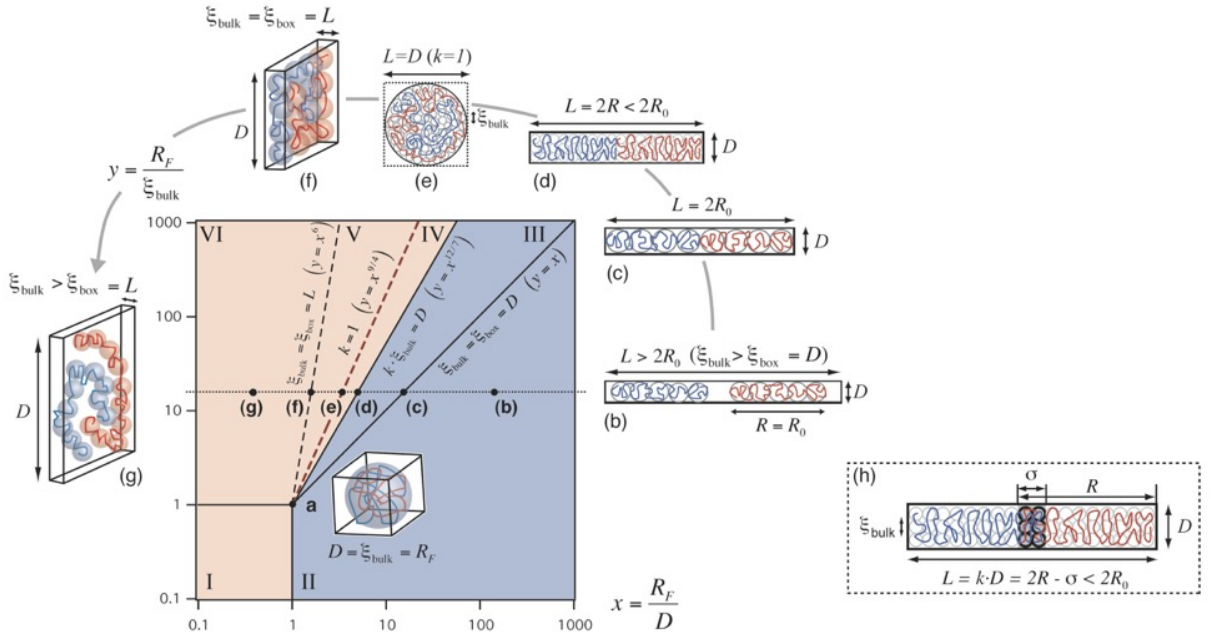

Figure 2.4: Phase diagram of a two-chain polymer solution system. The cross-section of the syringe is DxD and the length of the syringe is L. The x-axis represents the aspect ratio of the geometry with 1 being a cube confinement. The $y-$axis represents the concentration of the polymer solution. The phase diagram is divided into mixing regime (red) and demixing regime (blue). The dotted horizontal line indicates how aspect ratio of confinement affects the phase of the two-chain system. From (b)-(g), the two-chain system experiences a transition from a completely segregated regime (b) to a transition regime where chains start touching at the interface (d) to a mixing regime (g). (h) same as (d), but the two chains overlap at the interface. The correlation length ξ_{bulk} is smaller than the width of the box. R_0 is the end-to-end distance of a chain in a long box with the same width. Reproduced with permission from S Jun et al. *Nat. rev. microbiol, 8, 600-607. (2010)*

The phase diagram is shown in Fig. 2.4. The dimensionless quantity $x = R_F/D$ is the ratio between the size of the bulk chain and the cross-section of the syringe box; thus, the anisotropy of the confinement. Another dimensionless quantity $y = R_F/\xi_{bulk}$ is the ratio between the size of the bulk chain and the bulk correlation length ξ_{bulk}. As the chain concentration increases, ξ_{bulk} decreases monotonically; and thus y increases.

The phase diagram is divided into two regimes. The chain segregation regime and the chain mixing regime. The two regimes are further divided into six sub-regimes with the boundary drawn from the scaling argument.

Regime I: In this regime, the chain concentration is low and considered as "dilute". On average the chain to chain distance is much smaller than the confinement scale. In particular, when $D = L = R_F$, the correlation length ξ_{bulk} also equals to D. Thus, the chains have the same conformation as they are in bulk. Two chains can adopt either demixing or mixing configuration with a free energy cost on the order of k_BT [19].

Regime II: In this regime, the dilute chain solution is confined in an elongated confinement geometry. Due to the high aspect ratio, the chains are separated apart inside the confinement with a gap in between. The length of the chain R_0 is less than half of L. The scaling of the chain size is $R_0 \sim (N/g_b)D \sim ND^{-2/3}$, where g_b is the number of monomers in a blob following $D \sim ag_b^{\nu}$ [1, 16]. The two chains strongly exclude each other and adopt the full segregation configuration.

Regime III: In this regime, the aspect ratio of the confinement decreases so that two chains overlap at the interface. The bulk correlation length ξ_{bulk} is smaller than both D and L. The chains start losing their linear ordering gradually. The interface region between the two chains starts mixing until the linear conformation is completely lost.

Regime IV, V and VI: As the aspect ratio approaches 1, the two chains lose their linear conformations and mix. The boundary between V and VI is defined by $\xi_{bulk} = L$, which is translated as the blobs starting to feel the presence of the slab wall.

We clarify the boundaries between the above regimes.

From regime I to II: For this transition, the chains are in dilute regime. Two chains are far apart (Fig. 2.4 (b) point) and not expected to interact within the bulk coil size R_F. As the confinement aspect ratio increases, the two chains spontaneously "demix" and start adopting linear ordering. The point a is a special transition point. The size of the

confinement equals to the size of the chain; thus the chains adopt the same conformation as in bulk. The transition boundary thus is $x = 1$.

From regime II to III: For this transition, as the aspect ratio of the confinement decreases, the gap between two chains reduces until the two chains just touch (Fig. 2.4 (c) point). In this case, the correlation length $\xi_{bulk} = \xi_{box}$ since two chains fully occupy the confinement. The blob scale equals the width D of the confinement; therefore we have $\xi_{bulk} = \xi_{box} = D$, which is translated as $y = x$ in the reduced coordinates.

From regime III to IV: This transition point is defined by the loss of the chain ordering as the aspect ratio decreases. In regime III, the bulk correlation ξ_{bulk} is less than both D and L. The two chains perform random walks in the unit of the blob. In regime IV, the two chains are considered as a semi-dilute solution since their average inter-chain distance is much larger than the blob size. When we calculate the chain size along L direction, for a semi-dilute solution, we have $R_{/\!/} \sim N^{1/2}\phi^{-1/8}$[1] where $\phi \sim N/R_{/\!/}D^2$ is the monomer concentration. When two chains start adopting linear ordering, the chain size along L direction can be evaluated from the blob picture, which gives $R_{/\!/} \sim (N/g_b)\xi_{box}^3/D^2$. The transition point can be easily solved by comparing the semi-dilute solution size and linear ordering chain size. This gives the boundary $y = x^{12/7}$.

From regime IV to V: This transition is very similar to III to IV. In regime V, the aspect ratio of the confinement becomes less than 1, leading to the chains mixing and compressed in a slab-shape geometry. The correlation length ξ_{bulk} is less than the length L of the box. The transition happens when the aspect ratio becomes unity. In this case, the box is filled with blobs and the volume of the box $D^2L = D^3 \sim (N/g_b)\xi_{bulk}^3$, which gives the boundary condition $D^{9/4} \sim \xi_{bulk}$. This condition translates to $y = x^{9/4}$.

From regime V to VI: In this case, the bulk correlation $\xi_{bulk} \sim L$. The chain size projected to the cross-section of the syringe can be calculated as the chain performing 2D random walk with unit of blobs. Thus, the size of the cross-section $D \sim \xi_{bulk}(\frac{N}{g_b})^{1/2} \sim$

$L(\frac{N}{L^{1/\nu}})^{1/2}$. This gives the relation $D \sim L^{1/6}$ which is translated as $y = x^6$ in the phase diagram. Note this transition is the analogue of the transition between regime II and III.

There are Monte Carlo simulations supporting the phase diagram derived purely from scaling. Y Jung. *et al* [67] have shown numerically that the spatial organization of a two-chain system is closely related to the linear ordering of the chain. Their simulations suggest the linear ordering ensures the high degree of chain segregation. The anisotropy of the confinement geometry contributes to the chain segregation up to 70% to 80%, even outside de Gennes regime. Their simulation also gives the boundary between regime III, IV and V, which are consistent with the scaling phase diagram.

This phase diagram presented in Fig. 2.4 predicts the regime in which the chromosomes of a bacteria with certain geometry can segregate passively by using conformational entropy. For example, S. Jun *et al.* [12] has marked the location of the model system E. coli B/r (H266) strain in the phase diagram. The chromosome of H266 strain is located in the demixing region while the plasmid is located in the mixing region. This indicates the chromosomes of H266 can segregate passively while the plasmid tends to mix, i.e. diffuses freely in the cell. The chromosome location in the phase diagram is decided by the cell geometry and dsDNA concentration. Cells of H266 strain has a rod-shape body with hemispherical caps when in steady state (replication time around 150 min). The average length of the cell is 2.5μm and the width is 0.5μm. The nucleoid region, however, is smaller than the cell size. The nucleoid region is estimated to have a width of 0.24 μm and a length of 1.39 μm. The coil size R_F is measured to be 3.3 μm[68]. The correlation length in bulk ξ_{bulk} is a much more difficult quantity to measure. However, it is generally safe to assume the lower bound of ξ_{bulk} is the persistence length of dsDNA. Studies have shown that there are ~ 400 topological domains in E. coli chromosome[69], corresponding ~ 53 nm per unit. The correlation length ξ_{bulk} is also measured by fluorescence correlation spectroscopy[68]. Their result shows there are approximately 50 kb for each structural unit, which translates to 87 nm per unit. They also calculate the correlation

length by the diffusion coefficient of isolated nucleoids. They estimate the structural unit size is $70 \pm 20\,nm$, which agrees well with all the values mentioned above. We obtain $x = 13.6$ and $y = 37.5$, which indeed locates in the segregation regime.

Our nanofluidic system is a box with 200 nm height which is significantly smaller than the width $\sim 1\,\mu$m. Such flat geometry is in mixing regime V in the phase diagram. While this result means the two chains mix in the longitudinal direction, chains do not necessarily mix in the transverse direction. Jun *et al.* has suggested that slit-like systems should show enhanced segregation in the transverse direction, which is similar to tube confinement. Our experiments show that the λ-DNA molecules do not mix instantaneously, which is consistent with what Jun *et al.* predicted. Note there are real biological systems that resemble this flat box geometry. For example, *H. walsbyi* [23], an archea that is found in brine pools, has a stamp-like square shape with a thickness of less than $0.2\,\mu$m and a width around 2-5 μm. During cell replication, *H. walsbyi* grows into a rectangular shape, which increases the aspect ratio of the cell. This may help to ensure chromosome partitioning prior to division.

2.9 Plasmid Brownian Dynamics

Plasmids are isolated small circular dsDNAs in bacteria cells. They contain genes that are critical for cell metabolism, pathogenesis and evolution. While plasmids replicate and partition autonomously, plasmids are still able to maintain a stable inheritance in the offspring cells.

Each plasmid will have a certain number of identical copies in the bacterium (the copy number). Depending on their copy number, plasmids have different transport and partition mechanism. Low-copy number plasmids(lcn-plasmid), with usually less than ten copies in each cell, have evolved sophisticated partition mechanisms (*Par*) to ensure the successful passage to each daughter cell. The motion of lcn-plasmids usually is controlled

by the spindle-like structures that consume ATP [31]. High-copy number plasmids (hcn-plasmid), with usually tens or even hundreds of copies in each cell, are not known to have a specific active partition mechanism. It is generally believed the motion of the high-copy number plasmid is purely random and driven by thermal energy. Recent in vivo studies [43, 13, 32] provide experimental evidence suggesting that hcn plasmids undergo Brownian motion. Here, we focus on the hcn-plasmids and briefly review the formulation of Brownian motion.

Due to the immense complexity from the microscopic details of the liquid, the exact description of a Brownian motion particle is seldomly solved. As an alternative, the *Langevin equation* offers a semi-empirical description that only needs a few parameters, i.e. the external field, the friction and the thermal fluctuations.

$$m\frac{dv}{dt} = F_e + F_f + F_r(t), \tag{2.19}$$

where F_e is the external force, $F_f = -\gamma v$ is the friction with γ being the friction coefficient and F_r is the stochastic force that arises from many collisions experienced by the solute particle. The autocorrelation of the thermal fluctuation force can be written as:

$$\sigma_0^2\delta(t-t') = \langle F_r(t)F_r(t')\rangle \tag{2.20}$$

By taking integral on both sides of the equ. 2.19 and neglecting the external field for the moment, we have:

$$v(t) = v(0)e^{-\frac{t}{\tau}} + \frac{1}{m}\int F_r(t')e^{-\frac{t'-t}{\tau}}dt' \tag{2.21}$$

where $\tau = \frac{m}{\gamma}$. The first term decays to zero when the time is much longer than τ. Assuming the time considered here is long enough, we take the autocorrelation of $v(t)$ and get $< v(t)v(t') >= \frac{\langle F_r(t)F_r(t')\rangle}{m^2}e^{-\frac{t-t'}{\tau}}$. By setting $t = t'$ and substituting the equipartition

theorem, we get the famous Einstein relation:

$$\sigma_0^2 \equiv 2\gamma k_B T \tag{2.22}$$

When taking the integral of eq. 2.19, we assume that dt approaches zero. However, this conflicts with the stochastic force $F_r(t)$, which we expect $\langle F_r(t)F_r(t')\rangle \sim \delta(t-t')$. To fix this conflict in integration, we can either set $\langle F_r(t)F_r(t')\rangle \sim e^{-\frac{|t-t'|}{\tau}}$ and choose dt close to zero (Stratonovitch method) or let dt approach 0 slower than $\langle F_r(t)F_r(t')\rangle$ (Itô's method).

Due to the strong hydrodynamic friction of the solution, we can safely ignore the inertial term and Eq. 2.19 reduces to the over-damped Langevin equation:

$$\gamma \frac{dx}{dt} = F_r(t) \tag{2.23}$$

By using either Stratonovitch method or Itô's method, we can calculate the mean-squared displacement from correlating equ. 2.23, and we get the famous diffusive relationship:

$$\langle x^2(t)\rangle = \sigma_0^2 * t \tag{2.24}$$

The Brownian motion of a particle can also be described by Fokker-Planck equation. Fokker-Planck equation calculates the evolution of the probability distribution of finding the Brownian particle in a free energy landscape $F(x)$. In the Brownian particle setup, Fokker-Planck equation is also called Smoluchowski equation:

$$\frac{\partial P(x,t)}{\partial t} = \frac{\partial}{\partial x}\frac{1}{\gamma}\left(k_B T \frac{\partial P(x,t)}{\partial x} + P(x,t)\frac{\partial F}{\partial x}\right), \tag{2.25}$$

where $P(x,t)$ is probablity of finding the Brownian particle at position x.

The stochastic nature of the Langevin equation is preserved by the Smoluchowski equation due to its probability description. This partial differential equation with various boundary conditions can be solved to obtain the evolution of the Brownian particle dis-

tribution. The Smoluchowski equation shows that at long times the probability density describing particle position reduces to the equilibrium distribution (set $\frac{\partial P}{\partial t} = 0$):

$$P(x) \sim e^{-\frac{F(x)}{k_B T}}, \tag{2.26}$$

which allows us to probe the free energy landscape from the equilibrium distribution.

2.10 Entropic depletion

The entropic depletion force usually is observed in a binary system mixing large macromolecules and/or large colloids and small inert particles [70]. The small inert particles create an attractive interaction between the larger particles and/or macromolecules (see Fig. 2.5(a)); this arises because excluded-volume released to the small particles when the large particles come together, increasing the overall system entropy. The conformation of large macromolecules in the presence of small inert particles is also altered, due to intramolecular interactions induced by the attractive depletion interaction (in this case the small inert molecules are termed molecular crowders). Typically, in bulk, these lead to molecular condensation; however, in confined systems the physics can be more subtle. For example, study [71] shows that nanochannel confined T_4-DNA, in the presence of a low concentration of crowders (in this case 2-5 nm dextran), has an increase in extension, but is compacted at high dextran concentrations.

Entropic depletion can also lead to particle interactions with system boundaries. Depending on the detailed geometry of the boundary, the entropic depletion can either be attractive or repulsive. The attraction of the large particles to a wall and repulsion from step edges have been demonstrated in a binary bead solution [72, 73, 74, 75]. In particular, entropic depletion force can attract large neutral particles to the vicinity of the boundary and the depletion force drives large particles to places with higher boundary curvature [76]. The overlap between the excluded volume of the large neutral particles and the

boundary wall increases the accessible volume for the small spheres, hence increasing the system entropy [76] (see Fig. 2.5(b-d)).

From a physics perspective, the entropic depletion force plays an important role in determining the bacterial chromosome conformation and may also play a role in plasmid partitioning. Bacterial cells are packed with smaller molecule crowders, e.g. proteins, small RNA, and lipid vesicles. While these do not necessarily interact directly with the nucleoid and plasmids, entropically they can promote the compaction of the nucleoid, which enhances the nucleoid segregation. In addition, crowders may also create an effective entropic force field that attracts plasmids to the cellular boundary.

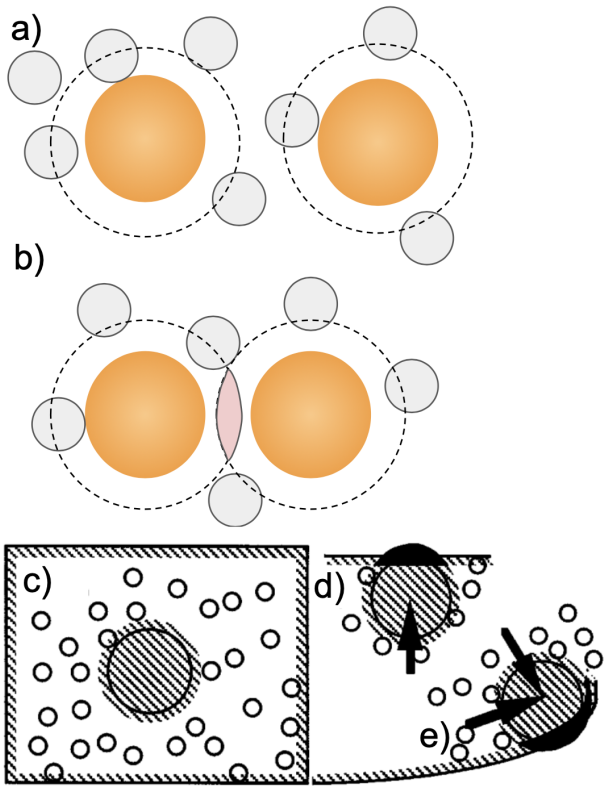

Figure 2.5: Illustration of entropic depletion forces in a binary hard-sphere mixture. a) Illustration of large spheres in a solution of smaller spheres. The dashed line indicates the excluded volume regions where the center of mass of small particles can not pass. b) As two large spheres move closer, the total volume accessible to small particles increases by the volume of the red shaded region. The overall system entropy increases. c-e) The centers of mass of the small spheres are excluded from the hatched regions. The hatched region is less than the radius of the large sphere. c) The total volume accessible to the small spheres is the box volume minus the hatched regions. d) When the large beads approach and squeeze against the wall, the total volume accessible to the small spheres increases due to the overlapping excluded volume from the wall and the large spheres. e) The curvature of the wall changes the overlap size; therefore, the large molecules will move to locations with higher curvature to maximize the overlapping region. Reprinted figure with permission from *A. D. Dinsmore, D. T. Wong, Philip Nelson, and A. G. Yodh, Physical Review Letters, Volume 80, Number 2, 1998.* Copyright (1998) by the American Physical Society.

Chapter 3

Nanofluidic Device with Variable Confinement Achieved Via Pneumatic Actuation

3.1 Introduction

Macromolecular confinement has been a topic of great interest over the past two decades [54]. When a chain is confined at scales below its gyration radius, the equilibrium conformation is altered. For example, 1D nanochannel linearizes the polymer chain and nanopores unthread the polymer coil. These properties can be used to help gain information about chain structure and chemistry. Another type of confinement is 0D or cavity confinement, which we can think of as confining the chain in a tiny box. Compared with nanochannel, nanoslit and nanopore confinement [77, 78, 79], nanocavity confinement has the potential of isolating a molecule from the environment. This molecular isolation is an essential step towards realizing our single molecule level interaction study as it ensures the interacting molecules are forced into spatial proximity and cannot diffuse away.

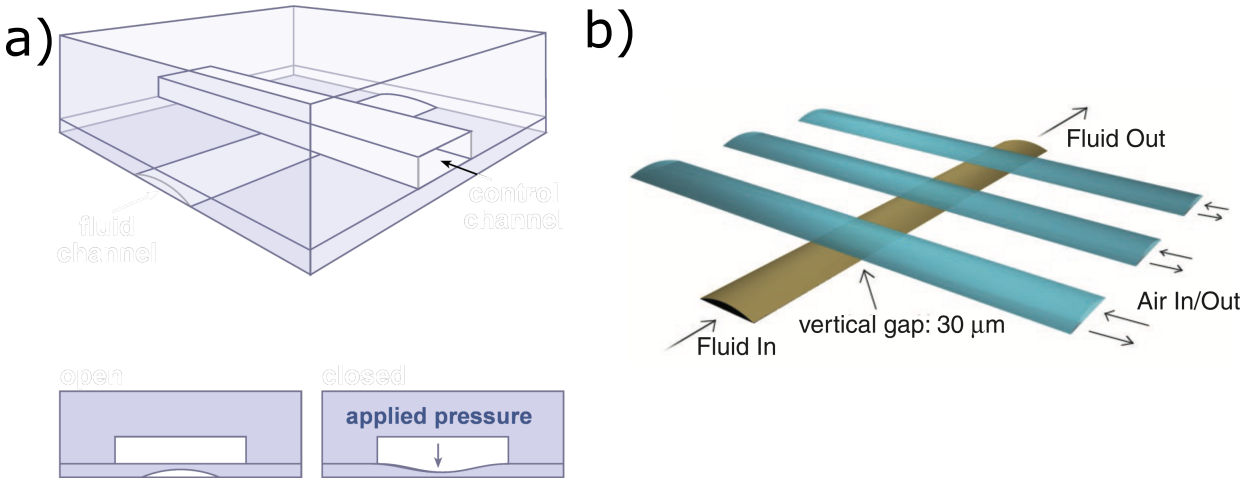

Figure 3.1: Schematic of the Quake valve. a) Structure of a single Quake valve. The PDMS membrane is actuated pneumatically. b) Multiple control channels are created on the same fluid channel. Molecules can be trapped between two closed valves.

The two-level soft-lithography valve developed by the Quake group is the first pneumatically actuated microfluidic designed to control the flow of fluid [51]. The valve is built in Polydimethylsiloxane (PDMS) via a multilayer soft-lithography process. The fluid channel and the control channel are separated by a thin PDMS membrane (see Fig. 3.1a). To seal the fluid channel, pneumatic pressure is applied to the control channel to flex the PDMS membrane downward and halt the fluid flow. By building multiple Quake valves on the same fluid channel, molecules of interest can be trapped between two valves and isolated from the main fluid (see Fig. 3.1b). Due to the elastomeric nature of PDMS, channels with a high aspect ratio tend to collapse, hindering the creation of a trapping pocket with $\sim 100\,nm$ vertical depth [80].

The dimple machine exploits the flexible PDMS lid. A lithography/reactive ion etching (RIE) process was used to produce an array of cavities etched in glass. This substrate was then bonded to a flexible PDMS lid. The PDMS lid is pneumatically deflected downward by applying a vacuum, and the molecules of interest are sealed in the nanocavities (see Fig. 3.2). However, MJ Shon et al. [53] noted that due to the ultra-small volume of

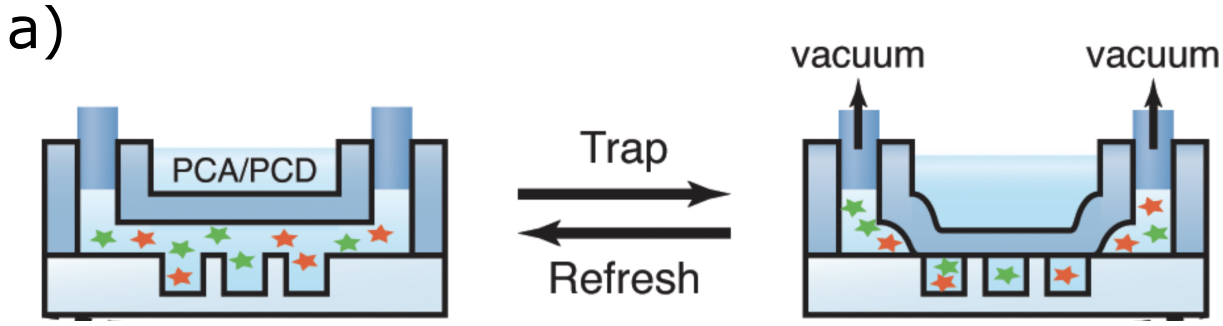

Figure 3.2: Schematic of the dimple machine. a) The trapping and refreshing state of the dimple machine. Reprinted with permission from Shon, Min Ju, and Adam E. Cohen. "Mass action at the single-molecule level." Journal of the American Chemical Society 134.35 (2012): 14618-14623.. Copyright 2012 American Chemical Society.

reactant in each dimple ($\sim 1\,fL - 1\,aL$), the reactant solution captured in the nanocavities tends to evaporate.

Convex Lens-Induced Confinement (CLIC) uses a modified planoconvex lens as a piston to push against a coverslip [52, 81]. The bottom substrate has nanoscale features created with the lithography technique. Molecules of interest are restricted to a wedge-shaped gap of nanoscale depth when the planoconvex lens touches the coverslip (see Fig. 3.3). While the evaporation and channel collapse issue is addressed by replacing PDMS with glass, CLIC technology relies on a piezo-actuated setup that complicates the experiment [81]. As a demonstration, they measured the conformation and diffusion constant of the slit-confined DNA [52].

3.2 Device concept

We developed a nanofluidic device where trapping is achieved by deflecting a thin layer of silicon nitride. A nitride layer with a thickness ranging from 50 nm to 200 nm is successfully incorporated into the device, providing opportunities for further device integration such as embedded nanopores. The schematic of the device is shown in Fig. 3.4.

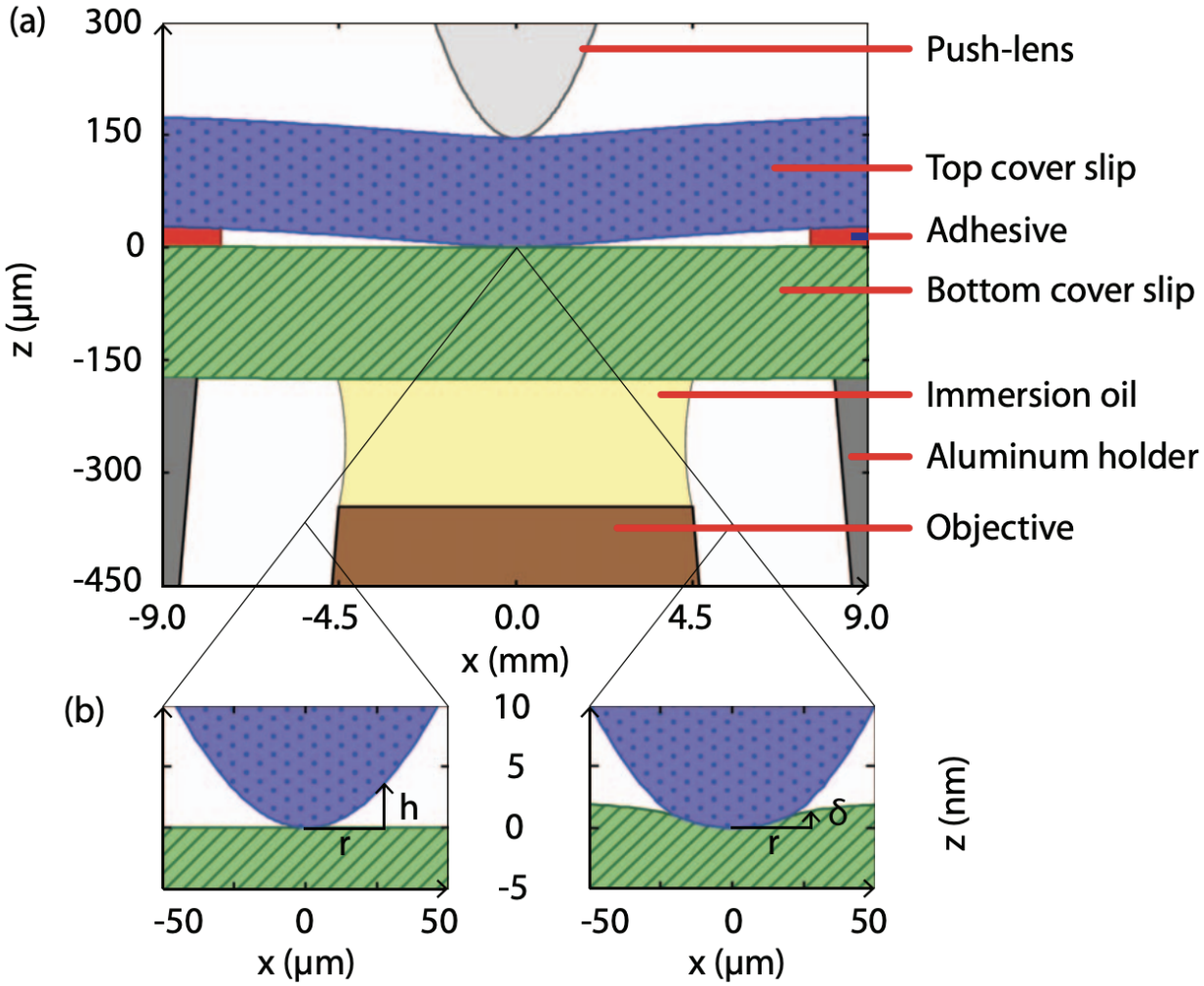

Figure 3.3: Schematic of the CLIC setup. a) The trapping and refreshing state of the dimple machine. r is the radial distance from the top cover slip center to the point of interest. b) Zoom in schematic of the contact region. h is the distance between the bottom cover slip to the top cover slip at the point of interest before pushing down. δ is the deformation of the bottom cover slip by the pushing lens. Adapted from *Berard, Daniel, et al. "Precision platform for convex lens-induced confinement microscopy." Review of Scientific Instruments 84.10 (2013): 103704.*, with the permission of AIP Publishing.

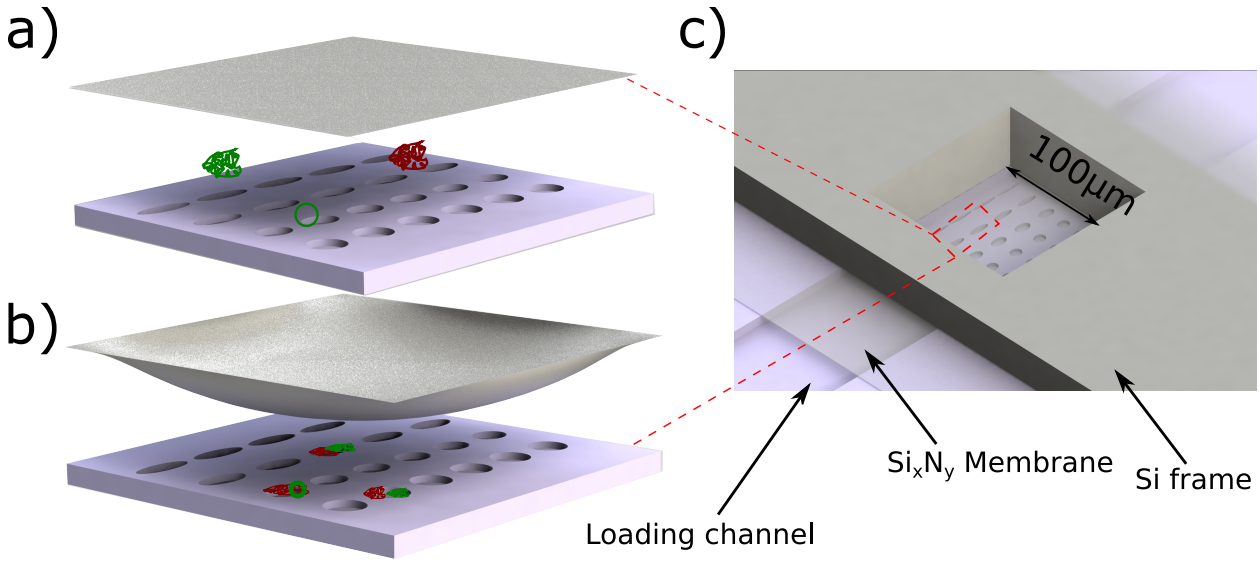

Figure 3.4: Schematic of the actuative nanofluidic device. a) Passive state of the device. DNA samples are loaded into the trapping region by applying pressure. b) Active state of the device. Silicon nitride membrane is flexed downward by applying pneumatic pressure. DNA samples are trapped within the cavities in the glass substrate. c) Zoom-out view of the device.

The device is a three-layer stack composed of a borosilicate substrate, a thin Low Pressure Chemical Vapor Deposition (LPCVD) deposited silicon nitride membrane and a silicon wafer substrate. The borosilicate substrate contains a microfluidic channel and an array of nanocavities. The silicon wafer is coated with silicon nitride membrane on both sides. The coated silicon wafer is subsequently anodically bonded with the borosilicate wafer. A central 100 μx100 μm port in the silicon wafer is opened via the Potassium hydroxide (KOH) etching process. The free standing nitride film is exposed and functions as a flexible lid.

3.3 Device fabrication

The array of nanocavities is defined by ebeam lithography with ZEP520A resist on the borosilicate wafer. The patterns are then transferred to the borosilicate wafer via reactive

ion etching. The etching recipe is optimized to create a smooth surface [82] and is timed carefully to get the 200±15 nm deep cavities, where the variation is across the wafer. The surface roughness R_a is less than 4 nm from the profiler, which is comparable to that of a polished borosilicate wafer. The microfluidic channel is subsequently defined by the standard UV lithography with S1818 resist and transferred to the glass wafer by RIE. Then, the silicon wafer with LPCVD coated nitride is anodically bonded to the etched borosilicate wafer. A piranha clean is performed on both the glass and the silicon wafer before bonding. Two wafers are stacked manually and any gas bubbles between the wafers are removed by pushing gently. The wafer stack is gradually heated to 350 ^{o}C during 1 hr. Then, three 1000 V 5 min voltage pulses are applied to the wafer stack to bond. Finally, the KOH window on the top side of the silicon wafer is opened by UV lithography and RIE. The free standing actuative membrane is released by KOH etching (30% KOH solution 80 ^{o}C). The detailed process workflow is shown in Fig. 3.5.

3.4 Device operation and microscope setup

The device is mounted on an inverted microscope via a 3D printed chuck, which allows for the application of pneumatic pressure and sample solution injection. The chuck is printed by a stereolithography 3D printer from Formlabs with Formlabs standard clear resin (using 25 μm resolution). The chuck is submerged in an IPA bath for 3 min after printing and the access channels are flushed manually with IPA to prevent blockage. A 15 min UV post-curing at 60 °C is applied to harden the chuck and remove the IPA residue. The chuck is interfaced to the device with a custom PDMS gasket with a 25% compression ratio and the device is secured onto the chuck by a stainless steel face plate. The nanofluidic chip is flushed with 1X tris buffer (10 mM Tris-HCl, pH=8.0) to remove any fabrication debris. The λ-DNA (48.5 kbp, linear topology) is stained with YOYO-1 and YOYO-3, T_4-DNA (169 kbp, linear topology) is stained with YOYO-3, and pBR322 (4361bp, ring

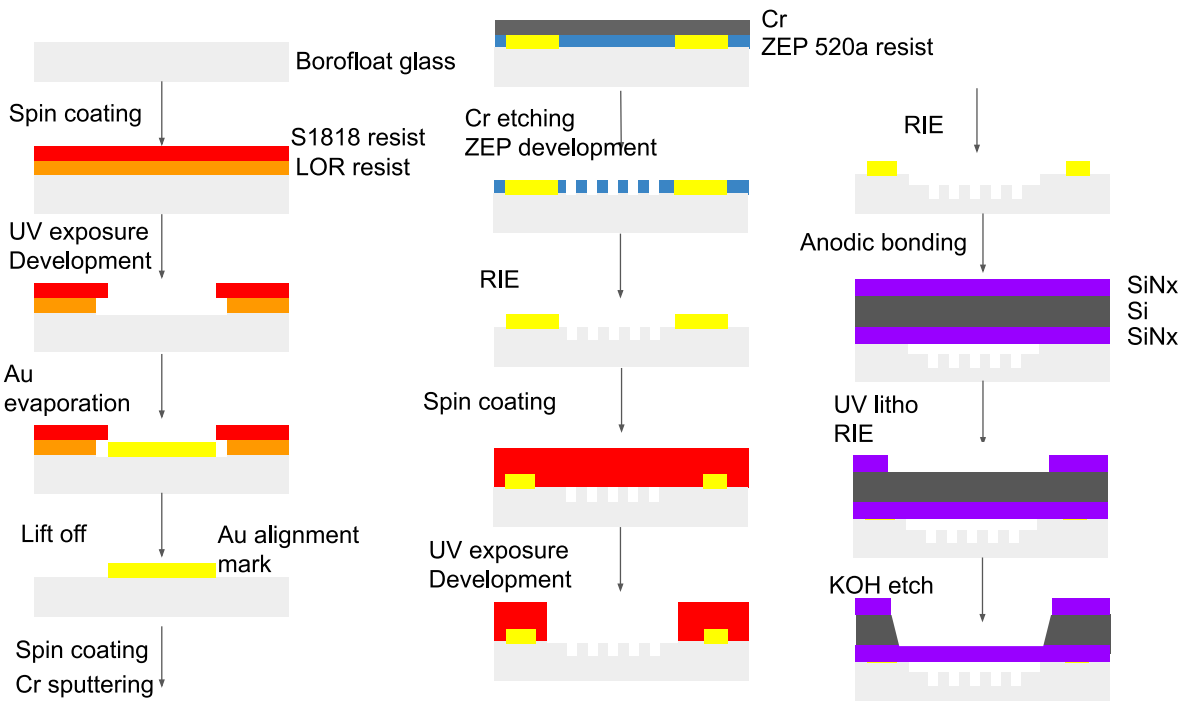

Figure 3.5: Flow chart of the fabrication process. The fabrication process begins with a bare 4-inch borosilicate wafer. A sequence of UV lithography, E-beam lithography, reactive ion etching, anodic bonding and KOH etching steps are then used to fabricate a device with A thin free standing silicon nitride membrane lid.

topology) is stained with YOYO-1. The staining ratio is controlled to 10:1 bp:fluorophore. The analytes are diluted to 2.5 μg mL^{-1} in 10 mM Tris (8.0 pH). β-mercaptoethanol (BME) 2% by volume is added to the sample solution prior to experiments to reduce photobleaching and photonicking. The DNA samples are pipetted into the loading reservoir. We use a syringe to load the DNA sample underneath the membrane by applying pressure. Once the DNA sample is underneath the membrane, the loading pressure is removed and the DNA samples are allowed to relax to reach an equilibrium conformation. The membrane lid is controlled via a Fluigent Flow EZ pump. By applying pressure greater than 1000 mbar, the membrane touches the floor of the microfluidic channel. Note that by applying lower pressure, the distance between the membrane and the fluid channel can be controlled with sub-5 nm precision [83]. The trapping is repeated until DNA chains are successfully trapped. (see Fig. 3.6)

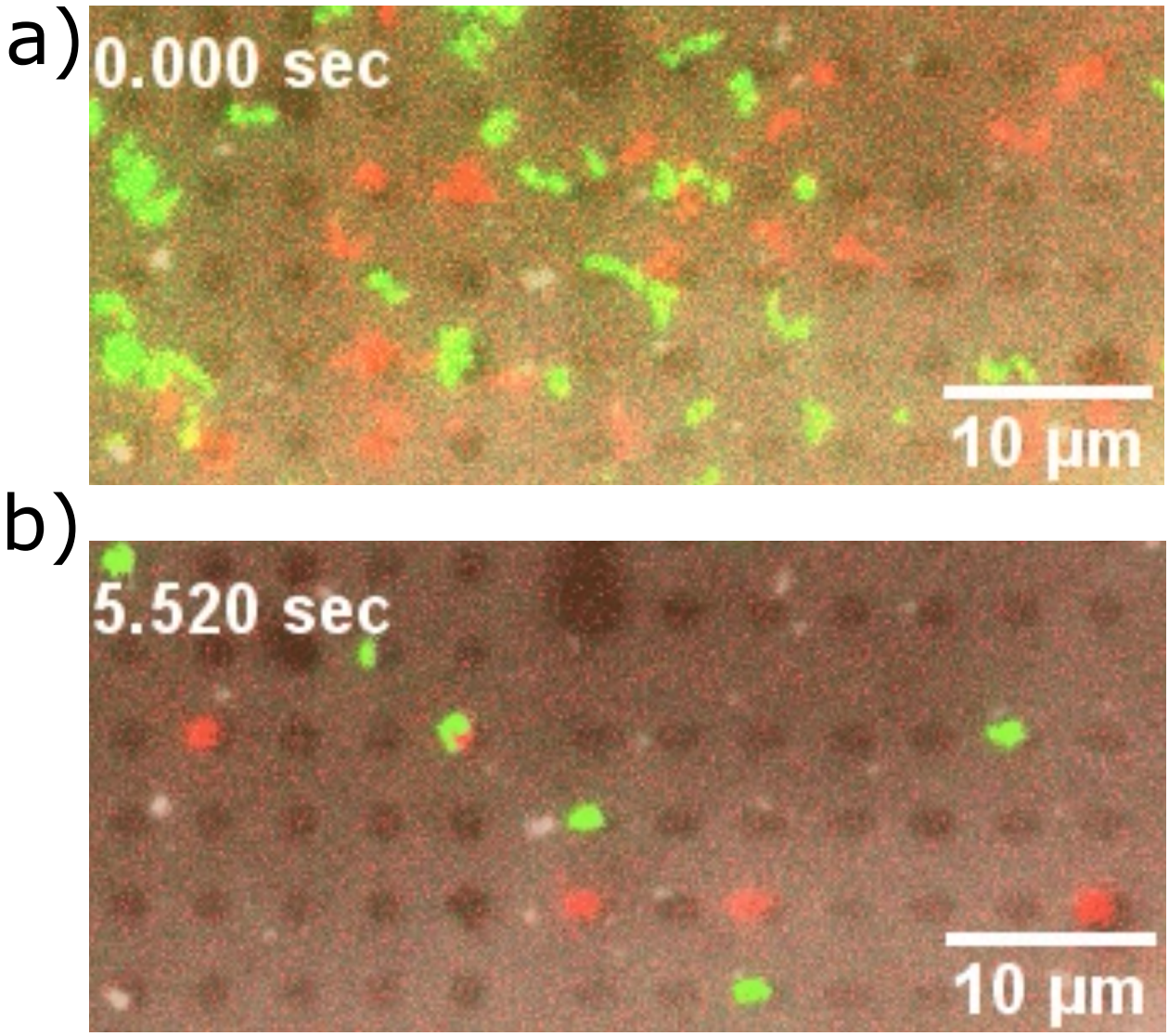

Figure 3.6: Differentially stained DNA chains are trapped in nanocavities. a) No pneumatic pressure is applied to the nitride membrane. b) Pneumatic pressure is applied to the nitride membrane. The cavity image is overlaid on the fluorescent image for clarity.

The fluorescent imaging commences after the desired combination of DNA molecules is trapped and has relaxed. The videos are taken on the Nikon Eclipse Ti inverted microscope with a Nikon Plan Apo VC 100x oil-immersion objective and a Teledyne Photometrics Prime 95B camera. The imaging system is controlled by the open-source software μ-Manager. We separate different colour fluorescent signals by using a spectrum splitter [53]. The camera captures different colour images at different regions of the chip to avoid significant time differences (greater than 1 ms) between channels. We configure the splitter based on the choice of the dye excitation/emission spectrum.

Different excitation lines are fired simultaneously to excite the corresponding fluorescent dye. The illumination is synchronized with the camera via a shutter trigger line. The exposure time is set ranging from 10 ms to 50 ms depending on the contrast of the images. Once a video is captured successfully, we release the membrane pressure and flush new DNA samples from the reservoir. The procedure is repeated until a sufficient amount of videos are captured.

3.5 Conclusion

In conclusion, we demonstrate multiple differentially stained DNA chains can be confined and sealed in the nanofluidic cavity smaller or comparable to their size. In particular, this technology could be used as an artificial cellular confinement environment to probe the interactions between molecules, or even organelles. As the confinement geometry and molecule of interest can be easily exchanged, this confinement method would serve as an in vitro playground to test physical principles that may play a role in more complex phenomena in bacteria.

Chapter 4

Confinement anisotropy drives polar organization of two DNA molecules interacting in a nanoscale cavity

In this chapter, we approach the problem of chromosome segregation and plasmid partitioning via an *in vitro* approach, demonstrating that a very simple nanofluidic model can give rise to fundamental behaviors observed in bacteria. In our study, a pneumatically actuated nanofluidic platform is used to confine *two* differentially stained DNA molecules in elliptical compartments with variable anisotropy. Increasing compartment anisotropy leads to a symmetry breaking phenomenon whereby the chains segregate to either side of the elliptical boxes. Secondly, by confining a larger dsDNA molecule and a small plasmid in the elliptical boxes, we show that entropy-driven demixing gives rise to a ring-like and polar distribution of the plasmid due to the symmetry mismatch between polymer-polymer exclusion and wall-polymer interaction. This entropy-driven organization in turn leads to a distinct pole-swapping dynamics where molecules switch ellipse poles via Brownian dynamics in the non-uniform potential landscape created by the DNA-DNA interactions. Finally, we introduce small inert molecules (dextran, diameter $\sim 2.6\,\mathrm{nm}$) into

the plasmid–T_4-DNA confinement system to simulate the effect of molecular crowding. We observe that a high concentration of dextran (volume fraction $\mathrm{v}_\phi = 6.3e-2$) alters the plasmid probability density in a manner that depends on the overall cavity anisotropy. Specifically, for circular and anisotropic cavities, crowders displace the plasmid probability density inwards from the cavity edges while also enhancing segregation of plasmids from the cavity center towards the cavity edges.

This chapter is the integral text from:

Confinement anisotropy drives polar organization of two DNA molecules interacting in a nanoscale cavity.

Liu, Zezhou, Xavier Capaldi, Lili Zeng, Yuning Zhang, Rodrigo Reyes-Lamothe, and Walter Reisner. *Nature communications* 13, no. 1 (2022): 1-12.

4.1 Abstract

There is growing appreciation for the role phase transition based phenomena play in biological systems. In particular, self-avoiding polymer chains are predicted to undergo a unique confinement dependent demixing transition as the anisotropy of the confined space is increased. This phenomenon may be relevant for understanding how interactions between multiple dsDNA molecules can induce self-organized structure in prokaryotes. While recent *in vivo* experiments and Monte Carlo simulations have delivered essential insights into this phenomenon and its relation to bacteria, there are fundamental questions remaining concerning how segregated polymer states arise, the role of confinement anisotropy and the nature of the dynamics in the segregated states. To address these questions, we introduce an artificial nanofluidic model to quantify the interactions of multiple dsDNA molecules in cavities with controlled anisotropy. We find that two dsDNA molecules of equal size confined in an elliptical cavity will spontaneously demix and orient along the cavity poles as cavity eccentricity is increased; the two chains will

then swap pole positions with a frequency that decreases with increasing cavity eccentricity. In addition, we explore a system consisting of a large dsDNA molecule and a plasmid molecule. We find that the plasmid is excluded from the larger molecule and will exhibit a preference for the ellipse poles, giving rise to a non-uniform spatial distribution in the cavity that may help explain the non-uniform plasmid distribution observed during *in vivo* imaging of high-copy number plasmids in bacteria.

4.2 Introduction

Biological systems exploit phase transition physics to ensure their proper organization and function [1]. Liquid-liquid phase transitions are now believed to account for the formation of membrane-less organelles, such as P granules [2]; 2D phase separations between liquid-disordered and liquid ordered lipid phases [3] may give rise to the phenomenon of lipid microdomains (lipid rafts) [4]. In these classic examples, the phase separation is driven by the collective weak interaction of many small molecules (e.g. proteins, lipids).

Phase separation can also be induced by the interaction of larger but less numerous dsDNA polymer molecules [5]. Counterintuitively, whereas entropy maximization favors mixing of small particles in the absence of attractive interactions, long polymer chains are predicted to demix, due to the higher excluded-volume and thus lower entropy, of the non-mixed conformations [6]. A typical prokaryotic cell contains multiple large and freely interacting DNA molecules, such as primary/secondary chromosomes [7] and plasmids. As prokaryotes lack a separate nuclear compartment, these multiple dsDNA molecules are free to interact within the cell volume. entropy-driven demixing of dsDNA molecules can thus affect internal prokaryotic organization and function. S. Jun et al. famously suggested that entropic polymer demixing could provide the driving force behind bulk chromosomal segregation in dividing bacteria [5, 6]. More recently, entropic polymer

demixing has attracted attention as a possible mechanism to explain the non-uniform distribution of plasmids observed in live-cell imaging of *E. coli* [8, 9, 10, 11], including a tendency for plasmids to localize at the poles [8] and in a ring at the periphery of the bacterial chromosome [9]. This may in turn have implications for the partitioning of high-copy number plasmids upon cell division [10].

A remarkable property of entropically driven polymer demixing is that the predicted mixing-demixing phase-space depends on the anisotropy of the imposed confinement; demixing is believed to be greatly enhanced in tube-like structures (e.g. nanochannels and rod-like bacteria) [12, 6]. While this phenomenon is predicted by classic scaling theories [6] and Monte Carlo simulation [12, 13, 14, 15], key questions remain regarding exactly how multiple polymer states are internally organized and fluctuate dynamically in confined volumes of varying anisotropy. How, in particular, does polar organization develop in a system of two confined polymers as the rotational symmetry of an initially isotropic confined volume is broken? What dynamic features emerge when anisotropy is introduced? Can polar organization develop spontaneously in a confined anisotropic system consisting of one large polymer and additional smaller polymer molecules (e.g. plasmids)? These fundamental polymer physics questions may have relevance for how shape anisotropy influences the organization of demixed polymer states in the corresponding bacterial systems (e.g. rod-like versus spherical versus box-shape bacteria). Using *in vivo* methods to probe these questions is challenging, due to the immense complexity of the biological systems—involving many overlapping molecular processes—and the inability *in vivo* to independently control physically essential system parameters without drastically altering cellular phenotype and functionality. In addition, as physical and active mechanisms can interact in complex ways, teasing out their distinct roles is not straightforward. For example, biological systems may exploit polymer driven demixing in certain contexts (e.g. entropy as a driver of chromosomal segregation), working in concert with active systems [16], while in others the same physical effect may be biologically undesirable (e.g.

polymer demixing can expel large plasmids from the nucleloid), so that additional active mechanisms are needed (e.g. a special partitioning system for large plasmids) [11].

Lastly, focusing only on specific *in vivo* systems may obscure understanding of how the system behaves physically over a larger parameter space (i.e. a parameter space defined in terms of gross biophysical parameters like cell size, degree of anisotropy in the cell geometry, number of chromosomes/plasmids, sizes of chromosomes/plasmids and degree of crowding). Specific *in vivo* systems occupy only narrowly defined regions of this space. However, exploring the physical behavior over much larger portions of the space, even parts of the space that do no contain viable organisms, is essential to probe the underlying physics and can place existing *in vivo* systems in a larger context, for example shedding light on differences between species that occupy different points in parameter space [6], or physical constraints critical for cellular viability.

In this communication we develop a drastically simplified model system, containing two dsDNA molecules interacting in an elliptical nanoscale compartment (Fig. 4.1), to serve as a minimal model to explain how polymer-polymer interaction in anisotropic confinement can give rise to states with polar organization. Note that our choice of an elliptical geometry is designed to emphasize behavior that arises purely from confinement anisotropy, rather than features that might arise from geometries specifically mimicking a given biological system. Firstly, by confining two differentially stained dsDNA molecules of equal size in elliptical compartments of varying eccentricity (Fig. 4.1**a**), we demonstrate that increasing compartment anisotropy leads to a symmetry breaking phenomenon whereby the chains segregate to either side of the elliptical boxes. This polar organization of the two chains at the ellipse poles can be understood as an orientational configuration transition that can be quantified by an order parameter analogous to that used for a liquid crystal isotropic to nematic transition. Secondly, by confining a larger dsDNA molecule and a small plasmid in the aforementioned structures (Fig. 4.1**b**), we show that entropy-driven demixing can give rise to a ring-like and polar distribution of

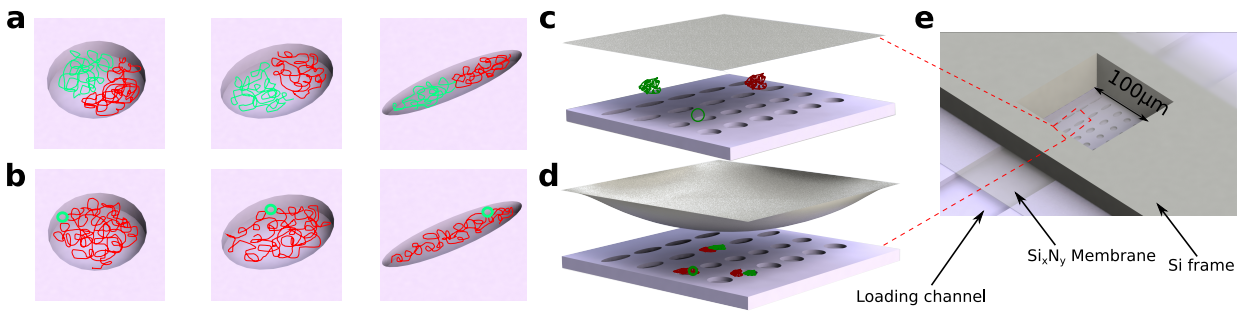

Figure 4.1: Schematic of the experimental concept and setup. **a**. Schematic of two differentially stained equal sized dsDNA molecules confined in elliptical compartments of varying eccentricity. **b**. Schematic of a larger dsDNA molecule and a plasmid molecule confined in the same structures. **c-d**. Molecular confinement is induced mechanically by using pneumatic pressure to depress a thin membrane lid. Depression of the lid traps the molecules in nanoscale cavities embedded in the floor of a nanoslit flow-cell **e**. Zoomed-out view of device: the cavities are defined in a nanoslit that is interfaced to the flexible membrane lid at a central window etched through a supporting silicon frame.

the plasmids, a phenomenon we find enhanced in the presence of molecular crowding. In particular, we find that the plasmid's polar distribution is driven by the symmetry mismatch between polymer-polymer exclusion and wall-polymer interaction.

4.3 Results

4.3.1 Polar Organization of Two DNA Chains Confined in an Anisotropic Cavity

Our experimental system is based on a nanofluidic device consisting of an array of elliptical cavities embedded in a nanoslit (Fig. 4.1**c**-**e**). The cavities have eccentricities e ranging from 0 to 0.9 (Fig. 4.1**a**,**b**) and are designed so that their volume is held constant as the eccentricity is increased. The nanoslit is bonded to a flexible lid that can be deflected downwards via pneumatic pressure, trapping molecular species in the cavities (Fig. 4.1**c**,**d**), a principle now exploited in a number of single-molecule confinement studies [17, 18, 19,

20, 21, 22]. The cavity devices are etched 200 nm deep and have a maximum diameter that ranges from 2 μm (for $e = 0$) to 3 μm (for $e = 0.9$).

In our first experiment, we introduce λ-DNA into the device; λ-DNA has a gyration radius of 0.7 μm, sufficiently large so that when two λ-DNA chains are trapped in a single cavity their lateral conformation and organization will be influenced by the confinement. The λ-DNA consists of a mixture of molecules stained with two different dyes (YOYO-1 and YOYO-3). Once driven beneath the flexible membrane via pressure actuated flow, the molecules are isolated in the cavities by depressing the lid, a procedure that is repeated until two differentially stained molecules are trapped, enabling independent monitoring of their conformation. Figure 4.2**a** shows a montage of fluorescence micrographs of the cavity confined chains. For a cavity with $e = 0$, the molecules displace each other towards the cavity edges, forming an opposed pair that undergoes brownian rotation about the cavity center. This effect, which follows closely the behaviour observed in a square cavity [21], is driven by volume exclusion between two-chains, which leaves the center of the cavity unfavorable to the two chains. When cavity eccentricity is introduced, the rotational symmetry is broken, and the molecules spend more time at the ellipse poles. At high eccentricity, the two chains adopt a strongly polar organization, with the chains stochastically swapping poles after a certain dwell-time.

To quantify the symmetry breaking of the λ-DNA spatial organization, we extract the chain positions $\mathbf{r}_1$ and $\mathbf{r}_2$ by computing the fluorescence center-of-mass for each chain. Histograms of the combined $\mathbf{r}_1$ and $\mathbf{r}_2$ values yield the probability P_{CM} of finding a chain center at some position within the cavity (Fig. 4.2**b**). The corresponding free-energy landscape $F_{\text{CM}} = -k_B T \log P_{\text{CM}}$ is also shown (Fig. 4.2**c**). Figure 4.2**b,c** clearly indicate the breaking of rotational symmetry as cavity anisotropy is increased. For cavity with $e = 0$, P_{CM} has a donut shape, consistent with Brownian rotation of chains symmetrically displaced from the cavity center. For $e = 0.3, 0.6$, P_{CM} appears as an elliptical donut ($e = 0.3, 0.6$). For $e = 0.9$, P_{CM} is peaked at the cavity poles, indicating fully polar seg-

regation. This behavior reflects the underlying evolution of the two chain free-energy landscape from a ring to a double-well shape. For eccentricity values below $e = 0.6$, the free energy minima lies near the cavity rim and circuits the ellipse. At $e = 0.6$ distinct free energy wells form at the ellipse poles, indicating a fully polarized state.

The separation vector $\mathbf{r} = \mathbf{r}_1 - \mathbf{r}_2$ serves as an additional measure of symmetry breaking, tracking the self-alignment of the two-chain system along the cavity long-axis. Let θ correspond to the angle between **r** and the ellipse semi-minor axis (Fig. 4.2**d**). The distribution of θ (Fig. 4.2**e**), as eccentricity is increased, moves from a flat distribution indicating no alignment to a distribution peaked at $\frac{\pi}{2}$, indicating that the two-chain system aligns along the semi major axis. The peaking of the angular distribution leads to a corresponding increase in the order parameter $S = 2\langle \cos^2(\theta) - \frac{1}{2} \rangle$.

Molecules trapped in the polar proximal free energy wells can stochastically swap their position due to thermal assisted escaping across the free energy barrier (Fig. 4.2**c**). We measure the stochastic pole swapping by monitoring the projection of **r** along the semi-major axis. This quantity changes sign when a swap occurs. Figure 4.3**a,b** gives an example of the time-series of the projected separation vector normalized to half the cavity extent (for $e = 0.6$ and $e = 0.9$). The time series indicate a two-state profile. When two chains attempt to swap positions but fail, a sharp peak (or dip) in the projected value will arise and the separation vector will revert to its original value (e.g. see Fig. 4.3**a**, green solid line). A successful attempt forms a raising (or falling) edge accompanied by a flip in the separation vector polarity (e.g. see Fig. 4.3**b**, green solid line). With increasing eccentricity, swapping events become less frequent.

The system dwell-time Δt in a given polar proximal state is exponentially distributed (i.e. $P(\Delta t) \sim e^{-\frac{\Delta t}{\tau}}$), as expected for a system with a constant escape rate [23] (Fig. 4.3**c**). We observe that the average dwell-time τ, extracted from the exponential fits to the cumulative probability distribution (see Supplementary Note. 1), is monotonically increasing with the cavity eccentricity (Fig. 4.3**d**). The increased average dwell-time is consistent

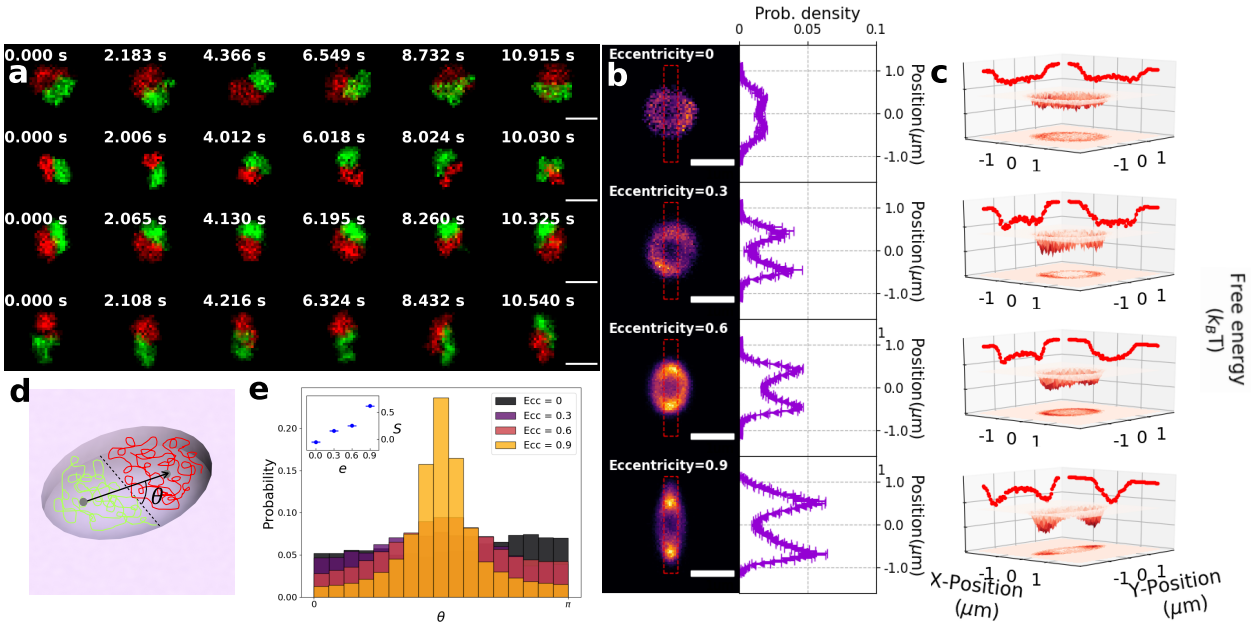

Figure 4.2: Experimental results and equilibrium analysis for two cavity confined DNA chains of equal size. **a**. Montage of fluorescence images of two λ-DNA molecules confined in elliptical cavities with varying eccentricity (the eccentricity values, ranging top to bottom, are 0.0, 0.3, 0.6 and 0.9). The scale bars are 2 μm and the time lapse between consecutive images is about 2 s. **b**. Probability of finding a chain center at certain position within the cavity. The cross-section of the probablity density distribution, labeled with red dashed box, is shown next to the heatmap.The error bars denote the standard deviation of the probability density. **c**. Free energy landscape within the cavity. The red lines indicate the projection of the landscape along the corresponding direction. **d**. A cartoon giving the definition of the separation vector and θ. **e**. The resultant θ-distribution for cavities of varying eccentricity. The inset shows the extracted order parameter. The error bars denote the standard error of the mean.

with the increasing free energy barrier between the two pole proximal free energy wells (Fig. 4.2**c**). As illustrated in Kramers' expression [24], $\tau \sim e^{\frac{\Delta F}{k_B T}}$ with ΔF is the free-energy barrier between two states. Qualitatively, note that increasing cavity eccentricity limits space in the cavity waist, yielding a higher free-energy barrier for the two chains to squeeze past each other in pole-reversal (Fig. 4.3**b**).

4.3.2 entropy-driven plasmid segregation

Next, we explore the interaction between a larger, linear DNA molecule (T_4-DNA, 166 kbp) and a plasmid vector (pBR322, 4361bp) confined in an elliptical cavity (Fig. 4.4). The molecules are differentially stained, as before. Figure 4.4**a** gives a montage of fluorescence micrographs of the interacting molecules. For cavities with low eccentricity, the plasmid tends to reside at the cavity periphery, diffusing in a narrow band between the T_4-DNA and the cavity side-walls. As the eccentricity increases above 0.9, the plasmid shows a preference for the cavity pole, yet undergoes stochastic switching between the poles by sliding between the T_4-DNA and the cavity side-wall. These qualitative observations on plasmid localization are confirmed via histograms of the plasmid position in the presence of the T_4-DNA for each eccentricity (Fig. 4.4**b**). Evidently, while the plasmid can penetrate the T_4-DNA, exclusion is sufficiently strong to ensure that the plasmid is most probably located on a ring circumventing the cavity periphery. For cavity eccentricity greater than 0.9, peaks of plasmid localization probability at the poles becomes evident, and there is a suppression of localization probability in the cavity mid-section. The T_4-DNA is centered in the cavity with remarkable precision, with a standard error of the mean of the center-of-mass position less than 1% of the cavity width. Self-centering of DNA in live *E. coli* is also reported by F. Wu et al. [25] Our experiment suggests that the self-centering of DNA chains can be achieved by conformational entropy regulated by the confinement geometry.

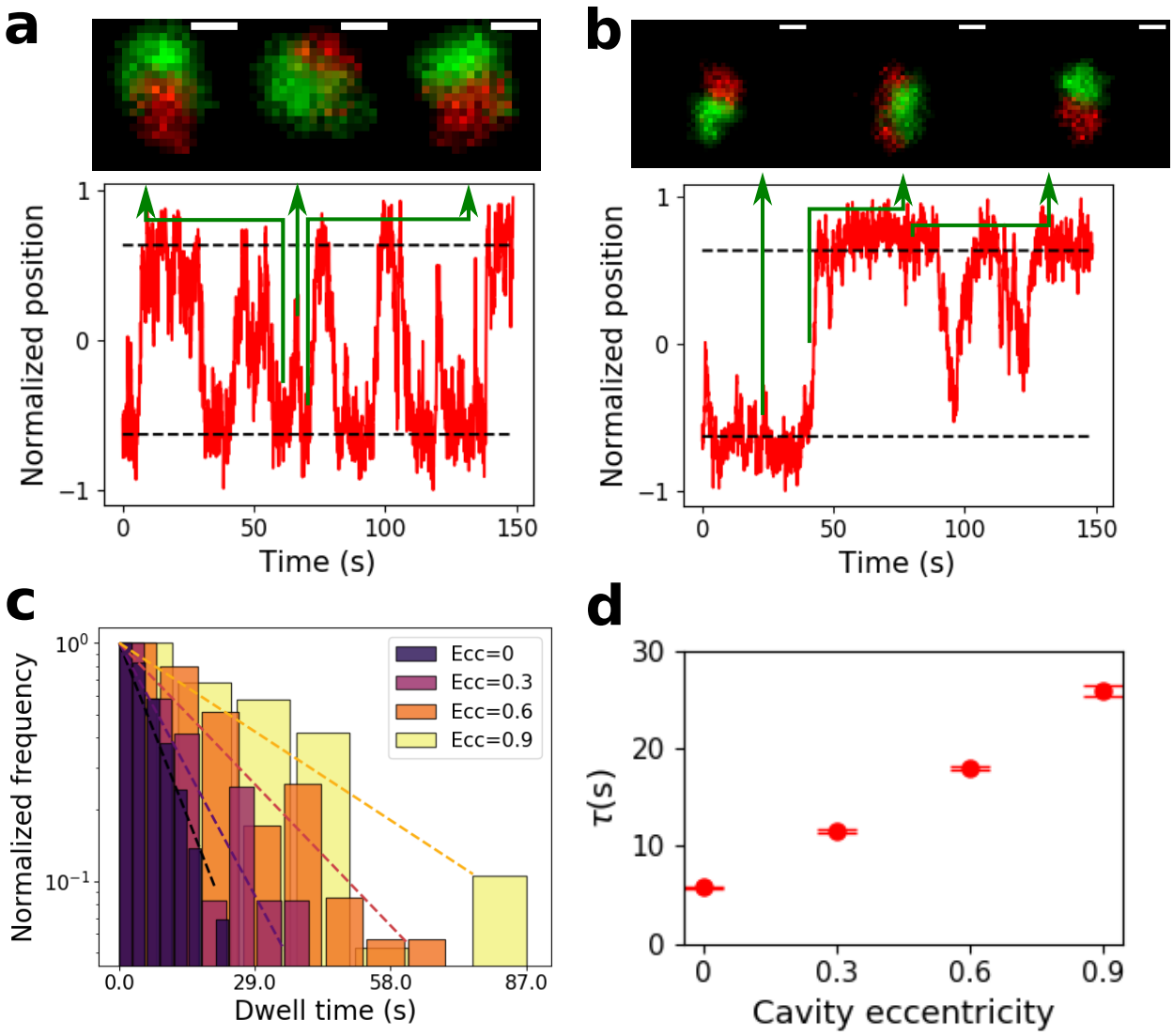

Figure 4.3: Experimental results and dwell time analysis for two cavity-confined DNA chains of equal size. **a,b**. Time series of separation vector projected along the semi-major axis (red-curve) for $e = 0.6$ and $e = 0.9$ respectively. The projections are normalized to half the cavity extent, so localization of the configuration in a polar proximal free energy well corresponds to a value close to ± 1. The black dashed line shows the baseline of two states. The green solid lines indicate the time corresponding to the adjoining image. In **a**, the two chains attempt to flip but failed, forming a spike in the vector projection. In **b**, the two chains flip successfully, reversing the sign of the vector projection. The scale bars are $1\,\mu$m. **c**. Histogram of the dwell time for four eccentricities; overlaid dashed lines correspond to exponential fits. **d**. Mean dwell time verses cavity eccentricity, with the mean dwell time extracted from exponential fitting to the corresponding cumulative distributions. The error bars denote the fitting covariance.

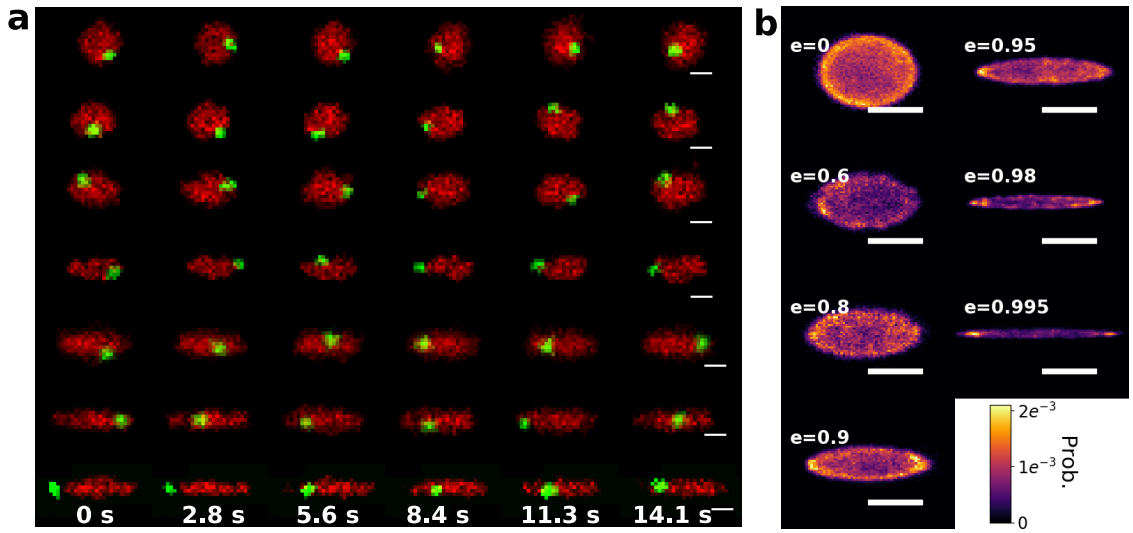

Figure 4.4: Experimental results and equilibrium analysis for a cavity confined plasmid in presence of T_4-DNA. **a**. Montage of fluorescence images of cavity confined T_4-DNA and plasmid DNA for cavities of varying eccentricity. The red color indicates T_4-DNA while the green indicates plasmid DNA. The scale bars are 2 μm. **b**. Histogram of plasmid-center position while confined with T_4-DNA, yielding an estimate of the probability density function for plasmid position in the cavity. The scale bars from top to bottom correspond to 1 μm, 1 μm, 1 μm, 1.2 μm, 1.2 μm, 1.6 μm and 1.6 μm.

4.3.3 A Model for Plasmid Segregation

We hypothesize that the observed plasmid probability density arises from the competition of two effects: (1) plasmid exclusion from regions of high T_4-DNA concentration and (2) a repulsive interaction of the plasmid with the cavity boundary. As the gyration radius of the T_4-DNA ($\sim$1.5 μm) is comparable to the cavity size, we treat the T_4-DNA as a semi-dilute polymer solution with a concentration profile given by the density function $\rho_{T_4}(\mathbf{r})$. The quantity $\mathbf{r}$ corresponds to a 2D position vector in the cavity. We evaluate $\rho_{T_4}(\mathbf{r})$ using a mean-field approach with ground-state dominance [26] appropriate for the slit-confinement [27]. In this approach, the concentration profile is determined by solution of a non-linear Schrödinger equation with $\rho_{T_4} = 0$ imposed at the cavity boundaries [27]. The corresponding interaction potential between the plasmid and the T_4-DNA at position

$\mathbf{r}$ is then proportional to $\rho_{T4}(\mathbf{r})$: $U_{T_4}(\mathbf{r}) = a\rho_{T_4}(\mathbf{r})$, with a being a proportionality constant related to the strength of exclusion between the plasmid and the T_4-DNA.

We argue that the plasmid interacts with each patch of arc-length ds along the cavity boundary via a potential $u_{\text{wall}}(\mathbf{r}_s - \mathbf{r})$, a function of the distance from the plasmid center position ($\mathbf{r}$) to the position of the particular boundary segment ds at arclength $s(\mathbf{r}_s)$. We choose an exponential form for u: $u_{\text{wall}}(\mathbf{r}_s - \mathbf{r}) = b\exp\left(-\frac{|\mathbf{r}_s - \mathbf{r}|}{r_b}\right)$, simply reflecting an interaction that decays over a length scale r_b (on order of magnitude of the distance the plasmid maintains from the cavity boundary). The quantity b characterizes the strength of the wall-depletion effect. In order to obtain the total boundary-interaction potential $U_{\text{wall}}(\mathbf{r})$, we integrate the contributions from each patch along the cavity boundary:

$$U_{\text{wall}}(\mathbf{r}) = \oint u_{\text{wall}}(\mathbf{r}_s(s) - \mathbf{r})ds \tag{4.1}$$

The plasmid explores the potential landscape stochastically via Brownian diffusion (Fig. 4.4**a**) with a particle position distribution $P(\mathbf{r})$ following the Boltzmann distribution $P(\mathbf{r}) \sim \exp(-U_p(\mathbf{r})/k_BT)$ [28, 24]; the potential experienced by the plasmid $U_p(\mathbf{r}) = U_{T_4}(\mathbf{r}) + U_{\text{wall}}(\mathbf{r})$. Numerical solution of the concentration profile $\rho_{T_4}(\mathbf{r})$ determines $U_{T_4}(\mathbf{r})$; this is performed using an open-source finite element PDE solver FreeFEM (see Supplementary Note 2) [29]. We fit the values of the parameters a, b and r_b by finding the values that maximize the cosine similarity [30] between the experimental plasmid position distribution and the modeled plasmid position $P(\mathbf{r})$.

The model plasmid probability density is shown in Fig. 4.5**a**, binned down to the same spatial resolution as the experimental results ($\sim 50\,$nm). We observe that the model qualitatively matches our experimental results, with the plasmid circumferential ring-shaped distribution and pole preference evident. For a more quantitative comparison with experiment, we compare the cross-section of the experimental and modeled plasmid probability distribution along the major- and minor- axis of the ellipse (Fig. 4.5**b,c** gives the

comparison for a cavity with $e = 0.9$. The cross-sections for additional cases are shown in Supplementary Note 3). Note that the positions of peak plasmid probability along the major axis, yielding the degree of polar segregation, agree well with the fitted model. The model also correctly describes the maximum concentration along the minor axis, which gives the position of the concentration ring. To explain intuitively why the plasmid segregates to the poles, we draw a portrait of the net potential experienced by the plasmid, plotting U_{T_4} and U_{wall} along the major axis (Fig. 4.5**d,e**). Note that the competition between the two potentials yields a segregation zone between the cavity center and the wall boundary. However, increasing the cavity eccentricity breaks the rotational symmetry of the potential landscape, so that the potential valley becomes deeper along the segregation zones that parallels the major axis. Also, the width of the valley, which can be observed qualitatively from Fig. 4.5**d,e**, is wider along the major-axis. Note that, for $e > 0.9$, the agreement between the model and measured plasmid position breaks down; this necessarily arises as our modeled T_4-DNA concentration distribution is no longer accurate [27] when the cavity becomes so elongated as to become tube-like and DNA semiflexibility plays a significant role. In the future, this problem may be addressed by more accurate modeling of the confined T_4-DNA concentration profile using self-consistent mean field approaches that can incorporate DNA semiflexibility [31, 32].

The underlying physics determining the boundary potential is complex, involving repulsive electro-static interactions [33, 34] between the plasmid and the cavity boundary and the degree to which the plasmid can be compressed as it is squeezed against the cavity wall. However, we expect that the range of the boundary potential is roughly related to the plasmid size. We determine the interaction range of the boundary potential as the point where it reaches $\sim 2k_BT$ (corresponding to a suppression of plasmid occupancy of around 90%). Using the fitted values of r_b and b, we find that the fitted boundary potential reaches $\sim 2k_BT$ at a distance of 190$\pm$8 nm from the cavity boundary. This value is indeed on order of magnitude of the true plasmid size; the radius of gyration R_g of

the 5.76 kbp supercoiled plasmid is measured to be 102 ± 2 nm from the light scattering [35]. Note that, in our 10 mM Tris buffer, we expect the DNA effective width w to be around 10 nm [31], while the effective width is closer to 2 nm in the 200 mM NaCl buffer used for the light scattering measurements [35]. As the $R_g \sim w^{1/5}$ for a bulk self-avoiding coil [33], this suggests that the plasmid R_g is closer to 140 nm in our buffer conditions. Regarding the parameter a, which determines the magnitude of self-exclusion, we find $a = (1.1 \pm 0.1) \cdot 10^{-6} k_B T \cdot \mu m^3 \cdot bp^{-1}$. The repulsive term of the Flory energy [26] is $v \cdot k_B T \cdot \rho$ where v is the excluded volume and ρ is the polymer solution concentration defined by Kuhn monomer. The persistence length P of the DNA chain is 50 nm, therefore the diameter a_k of the Kuhn monomer is $a_k = 2P = 100$ nm. The contour length of the T_4-DNA is around 60 μm, yielding approximately 600 Kuhn segments for the T_4-DNA. After normalizing ρ to the number of the Kuhn segments, and approximating the plasmid as a sphere of radius r_p, the value of a gives out $r_p = 70 \pm 3$ nm, again the same order of magnitude with the result from light scattering [35]. To check that our conclusions do not depend on the detailed boundary potential used, we also explored a Weeks-Chandler-Andersen (WCA) form for $u_{\text{wall}}(\mathbf{r}_s - \mathbf{r})$, which rises more steeply than an exponential (see Supplementary Note 4). The WCA model yields similar agreement, reaching $2\, k_B T$ at a distance of 180±8 nm, and an excluded volume radius of 60 nm.

4.3.4 Plasmid Dwell Time at Poles

The plasmid residence time at the poles characterizes the partitioning stability. The plasmid is considered to be in the pole region when its position satisfies $|x| > l/3$, where x is the major-axis projection of the plasmid position vector and l is the maximum extension the plasmid can reach in the experiment (the cavity has a length of $2l$). The histogrammed dwell-time for the various cavities are shown in Fig. 4.6**a**. The histogram suggests two different time-scales, which are extracted from a double-exponential model fitting (see Supplementary Note 5). The longer time-scale increases with increasing eccentricity (see

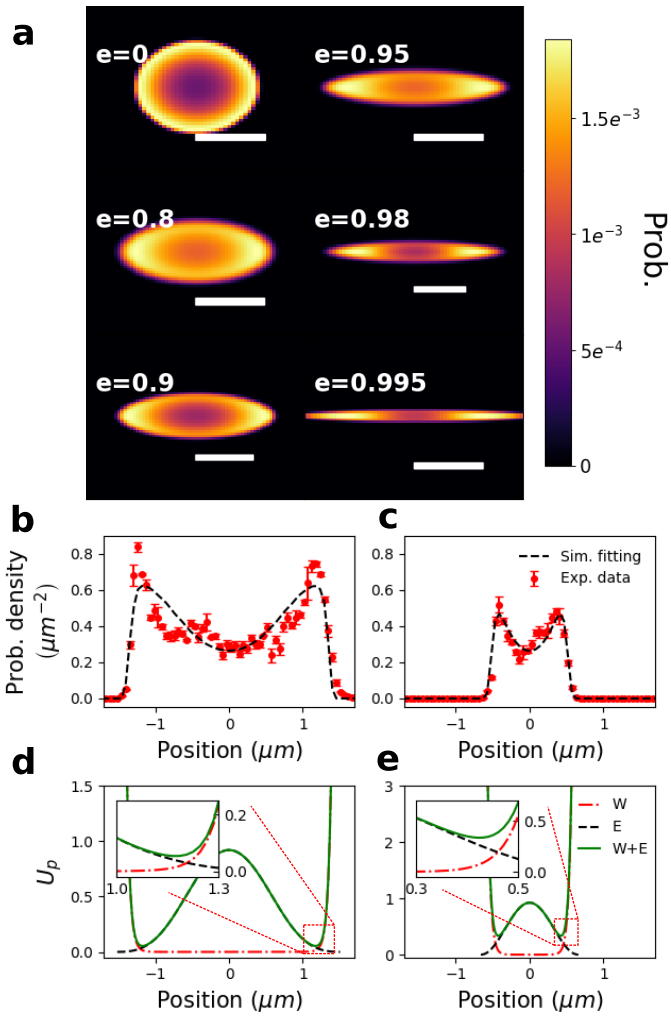

Figure 4.5: Modeling the distribution of plasmid position and comparison with experimental data. **a**. Fitted position distribution of the confined plasmid in cavities containing a single T_4-DNA molecule with eccentricity ranging from $e = 0$ to $e = 0.995$. The scale bars are 1 μm, 1 μm, 1.2 μm, 1.2 μm, 1.6 μm and 1.6 μm respectively for cavities with eccentricities ranging from $e = 0$ to $e = 0.995$. **b,c**. Plasmid probability density along the major (**b**) and minor (**c**) axis for $e = 0.9$. Experimental data are shown as red points, with error bars corresponding to the standard error of the mean of the binned counts ($n = 3$ bins for each point). Black dashed lines indicate the resulting fitted model plasmid probability density. **d,e**. Cross-sectional slices of the predicted potential along the major (**d**) and minor (**e**) axis for $e = 0.9$. The red dot-dashed line indicates the wall-potential; the black dashed line indicates the exclusion potential arising from the T_4-DNA; the green solid line indicates the superposition of both potentials. Note that a potential well forms at the overlap region between the repulsive wall-potential and the self-exclusion potential, with the insets giving the detailed behavior of the potential in the well vicinity.

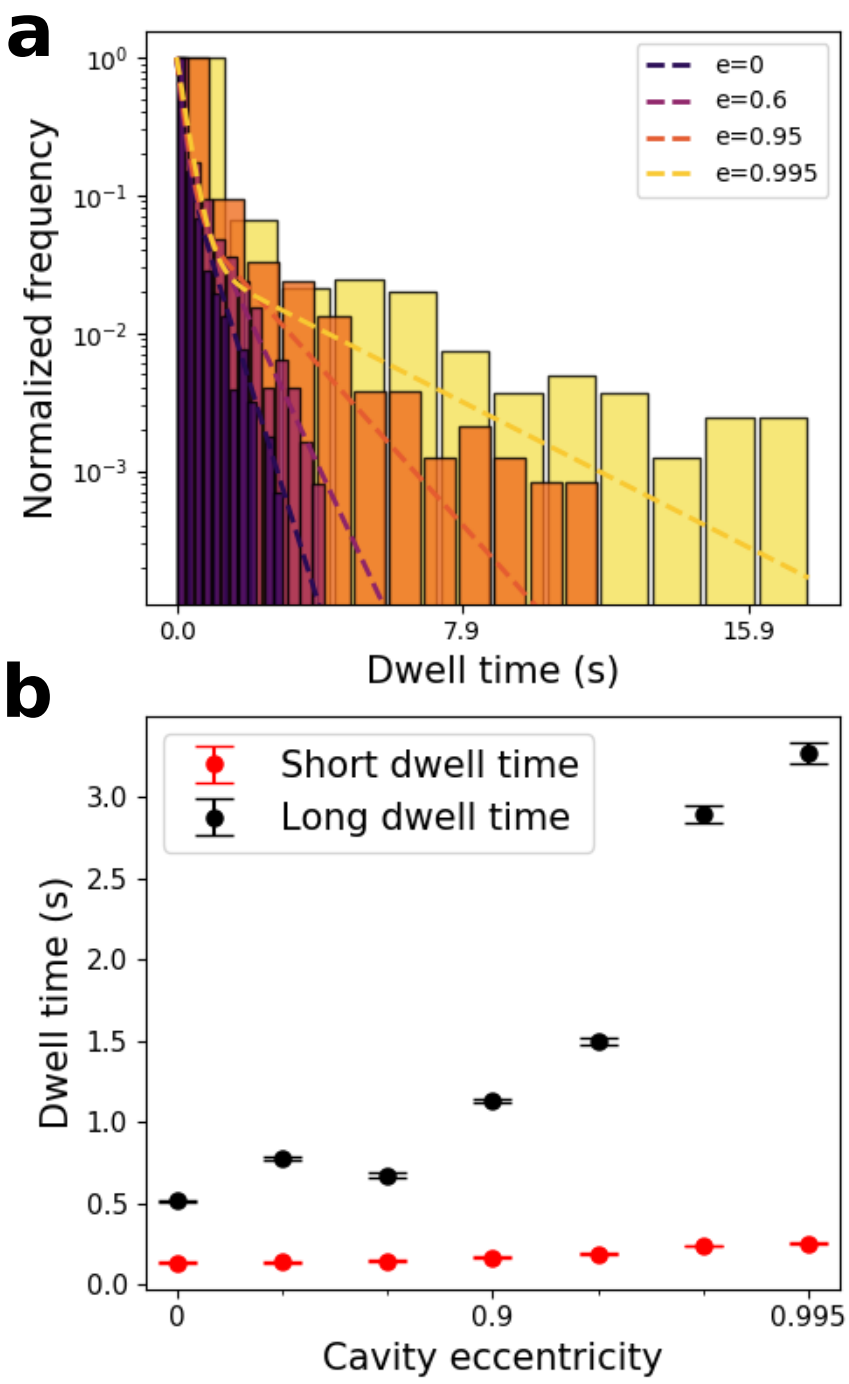

Figure 4.6: Dwell time analysis of a cavity confined plasmid in presence of T_4-DNA. **a**. Dwell time histograms for cavities of varying eccentricity with double-exponential fits. **b**. Resulting average dwell times extracted from double exponential fits to dwell-time histograms, with the black circles corresponding to the long average dwell-time and the red circles corresponding to the shorter average dwell time. The error bars denote the covariance from the fitting.

Fig. 4.6**b**). This time-scale corresponds to the mean dwell time of the plasmid at the cavity poles, and arises from the increased free energy barrier between the cavity pole and cavity waist (located between $\pm\, l/3$ by our definition of the pole region), also reflected by the reduced preference of the plasmid at the cavity waist in the plasmid position histogram in Fig. 4.4**b** and Fig. 4.5**a**. The shorter time scale arises from events that briefly cross the boundary at $|x| > l/3$ and then return towards the cavity center without experiencing the potential pocket at the poles (see Supplementary Note 5, in particular Supplementary Fig. 6).

4.3.5 Plasmid Mean-Squared Displacement

In addition we extract the plasmid's mean-squared displacement (MSD): $\langle(\Delta r)^2\rangle = \langle(\mathbf{r}(t)-\mathbf{r}(0))^2\rangle$. The MSD projected along the cavity major axis, $\langle(\Delta r)^2\rangle_{||}$, and minor axis $\langle(\Delta r)^2\rangle_{\perp}$, are shown respectively in Fig. 4.7**a** and **b** (also see Supplementary Note 6). Note that the saturating value of the MSD reflects the differing spatial extent of the confinement for the different cavities. For the short-time regime, the MSD shows a sub-diffusive behavior ($\alpha < 1$) in both directions. The scaling exponent of the MSD (α), determined from a power-law fit to the short-time regime (less than 1 s), is shown in Fig. 4.7**c-d**. The scaling exponent for the major axis MSD component increases slightly (Fig. 4.7**c**) while the minor axis component strongly decreases (Fig. 4.7**d**). In order to understand this behavior, we have performed a Brownian dynamics simulation for a particle undergoing a random walk in a free energy landscape derived from the observed plasmid position distribution (see Supplementary Note 7 for details on simulation methodology). Specifically, we derived the free energy from $F_{\text{CM}}(\mathbf{r}) = -k_B T \log P_{\text{plasmid}}(\mathbf{r})$, where $P_{\text{plasmid}}(\mathbf{r})$ is the fitted probability distribution of the plasmid position in the cavity (i.e. shown in Fig. 4.5**a**). We would expect, if the observed MSD behaviour results purely from the particular non-uniform structure of the potential landscape, that these simulations would agree with our measurements. We indeed find that the observed trend and exponent values for the MSD

major axis component agrees well with simulation (Fig. 4.7**c**), suggesting that the sub-diffusive behavior arises largely from the non-uniformity of the free energy landscape. The MSD minor axis component, however, falls more steeply than the simulation results, with the exponents showing much stronger sub-diffusive behavior (lower α, Fig. 4.7**d**). This behavior may arise as the plasmid diffusivity is influenced by interaction with the confined T_4-DNA, which relative to the plasmid, acts effectively like a section of a larger polymer solution. Small particles are well-known to exhibit a size-dependent anomalous diffusion in polymer solutions, i.e. departing from pure Stokes-Einstein diffusion, as the polymer solution can give rise to a non-continuum resistance at scales on order of the particle size [36, 37, 38, 39]. In particular, the particle diffusivity decreases as a function of polymer volume fraction [37, 38, 39], and sub-diffusive regimes have been observed [37, 40]. We suggest that these anomalous effects are observed for the minor axis, and not major axis MSD component, as the MSD minor axis component is sensitive to the plasmid's motion through regions of concentrated DNA along the central cavity axis (i.e. as occurs when a plasmid makes a perpendicular crossing across the cavity major axis). Note that we observe an absence of super-diffusive behavior ($\alpha > 1$), suggesting that super diffusion does not arise purely from polymer entropic and elastic recoiling forces, as hypothesized in T. M. Hsu et al [10].

4.3.6 Effect of Macromolecular Crowding on Plasmid Distribution

We introduce small inert molecules (dextran, gyration radius $\sim 2.6\,\text{nm}$) into the plasmid–T_4-DNA confinement system to simulate the effect of molecular crowding. We observe that a high concentration of dextran (volume fraction $v_\phi = 6.3 \cdot 10^{-2}$) alters the plasmid probability density in a manner that depends on the overall cavity anisotropy (Fig. 4.8**a**). Specifically, for circular and anisotropic cavities, crowders displace the plasmid probability density inwards from the cavity edges while also enhancing segregation of plasmids from the cavity center towards the cavity edges. We quantify the observed phe-

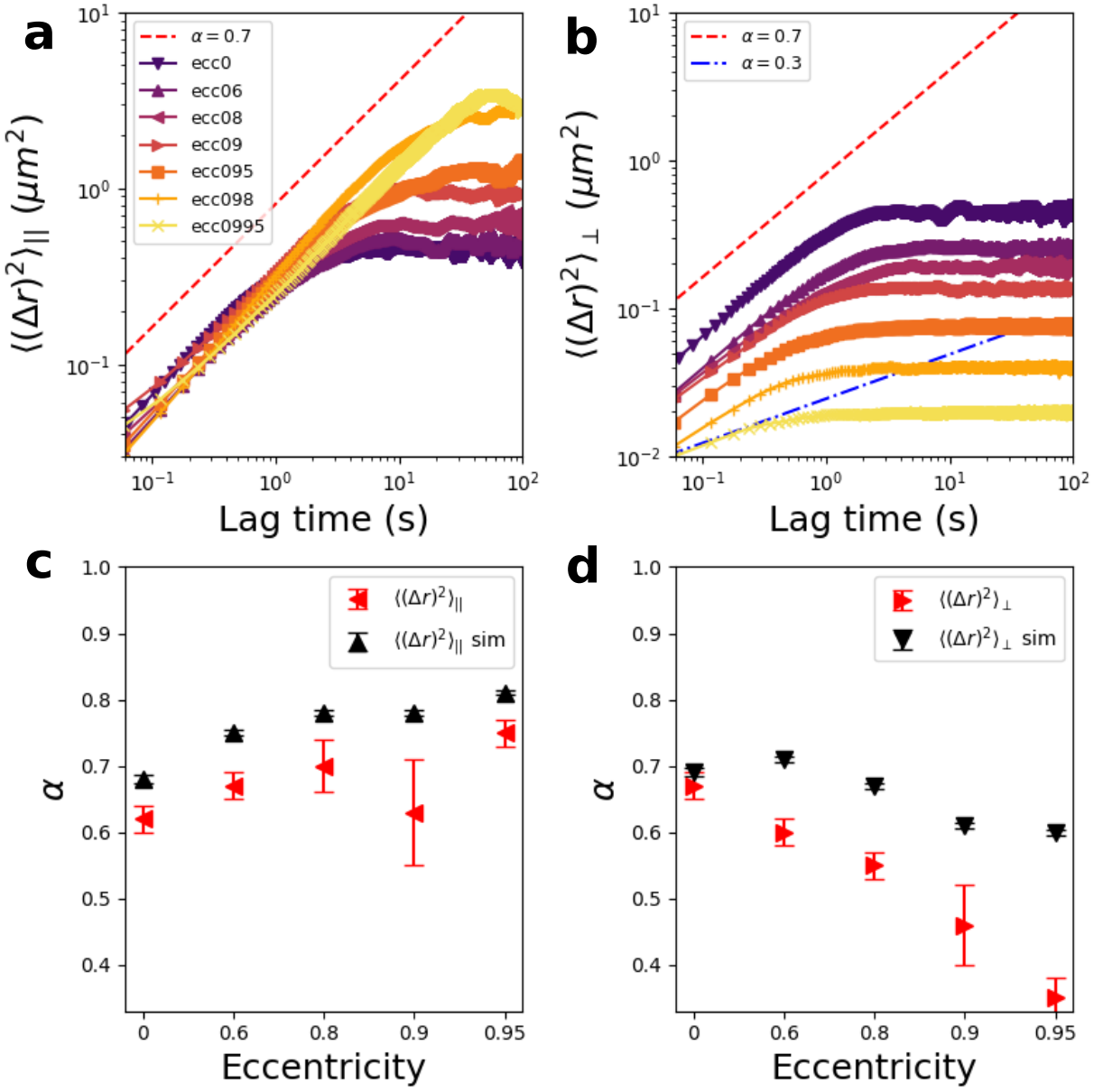

Figure 4.7: Mean-squared displacement of a cavity-confined plasmid in presence of T_4-DNA. **a**. The major axis component of the MSD extracted from the plasmid confined in different cavities. **b**. The minor axis component of the MSD extracted from the plasmid confined in different cavities. **c**. The scaling exponent of $\langle(\Delta r)^2\rangle_{||}$ extracted from experiments (red points) and simulations (black points). **d**. The scaling exponent of $\langle(\Delta r)^2\rangle_{\perp}$ extracted from experiments (red points) and simulations (black points). The red error bars give the standard error of the mean of α over captured videos ($n = 5$ for $e = 0$, $n = 7$ for $e = 0.6$, $n = 8$ for $e = 0.8$, $n = 9$ for $e = 0.9$, $n = 15$ for $e = 0.95$). The black error bars give the standard error of the mean of α over simulation clips ($n = 250$ clips with 3000 steps).

nomenon by measuring, for a circular cavity, a radially averaged plasmid probability density (Fig. 4.8**c**) and, for the anisotropic elliptical cavity, the plasmid probability density along cross-sections parallel and perpendicular to the cavity major axis (Fig. 4.8**b**) as well as the plasmid probability density averaged along an elliptical contour (Fig. 4.8**d**). We plot the plasmid probability density averaged over the elliptical contours versus an effective radial coordinate defined as $r_{\text{eff}} = \sqrt{\frac{x^2}{a^2} + \frac{y^2}{b^2}}$, where a and b correspond to the length of semi-major and semi-minor axis respectively. For purposes of quantifying shifts in the plasmid probability density, the distribution edge is defined as the position where the average plasmid probability density (in Fig. 4.8**c,d**) is equal to $\frac{1}{e}$ of its maximum. The effect of crowding is small for the symmetric cavity; here the plasmid probability densities with and without dextran are qualitatively similar, with only a small enhancement at the cavity edges present (Fig. 4.8**c**). For the symmetric cavity, crowders displace the plasmid probability density inward by $0.04 \pm 0.01\,\mu m$. However, the presence of anisotropy ($e = 0.9$) strongly enhances the effect of crowding. In the anisotropic cavity, the inwards displacement is a factor of four greater ($0.16 \pm 0.01\,\mu$m from the probability density averaged over elliptical cross-section; for comparison, displacement along the minor axis is $0.12 \pm 0.03\,\mu$m and the displacement along major axis is $0.18 \pm 0.03\,\mu$m). Additionally, the segregation effect, towards both the cavity periphery and poles, is amplified (Fig. 4.8**a,d**).

Neutral dextran nanoparticles are expected to influence the system purely entropically [41, 42, 43]. While crowders promote the compaction of T_4-DNA, yielding more space accessible to the plasmid, the crowders can also accumulate at the cavity perimeter [42], reducing the accessibility of the cavity edge. The plasmids then tend to occupy an intermediate region between the cavity edge, with its high concentration of crowders, and the central region of the cavity occupied by the T_4-DNA. The increased overall compaction of the T_4-DNA increases the T_4-DNA concentration in the cavity center and thus the influence of excluded-volume, enhancing the segregation effect of the plasmids relative to the T_4-DNA. Critically, anisotropy enhances the effect of crowding (in Fig. 4.8**a**,

eccentricity$= 0.9$). One possible explanation is that the chain conformation itself has a transient anisotropy [44] with increased elongation along a particular axis. In the symmetric cavity, this elongated axis can rotate freely, so that the plasmid and the crowders, which are much smaller than T_4-DNA, can maximize their accessible volume by moving in a coordinated fashion with the T_4-DNA (transiently occupying regions to either side of the elongated chain). However, in the anisotropic cavity, the more compact T_4-DNA aligns with the cavity major axis and is rotationally constrained. The crowders are thus forced to accumulate preferentially towards the cavity edge.

4.4 Discussion

In conclusion, using a nanofluidic model system, we demonstrate that anisotropic confinement can give rise to polar organization of a two-polymer system due to entropy-driven chain demixing. In our first experiment, we observe that as the cavity aspect ratio is increased, the two DNA chains will transition from a rotationally symmetric state that lacks polar ordering to a polarized state with a polar alignment of the chain center-to-center vector. In our second experiment, we observe that when a large DNA molecule is confined in an anisotropic cavity in the presence of a plasmid, the combination of excluded volume interactions and repulsive interactions with the cavity boundary will lead to the plasmid adopting a polar preference. These experiments illustrate physical principles that may play a role in more complex phenomena in bacteria. The first experiment shows how entropy-driven chain demixing can segregate two equal-size molecules in anisotropic confinement, which has been proposed as possible mechanism promoting chromosomal segregation in bacteria. The second experiment illustrates a principle that may help explain the observed distribution of high-copy number (hcn plasmids, $>$15 copies per cell) plasmids.

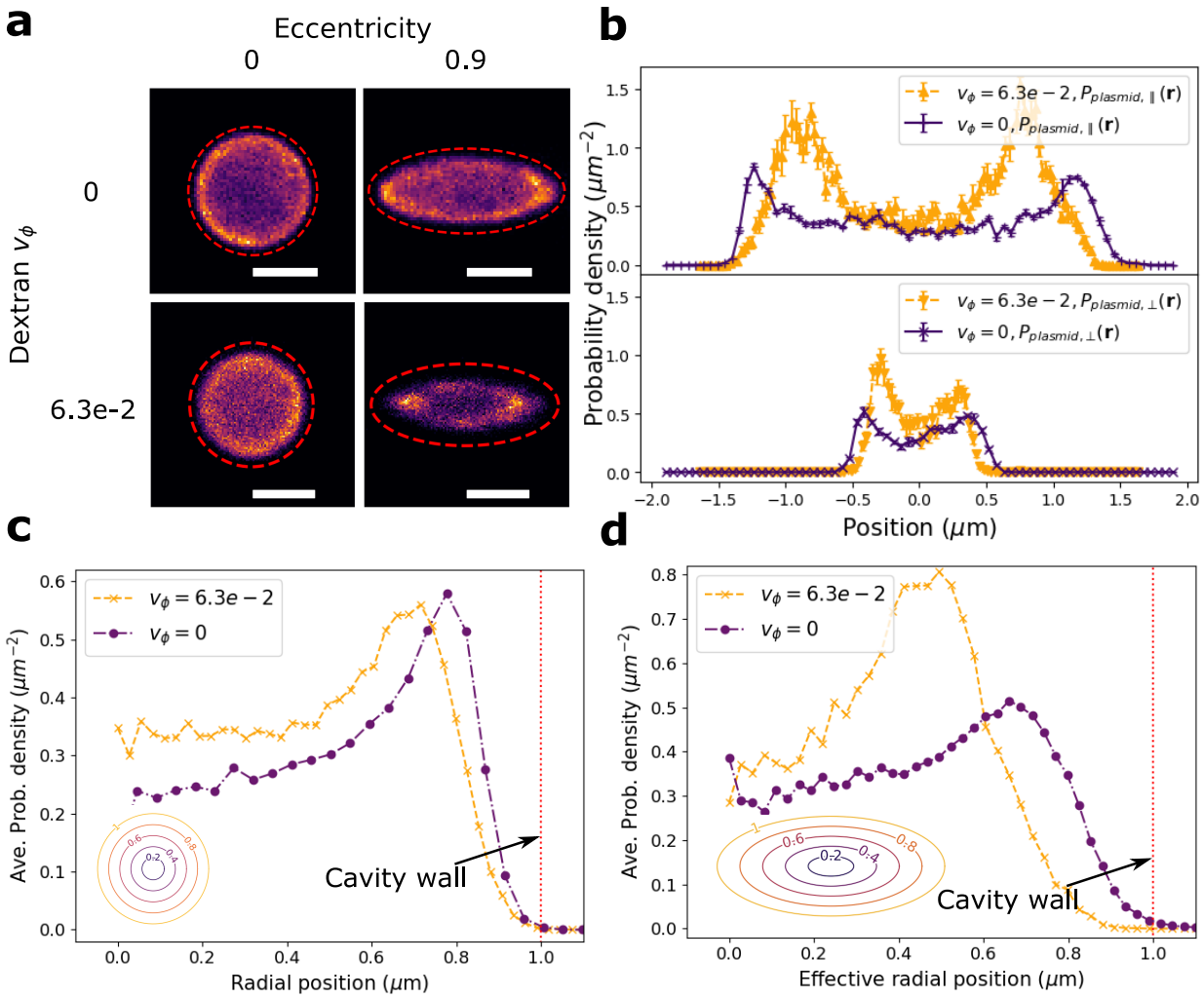

Figure 4.8: Experimental results for a cavity confined plasmid in presence of T_4-DNA with added macro crowders. **a**. Plasmid probability density in cavity, obtained from histogrammed plasmid position measurements, with and without crowding and for a symmetric and anisotropic cavity. The crowder volume fraction is $v_\phi = 6.3 \cdot 10^{-2}$ and the scale bars are $1\,\mu$m. The red dashed line gives the cavity edge. **b**. Cross-section of the plasmid position probability along the cavity major axis (upper panel) and along the cavity minor axis (lower panel). The length of the semi-major axis of the cavity is $1.51\,\mu$m. The length of the semi-minor axis of the cavity is $0.66\,\mu$m. The error bars denote the standard error of the mean of the binned probability density ($n = 3$ bins). **c**. Radially averaged plasmid probability density. The inset shows the contour along which the probability density average is taken. **d**. Plasmid probability density averaged over an elliptical contour versus effective radial coordinate $r_{\text{eff}} = \sqrt{\frac{x^2}{a^2} + \frac{y^2}{b^2}}$, where a and b correspond to the length of semi-major and semi-minor axis respectively. The inset shows the elliptical contours along which the probability density average is taken.

To expand on the second point, plasmids present at low-copy number (lcn) possess dedicated molecular machinery for ensuring proper partitioning upon bacterial division. In contrast, active partitioning mechanisms are not known to exist for plasmids present at high copy number [45]. While purely random partitioning can theoretically ensure stable transmission in the case of high copy number, *in vivo* imaging of fluorecently labeled plasmids in *E. coli* suggests that hcn plasmid partitioning is not random. In particular, the live-cell work suggests that the hcn plasmid distribution has a remarkable multi-focal character, with large multi-plasmid clusters present at the cell poles [8]. Observation of anti-correlation between nucleoid location and plasmid distribution suggest that this polar organization arises from nucleoid occlusion, i.e. the plasmids are physically obstructed from nucleoid proximal regions in the bacteria mid-section [8]. Super-resolution studies support but complicate this picture, indicating that the excluded plasmids are in fact roughly distributed in a ring around the nuceloid periphery, with a small degree of nucleoid penetration [9]. Recent polymer based simulations confirm that entropic forces will tend to segregate plasmid and chromosomal dsDNA, but predict that the exclusion is strongly size dependent, with larger plasmids ($>$100 kbp) tending to occupy the cell poles, and smaller plasmids excluded laterally about the nucleoid without showing pronounced polar organization [11]. Our measurements support the conclusion that the peripherial ring distribution and polar clusters arise from generic features of the entropy-driven interactions between large polymer chains, but go further in suggesting that the polar organization results from competition between excluded-volume interactions and repulsion from the anisotropic confining surfaces. Our findings additionally suggest that molecular crowding may influence the degree of plasmid segregation and polar accumulation and that the effects of crowding are enhanced by cavity anisotropy.

Note that, while bacterial chromosomes are $\sim$ Mbp in scale (e.g. the genome size of *E. coli* is 4.6 Mbp), much larger than the DNA sized used here (λ-DNA is 46.5 kbp, T_4-DNA is 166 kbp), the chromosomal systems do not necessarily contain more independent

chain units, due to their high degree of compaction arising from negative supercoiling and associated proteins. The structural unit of a chromosome is estimated to be between 10-300 kbp in size, giving rise to between 15-400 structural units [16]. In comparison, a bare λ-DNA and T_4-DNA molecule, for which the structural unit is the Kuhn length (100 nm or 300 bp), has respectively 145 and 500 structural units. Thus, due to the chromosome's strong degree of compaction, the chromosomal polymer model and the simple DNA model have an effective polymer size at least order of magnitude comparable. Note, however, that the more anisotropic chain unit in the simple DNA model may lead to subtly different scaling behavior of the chain free energy as our nanofluidic model may technically lie in an extended confinement regime [46, 16].

Our nanofluidic system, with a 200 nm height significantly smaller than the width ($\sim$ 1 μm), is slit-like. S. Jun et al. has suggested that slit-like systems should show enhanced segregation relatively to isotropic systems [6], which is consistent with what we observe; even in a circular cavity, the λ-DNA molecules do not instantaneously mix. However, note that there exist real biological systems that resemble our slit-like cavities. For example, *H. walsbyi*, an archea that is found world-wide in brine pools, has a stamp-like shape with a thickness of less than 0.2 μm and a width around $2 - 5$ μm [47]. During cell growth, *H. walsbyi* transforms from a square into a rectangular shape; this may induce anisotropic confinement that helps ensure chromosome partitioning prior to division [48].

From the point of view of simulation, model experimental systems, which contain a precisely calibrated degree of complexity, can help validate/calibrate simulation approaches [49] and thus serve as a stepping stone to modeling the full complexity of an *in vivo* biological system. In particular, our experiment gives us access to time-scales associated with the two-chain polymer dynamics. These time-scales can be challenging to access in simulations as computational approaches that can capture dynamics require unfeasibly long simulations times to model chains of a size approaching that of the chromosomal polymer models [49]. In the λ-DNA experiment, we observe a time-scale ~ 10 s

associated with molecule pole-swapping. The existence of this time-scale, which is much smaller than an overall bacterial generation time ($> 20\,\text{min}$ [50]), suggests an additional role for mechanisms that ensure anchoring of replication origins to cell poles [51] (i.e. entropic mechanisms may not be sufficient to ensure stable polar partitioning of chromosomes due to pole-swapping events). In the plasmid system, measurements of the MSD from single plasmid trajectories suggest that the observed scaling exponents are consistent with sub-diffusion, and that the observations of super-diffusive exponents in live cells [10] likely result from additional active mechanisms rather than entropic forces.

Our nanofluidic model permits a wide-range of additional experiments that can, following a "bottom-up philosophy" [52], explore the global significance of additional biological complexity on the overall entropy-driven chain demixing. Our addition of crowding agents to the plasmid–T_4-DNA model is an example of how we can increase system complexity step-by-step. Additionally, we could use circular DNA constructs to explore the role of circular chain topology. We could add variable numbers of plasmids and DNA molecules of varying size to simulate secondary chromosomes and different degrees of plasmid loading. The simple DNA constructs used here could be potentially replaced with extracted bacterial nuceloids [43] and the role of specific nucleoid associated proteins explored (e.g. H-NS and Fis proteins [53]).

A second potential application of our system is to attempt to elucidate certain poorly understood *in vivo* phenomena that appear impacted by nucleoid exclusion. In particular, the formation of localized aggregates of unfolded/mis-folded protein is a widespread phenomenon in bacteria [54]. These aggregates often appear at the cell-poles (as in the case in *E. coli* [54]), and form in response to proteotoxic stresses arising from cellular and environmental factors, for example decline in ATP levels, [54] heat shock,[55] antibiotic treatment, high levels of heterologous protein expression [56] and potentially cell aging [57] (although the correlation of aggregate formation with cell aging is under debate [58]). The aggregates are inheritable and associated with increased with increased

resistance to stress [55] with a close connection to persister phenotypes that can survive starvation and exposure to high levels of antibiotics [59, 60, 56]. The aggregates have been observed to freely diffuse in nucleoid free regions of the bacteria [61, 62], suggesting that entropic forces may play a role in their polar localization, analogous to the localization of the plasmids. In principle, protein aggregates, for example extracted from bacteria via centrifugation [63] and labeled via IbpA-YFP fusion proteins [55], could be introduced to our nanofluidic system to observe if polar organization occurs in the absence of any active mechanisms. Protein aggregates in non-stressed conditions often form at only one of the cell poles.[57] We suggest this may result due to competition between protein aggregates and other macromolecular components, such as plasmids, for polar locations (a hypothesis our nanofluidic model allows us to partially test, by exploring systems containing mixtures of plasmids and proten aggregates). Lastly, given that the geometry and molecular constituents of these model experiments are precisely known, the results can then be compared directly against molecular simulation, which will enable calibration of simulation predictions regarding the role of specific biological features.

4.5 Methods

4.5.1 Image analysis

We subtract background noise prior to the analysis using a noise subtraction algorithm proposed by J Tang et al. [64] implemented in ImageJ. The fluorescence center of mass (FCM) is then calculated for each frame via:

$$\mathbf{r}_{\mathbf{CM}}(t) = \frac{\sum \mathbf{r}(t) I(\mathbf{r}, t)}{\sum I(\mathbf{r}, t)} \tag{4.2}$$

The position data is then fed to a homemade open-source Python script to perform the remaining analysis (e.g. calculation of cavity probability distributions, free energy).

4.5.2 DNA-dextran sample preparation

Dextran with molecular weights $M_w = 5$ kDa was purchased from Sigma-Aldrich and dissolved in 10 mM Tris buffer. The tris-dextran buffer is mixed with plasmid–T_4-DNA containing buffer in equal volumes and incubated for 48 hrs with 2%v/v of BME added right before the experiments. The radius of gyration of the dextran molecules is calculated to be 2.6 nm via the empirical equation $R_g = 0.066 \cdot M_w^{0.43}$ with M_w in g/mol and R_g in nm [42].

Reference

[1] Chiu Fan Lee and Jean David Wurtz. “Novel physics arising from phase transitions in biology”. In: *Journal of Physics D: Applied Physics* 52.2 (2018), p. 023001.

[2] Clifford P Brangwynne et al. “Germline P granules are liquid droplets that localize by controlled dissolution/condensation”. In: *Science* 324.5935 (2009), pp. 1729–1732.

[3] Aurelia R Honerkamp-Smith, Benjamin B Machta, and Sarah L Keller. “Experimental observations of dynamic critical phenomena in a lipid membrane”. In: *Physical review letters* 108.26 (2012), p. 265702.

[4] Sara L. Veatch and Ilya Levental. “The continuing mstery of lipid rafts”. In: *Journal of Molecular Biology* 428 (2016), pp. 4749–4764.

[5] Suckjoon Jun and Bela Mulder. “Entropy-driven spatial organization of highly confined polymers: lessons for the bacterial chromosome”. In: *Proceedings of the National Academy of Sciences* 103.33 (2006), pp. 12388–12393.

[6] Suckjoon Jun and Andrew Wright. “Entropy as the driver of chromosome segregation”. In: *Nature Reviews Microbiology* 8.8 (2010), p. 600.

[7] Elizabeth S. Egan, Michael A. Fogel, and Matthew K. Waldor. “Divided genomes: negotiating the cell cycle in prokaryotes with multiple chromosomes”. In: *Molecular Microbiology* 56.5 (2005), pp. 1129–1138.

[8] Rodrigo Reyes-Lamothe et al. “High-copy bacterial plasmids diffuse in the nucleoid-free space, replicate stochastically and are randomly positioned at cell division”. In: *Nucleic Acids Research* 42.2 (2014), pp. 1042–1051.

[9] Yong Wang, Paul Penkul, and Joshua N Milstein. “Quantitative localization microscopy reveals a novel organization of a high-copy number plasmid”. In: *Biophysical journal* 111.3 (2016), pp. 467–479.

[10] Tai-Ming Hsu and Yi-Ren Chang. “High-Copy-Number plasmid segregation—single-molecule dynamics in single cells”. In: *Biophysical journal* 116.5 (2019), pp. 772–780.

[11] Charlène Planchenault et al. “Intracellular positioning systems limit the entropic eviction of secondary replicons toward the nucleoid edges in bacterial cells”. In: *Journal of molecular biology* 432.3 (2020), pp. 745–761.

[12] Axel Arnold and Suckjoon Jun. “Time scale of entropic segregation of flexible polymers in confinement: implications for chromosome segregation in filamentous bacteria”. In: *Physical Review E* 76.3 (2007), p. 031901.

[13] Youngkyun Jung and Bae-Yeun Ha. “Overlapping two self-avoiding polymers in a closed cylindrical pore: Implications for chromosome segregation in a bacterial cell”. In: *Physical Review E* 82.5 (2010), p. 051926.

[14] Youngkyun Jung et al. “Interchain ordering and segregation of polymers under confinement”. In: *Macromolecules* 45 (2012), pp. 3256–3262.

[15] James M Polson and Logan G Montgomery. “Polymer segregation under confinement: Free energy calculations and segregation dynamics simulations”. In: *The Journal of chemical physics* 141.16 (2014), p. 164902.

[16] Bae-Yeun Ha and Youngkyun Jung. “Polymers under confinement: single polymers, how they interact, and as model chromosomes”. In: *Soft Matter* 11 (2015), pp. 2333–2352.

[17] Min Ju Shon and Adam E Cohen. "Mass action at the single-molecule level". In: *Journal of the American Chemical Society* 134.35 (2012), pp. 14618–14623.

[18] Daniel J Berard et al. "Convex lens-induced nanoscale templating". In: *Proceedings of the National Academy of Sciences* 111.37 (2014), pp. 13295–13300.

[19] Michael Adrian Gerspach et al. "Pneumatically controlled nanofluidic devices for contact-free trapping and manipulation of nanoparticles". In: *Particle & Particle Systems Characterization* 35.12 (2018), p. 1800161.

[20] D. J. Berard and S. R. Leslie. "Miniaturized flow cell with pneumatically-actuated vertical nanoconfinement for single-molecule imaging and manipulation". In: *Biomicrofluidics* 12 (2018), p. 054107.

[21] Xavier Capaldi et al. "Probing the organization and dynamics of two DNA chains trapped in a nanofluidic cavity". In: *Soft matter* 14.42 (2018), pp. 8455–8465.

[22] Marjan Shayegan et al. "Probing inhomogeneous diffusion in the microenvironments of phase-separated polymers under confinement". In: *Journal of the American Chemical Society* 141.19 (2019), pp. 7751–7757.

[23] Christian L Vestergaard et al. "Transition state theory demonstrated at the micron scale with out-of-equilibrium transport in a confined environment". In: *Nature communications* 7 (2016), p. 10227.

[24] Hendrik Anthony Kramers. "Brownian motion in a field of force and the diffusion model of chemical reactions". In: *Physica* 7.4 (1940), pp. 284–304.

[25] Fabai Wu et al. "Cell boundary confinement sets the size and position of the E. coli chromosome". In: *Current Biology* 29.13 (2019), pp. 2131–2144.

[26] Pierre-Gilles De Gennes and Pierre-Gilles Gennes. *Scaling concepts in polymer physics*. Cornell university press, 1979.

[27] Yue Qi et al. “Compression of nanoslit confined polymer solutions”. In: *Macromolecules* 51.2 (2018), pp. 617–625.

[28] EC Zeeman. “Stability of dynamical systems”. In: *Nonlinearity* 1.1 (1988), p. 115.

[29] Frédéric Hecht. “New development in FreeFem++”. In: *Journal of numerical mathematics* 20.3-4 (2012), pp. 251–266.

[30] Pang-Ning Tan, Michael Steinbach, and Vipin Kumar. *Introduction to data mining*. Pearson Education India, 2016.

[31] Alexander R. Klotz et al. “Self-avoiding wormlike chain confined in a cylindrical tube: scaling behavior”. In: *Macromolecules* 48 (2015), p. 5028.

[32] Jeff ZY Chen. “Self-avoiding wormlike chain confined in a cylindrical tube: scaling behavior”. In: *Physical review letters* 121.3 (2018), p. 037801.

[33] W Reisner, Jonas N Pedersen, and Robert H Austin. “DNA confinement in nanochannels: physics and biological applications”. In: *Reports on Progress in Physics* 75 (2012), p. 106601.

[34] Guo K Cheong, Xiaolan Li, and Kevin D. Dorfman. “Wall depletion length of a channel-confined polymer”. In: *Physical Review E* 95 (2017), p. 022501.

[35] David R Latulippe and Andrew L Zydney. “Radius of gyration of plasmid DNA isoforms from static light scattering”. In: *Biotechnology and bioengineering* 107.1 (2010), pp. 134–142.

[36] Katie A Rose et al. “Particle tracking of nanoparticles in soft matter”. In: *Journal of Applied Physics* 127.19 (2020), p. 191101.

[37] Pooja Nath et al. “Dynamics of nanoparticles in entangled polymer solutions”. In: *Langmuir* 34 (2018), p. 241.

[38] Kavindya K. Senanayake et al. “Diffusion of nanoparticles within a semidilute polyelectrolyte solution”. In: *Soft Matter* 15 (2019), p. 7616.

[39] Indermeet Kohli and Mukhopadhyay. "Diffusion of nanoparticles in semidilute polymer solutions: effect of different length scales". In: *Macromolecules* 45 (2012), p. 6143.

[40] IY Wong et al. "Anomalous diffusion probes microstructure dynamics of entangled F-actin networks". In: *Physical review letters* 92.17 (2004), p. 178101.

[41] Juin Kim et al. "A polymer in a crowded and confined space: effects of crowder size and poly-dispersity". In: *Soft Matter* 11.10 (2015), pp. 1877–1888.

[42] Ce Zhang et al. "Macromolecular crowding induced elongation and compaction of single DNA molecules confined in a nanochannel". In: *Proceedings of the National Academy of Sciences* 106.39 (2009), pp. 16651–16656.

[43] James Pelletier et al. "Physical manipulation of the Escherichia coli chromosome reveals its soft nature". In: *Trends in Microbiology* 109 (2012), E2649.

[44] Douwe Jan Bonthuis et al. "Conformation and dynamics of DNA confined in slitlike nanofluidic channels". In: *Physical review letters* 101.10 (2008), p. 108303.

[45] Samuel Million-Weaver and Manel Camps. "Mechanisms of plasmid segregation: Have multicopy plasmids been overlooked?" In: *Plasmid* 75 (2014), p. 27.

[46] Guo Kang Cheong, Xiaolan Li, and Kevin D Dorfman. "Evidence for the extended de Gennes regime of a semiflexible polymer in slit confinement". In: *Physical Review E* 97.2 (2018), p. 022502.

[47] Anthony E. Walsby. "Archaea with square cells". In: *Trends in Microbiology* 13 (2005), p. 193.

[48] Suckjoon Jun. "Polymer physics for understanding bacterial chromosomes". In: *Bacterial Chromatin*. Ed. by Remus T. Dame and Charles J. Dorman. Springer, 2010. Chap. 6, p. 97.

[49] J. M Polson and D. A Rehel. “Equilibrium organization, conformation, anddynamics of two polymers under box-likeconfinement”. In: *Soft-Matter* 17 (2021), pp. 5792–5805.

[50] Beth Gibson et al. “The distribution of bacterial doubling times in the wild”. In: *Proceedings of the Royal Society B* 285.1880 (2018), p. 20180789.

[51] Anjana Badrinarayanan, Tung BK Le, and Michael T Laub. “Bacterial chromosome organization and segregation”. In: *Annual review of cell and developmental biology* 31 (2015), p. 171.

[52] Anthony Birnie and Cees Dekker. “Genome-in-a-box: Building a Chromosome from the Bottom up”. In: *ACS nano* 15.1 (2020), pp. 111–124.

[53] Shane C Dillon and Charles J Dorman. “Bacterial nucleoid-associated proteins, nucleoid structure and gene expression”. In: *Nature Reviews Microbiology* 8.3 (2010), pp. 185–195.

[54] Frederic D Schramm, Kristen Schroeder, and Kristina Jonas. “Protein aggregation in bacteria”. In: *FEMS microbiology reviews* 44.1 (2020), pp. 54–72.

[55] Sander K Govers et al. “Protein aggregates encode epigenetic memory of stressful encounters in individual Escherichia coli cells”. In: *PLoS biology* 16.8 (2018), e2003853.

[56] Olivia Goode et al. “Heterologous protein expression favors the formation of protein aggregates in persister and viable but nonculturable bacteria”. In: *ACS Infectious Diseases* 7.6 (2021), pp. 1848–1858.

[57] Ariel B Lindner et al. “Asymmetric segregation of protein aggregates is associated with cellular aging and rejuvenation”. In: *Proceedings of the National Academy of Sciences* 105.8 (2008), pp. 3076–3081.

[58] Urszula Łapińska et al. “Bacterial ageing in the absence of external stressors”. In: *Philosophical Transactions of the Royal Society B* 374.1786 (2019), p. 20180442.

[59] Y. Pu et al. “ATP-Dependent dynamic protein aggregation regulates bacterial dormancy depth critical for antibiotic tolerance”. In: *Molecular Cell* 73 (2019), pp. 143–156.

[60] L. Dewachter et al. “The dynamic transition of persistence towards the VBNC state during stationary phase is driven by protein aggregation”. In: *mBio* 12 (2021), e00703–21.

[61] Anne-Sophie Coquel et al. “Localization of protein aggregation in Escherichia coli is governed by diffusion and nucleoid macromolecular crowding effect”. In: *PLoS computational biology* 9.4 (2013), e1003038.

[62] Abhishekh Gupta et al. “In vivo kinetics of segregation and polar retention of MS2-GFP-RNA complexes in Escherichia coli”. In: *Biophysical journal* 106.9 (2014), pp. 1928–1937.

[63] Etienne Maisonneuve et al. “Existence of abnormal protein aggregates in healthy Escherichia coli cells”. In: *Journal of bacteriology* 190.3 (2008), pp. 887–893.

[64] Jing Tang et al. “Revisiting the conformation and dynamics of DNA in slitlike confinement”. In: *Macromolecules* 43.17 (2010), pp. 7368–7377.

Chapter 5

Multiple Polymer Chains Confined in a Nanoscale Cavity: How Entropic Forces Alter Plasmid Dynamics

In this chapter, we extend the study presented in chapter 4 in two ways:

(1) we explore the effect of adding additional plasmids to the cavity system.

(2) the effect of adding variable pole curvature.

These additions are designed to quantify how incorporating additional plasmids will affect plasmid localization, explore potential plasmid-plasmid interactions and how variable curvature might affect the free energy landscape experienced by diffusing plasmids. We also introduce the state transition method to systematically characterize system dynamics given a specified coarse-graining of the system into well-defined states. Specifically, the state transition method yields a matrix that characterizes the transition probability between the specified coarse-grained states. This approach generalizes the notion of polar 'dwell time' introduced in the previous chapter. We find that, in the presence of T_4-DNA, increasing the plasmid number tends to broaden the observed plasmid distribution in the cavity, with plasmids tending to localize at regions of high curvature. In

the absence of T_4-DNA, we observe that a cavity system with multiple plasmids will exhibit a weak attractive interaction with the cavity boundary (due we argue to a depletion effect induced by the plasmids with respect to each other). Polar dwell-time measurements indicate the presence of repulsive plasmid-plasmid interactions. The state transition method allows us to characterize system dynamics not just for polar occupancy but also for states where both plasmids lie in the cavity center. We observe overall that the state dynamics is determined by the interplay of increased friction with the T_4-DNA packing and excluded-volume interactions with the T_4-DNA.

5.1 Introduction

There is growing appreciation of how cells exploit purely physical interactions to help regulate their metabolism and organize their interiors. In particular, liquid-liquid phase separations are now appreciated as a broad organizing principle by which cells can achieve spatial regulation of biochemical reactions without the need for dedicated membrane bound organelle compartments [1, 2]. Liquid-liquid phase separations exploit intrinsic interactions between macromolecules, often enhanced by the presence of multivalent domains [2], to drive the formation of phase separated biomolecular condensates (droplets). These regions passively concentrate species to enhance reaction kinetics [1, 2] and reduce expression noise by stabilizing reactant concentrations [3]. A large number of membraneless compartments are now believed to form as a result of a liquid-liquid phase separation mechanism, including P granules in *Caenorhabditis elegans* [4], nuclear bodies such as Cajal bodies and nucleoli, and cytoplasmic stress granules [2].

Liquid-liquid phase separations arise from the interactions of many smaller molecular species. Biological organization can also arise from the interactions of a smaller number of large dsDNA molecules. In bacteria, for example, which lack a separate nuclear compartment, large dsDNA molecules including primary/secondary chromosomes [5] and plas-

mid species are free to interact within the confined bacterial volume. These interactions can give rise to self-organizing behaviour through the mechanism of entropic demixing, the tendency of large polymer coils in anisotropic confinement to exclude each other and demix [6, 7, 8, 9, 10]. In particular, entropic polymer demixing has emerged as a potential mechanism to drive the uneven spatial distribution of high-copy-number (hcn) plasmids observed in live-cell imaging of *E. coli* [11, 12].

Low-copy number plasmids (lcn), existing in the cell with less than 10 copies, possess dedicated active machinery to ensure that each daughter cell receives at least one plasmid copy upon cell division (typically based on a *par* system that is somewhat analogous to a mitotic spindle). High-copy-number plasmids which are plasmids that exist in the cell with tens or even hundreds of copies, appear to lack an active partitioning mechanism; examples of high copy number plasmids include the technologically and industrially significant ColE1 derived plasmids that are used for recombinant gene expression [13]. Initially it was thought that hcn plasmids were distributed uniformly in the cell and were partitioned simply via random diffusion; at high copy number this simple mechanism ensures that the probability of a daughter cell receiving no plasmid copies at all is extremely small (smaller than 10^{-6} [14, 15]). However, live-cell imaging of small ColE1 type plasmids (¡10 kbp) in *E. coli* using fluorescence in situ hybridization (FISH) [16] and fluorescence repressor operator systems (FROS) [17] indicated that the plasmid distribution is non-uniform; plasmids appeared to cluster [16] and localize at the cell poles [17]. Further live-cell studies indicated that plasmid clusters at the poles appeared to be excluded from the nucleoid region [18]. A super-resolution microscopy study of fixed cells using FISH refined this picture [19], indicating that in addition to polar clusters plasmids appeared to reside near the cell periphery in an annular region around the nucleoid, with a small degree of nucleoid penetration present. A recent FROS study [11] by T. Hsu *et al.* exploited plasmids expressing spectrally distinct fluorescent repressors to study plasmid clustering and dynamics. The two-color system enabled T. Hsu *et al.* to observe plasmid

co-localization and resolve/track single plasmids labelled with one fluorophore against a higher concentration of background plasmids bearing a spectrally distinct second fluorophore. Plasmids were observed to separate into highly diffusive mobile and localized groups, with the localized plasmids appearing to be part of clusters, and the mobile plasmids appearing to correspond to single plasmids. Plasmid clusters were found only in nucleoid free regions. Single mobile plasmids also exhibited a high degree of nucleoid exclusion, appearing to traverse a narrow confined corridor between the nucleoid and the cell membrane that functions as an entropic barrier (although a small degree of nucleoid penetration was observed, with the degree of penetration appearing to correlate with nucleoid density in a cell-cycle specific fashion). T. Hsu *et al.* developed an impeded plasmid partitioning model taking into account the effect of polar clustering and nucleoid impeded dynamics; this model suggests that the main effect of non-uniform plasmid distribution is to increase the heterogeneity of inherited plasmid copy number, which may lead to beneficial increases in population diversity. C. Planchenault *et al.* [12] investigated the localization of large plasmids (R27, 180 kbp) and large circular DNA excised from chromosomes. With the par system missing they found that R27 tends to localize at the cell poles on the nucleoid edge. They also performed polymer based Monte Carlo simulations indicating that the polar segregation of plasmid DNA depends strongly on DNA size, with only plasmids above around 100 kbp having a strong tendency to be localized at the cell poles.

In vivo imaging studies suggest that hcn plasmid dynamics arises from random diffusion in a non-uniform free energy landscape created by repulsive interactions with the nucleoid arising from entropic demixing [11, 12]. However, the inherent complexity of the *in vivo* system complicates this picture. The prokaryotic intracellular space is densely packed with numerous small biomolecules (e.g. RNAs, proteins and metabolites) and numerous active enzymatic processes are ongoing. These interactions have the effect of obscuring the role of a specific physical interaction, i.e. entropic force, in molecule seg-

regation and partitioning. To address this issue, we isolate purely physical effects by confining DNA molecules in a well defined nanofluidic compartment [20], where the potential interactions and biomolecular players are well known, to create an in vitro model to explore consequences of confinement and entropic demixing. Our previous work [21] confined interacting DNA in a nanofluidic cavity, using a pneumatically deflected silicon nitride membrane lid to seal off the cavity from a surrounding slit (see Fig. 5.1a). This study demonstrated that features mimicking the biological system can be generated by simply confining a single plasmid molecule and a larger dsDNA molecule (T_4-DNA) in an anisotropic cavity. The anisotropic confinement and exclusion interactions with the T_4-DNA give rise to a free-energy landscape with potential valley structures at the poles and cell periphery [21]. The potential valley structure may generate the plasmid pole preference, an important feature of the plasmid distribution.

Our nanofluidic model allows more complicated aspects of the biological system to be added in a step-by-step fashion. One key question is the role of multi-plasmid interactions in the free energy landscape. Due to the great number of hcn plasmids within a bacteria, how does the interaction between multiple plasmids affect their localization? In addition to their non-uniform distribution, plasmid clusters have been observed in an annular ring around the nucleoid periphery and at the cell poles. How do these clusters form; could different mechanisms be implicated in their annular versus polar positioning? Observing multi-plasmid dynamics in our simplified model system may clarify the role of purely physical plasmid interactions arising from dsDNA interactions alone as opposed to more complex biological factors (e.g. presence of localized regions with high RNA polymerase that might lead to aggregation of actively transcribed plasmids in living cells [22]). A second question relates to how curvature in the confining boundary affects the plasmid dynamics. Membrane curvature is now a well-known factor driving localization of biological function in bacteria [23, 24], with proteins identified that are able to sense and aggregate at regions of high positive [25] and negative curvature [26]. This

mechanism is known to drive the accumulation of DivIVA protein at the poles in *B. subtilis* [27]. Curvature-driven polar localization is distinct from polar localization driven by nucleoid occlusion [27]. However, we speculate that membrane curvature and occlusion might have a more complex interplay, with membrane curvature altering the polar free energy pocket in the free-energy landscape experienced by diffusing plasmids.

Here we extend our previous nanofluidic confinement system to explore the effect of multiple plasmids and variable confinement curvature. First, in the presence of a single T_4-DNA crudely simulating a "chromosome", we demonstrate plasmids prefer more sharply defined boundaries (that is boundaries with smaller radii of curvature). This result implies that randomly diffusing hcn plasmids may form clusters near features with sharper edges. Second, in the presence of a T_4-DNA, the spatial distribution of the plasmid becomes broader as the plasmid number increases. In the absence of the T_4-DNA, the plasmid spatial distribution forms a ring-shape structure as the plasmid number increases. Note there is no obvious pole preference for this case. Third, in the absence of the T_4-DNA, the distance between the plasmid distribution edge and the cavity wall decreases as the plasmid number increases. Fourth, in the presence of a T_4-DNA, the dwell time of the two-plasmid system decreases as the extra plasmids are introduced. Fifth, to characterize multiple plasmid dynamics we introduce the state transition matrix method. The state transition matrix can characterize the interaction between multiple plasmids. Depending on the specific state transition, the transition probability increases (or decreases) as we introduce extra plasmids. We argue the change of the transition probability arises from the competition between polymer friction and volume-exclusion. The friction between the T_4-DNA and the plasmid slows down the diffusion process of the plasmid; thus, this effect increases the time plasmids spend at locations where the T_4-DNA concentration is high. On the other hand, the volume-exclusion between the T_4-DNA and the plasmids pushes plasmids from locations with high T_4-DNA concentration to locations with lower concentration. The exclusion decreases the time plasmids

spend at locations where the T_4-DNA concentration is high. The T_4-DNA concentration thus determines the actual plasmid residence time in our picture. To validate the friction volume-exclusion picture, we calculate the diagrams of the state transition probability via Monte-Carlo simulations. The experimental measurements match our simulation qualitatively. Lastly, we use the state transition approach to quantify the plasmid-plasmid interaction and the curvature effect.

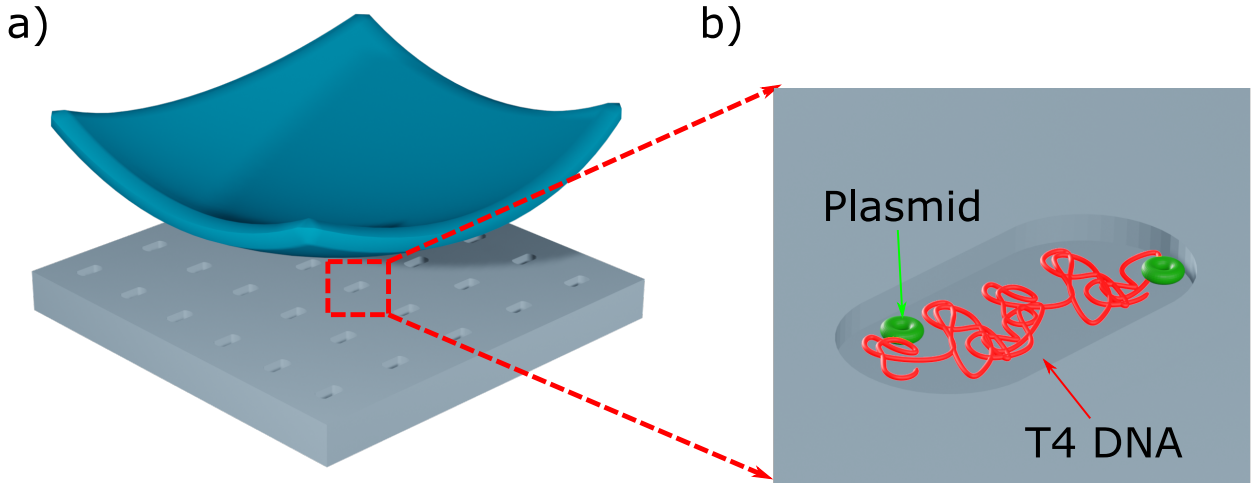

Figure 5.1: a). Schematic of the nanofluidic device with the membrane deflected by pneumatic pressure, closing off the nanocavities that are embedded in the floor of a nanoslit flow cell. b). Zoomed-in view of the trapping scenario. Two plasmids stained with YOYO-1 are trapped within the same cavity as a T_4-DNA stained with YOYO-3. The schematic is not scaled for clarity.

5.2 Materials and Methods

5.2.1 Device Fabrication

The device fabrication protocol is described in detail in [20, 21, 28]. To summarize, we use photolithography followed by reactive ion etching (RIE) to define the fluidic channel (the slit) on a borosilicate glass wafer. Electron beam lithography followed by RIE is then used to create the nanofluidic cavities. We can produce a smooth borofloat etched surface

with a R_a less than 5 nm by the RIE recipe developed by Goyal *et al.* [29]. The cavities are etched to a depth of 168$\pm$4 nm. The borofloat wafer is anodically bonded to a silicon wafer coated with 100 nm of LPCVD silicon nitride. The free standing silicon nitride membrane is released by using KOH etching to remove the silicon backing.

5.2.2 Fluorescent Microscopy

The plasmid vector pBR322 (4361bp, ring topology) is stained with YOYO-1; the T_4-DNA (169kbp, linear topology) is stained with YOYO-3. The loading buffer contains both DNA analytes (plasmid and T_4-DNA) diluted to 2.5 μgmL^{-1} in 10 mM Tris (pH 8.0); 2% (by volume) β-mercaptoethanol (BME) is added to the solution prior to experiments to reduce photobleaching and photonicking.

To interface the nanofluidic chip with the microscope, we design and fabricate a chuck using a stereolithography 3D printer from Formlabs with Formlabs standard clear resin. We perform a 3 min post print IPA rinse and a 15 min UV post-curing at 60 °C to debur the opening edge and harden the resin. The nanofluidic chip is interfaced with the chuck using a homemade PDMS gasket held in place by a metal retaining plate. The chuck with the mounted device including all pneumatic lines is then mounted to the Nikon Eclipse Ti inverted microscope with a Nikon Plan Apo VC 100x oil-immersion objective and a Teledyne Photomatrix Prime 95B camera. We use X-cite Turbo multi-wavelength LED as the excitation source. The light source is triggered by the camera exposure line to minimize photobleaching. We split the YOYO-1 and YOYO-3 channels using Cairn OptoSplit III to filter and project the emission image depending on the spectrum to different portions of the camera. The membrane lid is controlled by a digital pressure controller (Fluigent EZ controller). The DNA sample loading is controlled manually by a syringe. Once the DNA samples are transported underneath the trapping membrane, the inlet and outlet of the fluidic channel are exposed to the atmosphere to equilibrate the lateral flow. The trapping membrane is then actuated with a constant 1500 mbar pressure applied to ensure the

membrane is completely deflected. Videos of molecules trapped in the nanocavities are then captured in real time. After a video is captured, we release the membrane pressure and load fresh DNA samples from the chip sample reservoir, repeating the same process until a sufficient number of videos are captured.

5.2.3 Image analysis

The first step in processing the raw images is to perform the noise removal procedure developed by J Tang et al. [30]. The algorithm is implemented in Python to allow batch processing. The center of mass (CM) of *single* DNA chain is extracted via:

$$\mathbf{r_{CM}}(t) = \frac{\sum \mathbf{r}(t) I(\mathbf{r}, t)}{\sum I(\mathbf{r}, t)} \tag{5.1}$$

We then extract the multi-plasmid CMs using the K-means clustering method [31]. This method allows us to track multiple particles when the plasmids images overlap in one channel. The k-means method assigns pixels to their corresponding plasmid and then calculates each plasmid CM. To briefly summarize the pixel assigning procedure, step 1 initializes the method by assigning pixels to clusters. The initial label can be set either randomly or using prior knowledge of the image. We randomly initialize labels to minimize artificial bias. In step 2 we calculate the CM of each cluster. In step 3 we calculate the distance (Euclidean distance in our case) between each pixel and each of the CMs of each cluster extracted in step 2. We then reassign pixels to the closest cluster. Finally, step 2 and step 3 are iterated until no pixel needs to be reassigned. The k-means method offers a non-parameterized tracking method, which does not rely on the prior knowledge of the images (e.g plasmid size, minimum intensity threshold of a pixel to be considered as valid, inter-frame step length), required by most of the tracking methods. Most importantly, the cluster centers are the centers of fluorescence intensity of the corresponding

plasmids, which are defined consistently with the single plasmid center-of-mass tracking.

We evaluate the accuracy of the K-means clustering method by constructing artificial data from Monte-Carlo dynamics simulations. The data is built by convolving plasmid positions from simulation using the point spread function $\mathrm{PSF}(r) = I_0(\frac{2\mathrm{J}_1(r/r_0)}{r/r_0})^2$, where I_0 is the peak intensity of the Airy disk function, $J_1(x)$ is the Bessel function, r is the distance of a pixel, r_0 is the width of the Airy disk function. For the case of two plasmids tracking, the mean tracking error ($< |\mathbf{r}_{\mathrm{track}} - \mathbf{r}_{\mathrm{sim}}|_2 >$) from the k-means clustering method is $0.05\,\mu m$. For the case of three-plasmids, the mean tracking error is $0.1\,\mu m$. In both cases, the mean tracking error is less than the camera pixel size ($0.11\mu m$) (see supplementary note 1).

5.3 Results

5.3.1 Fluorescent images

The confinement experiments are conducted using a nanofluidic device consisting of an array of cavities embedded in a nanoslit. The waist of the cavities is rectangular and capped by half ellipses (see Fig. 5.1a,b). The eccentricity e of the ellipses ranges from 0 to 0.9. These eccentricities correspond to local radii of curvature at the half ellipse vertex ranging from 0.5 to 1.5. The cavity area is held fixed at $2\,\mu m^2$ by adjusting the length of the rectangular body. The constraint of the fixed area ensures the concentration of the DNA chain is held roughly constant.

The plasmids and T_4-DNA are monitored via wide-field two-color fluorescent microscopy. We differentially stain the plasmids and the T_4-DNA by YOYO-1 and YOYO-3 dye, then we mix these two samples and introduce the DNA samples into the device. By applying pneumatic pressure to the nitride membrane above the cavity array, the membrane is deflected downward so that the cavity is sealed off. This actuation is repeated

until we have multiple plasmids and a T_4-DNA trapped in the same cavity after which a video is recorded. The radius of gyration R_g of the T_4-DNA is estimated around 2 μm [32], which is less than the width/depth of the cavity, so that the conformation of the T_4-DNA is altered by the confinement. Fig. 5.2 shows montages of the plasmids–T_4-DNA trapped within the 1 μm $\times$ 2 μm rectangular cavity and other cavities with different curvature caps (we adjust the width of the rectangular portion to keep the cavity volume the same). The plasmid–T_4-DNA trapping images are shown in Fig. 5.2a and the three plasmids–T_4-DNA trapping images are shown in Fig. 5.2b.

We observe that the plasmids are excluded from the center of the cavity (see Fig. 5.2a,b) for both single-plasmid–T_4-DNA and the three-plasmid–T_4-DNA trapping experiments. The plasmids are excluded from the cavity center due to the influence of the T_4-DNA, which is concentrated at the cavity center [21, 33]. The plasmids can be treated as performing Brownian motion in a free energy landscape that arises from the combination of the plasmid interaction with the cavity walls and volume exclusion interactions with the T_4 DNA [21]. Qualitatively, we are more likely to observe a plasmid in the cavity center region for the three plasmids–T_4-DNA experiment (see the first row of Fig. 5.2b) compared with the single plasmid–T_4-DNA experiment (see the first row of Fig. 5.2a). The increase of the probability for a plasmid to be found in the cavity center can also be observed in cavities with different curvature end caps (see 2^{nd} and the 3^{rd} row of Fig. 5.2a,b).

For cavities with flat ends, we note the plasmids prefer residing at the cavity corners and diffuse mainly within the free energy corridor between the T_4-DNA and the cavity wall (see the first row of Fig. 5.2a and b). This phenomenon is observed in the montage of both single- and multi-plasmid–T_4-DNA experiments.

5.3.2 Plasmid–T_4-DNA histogram

We can quantify our observations by binning the plasmid positions into 2D histograms. The CMs of the plasmids are extracted and the binned histogram is shown in Fig. 5.3.

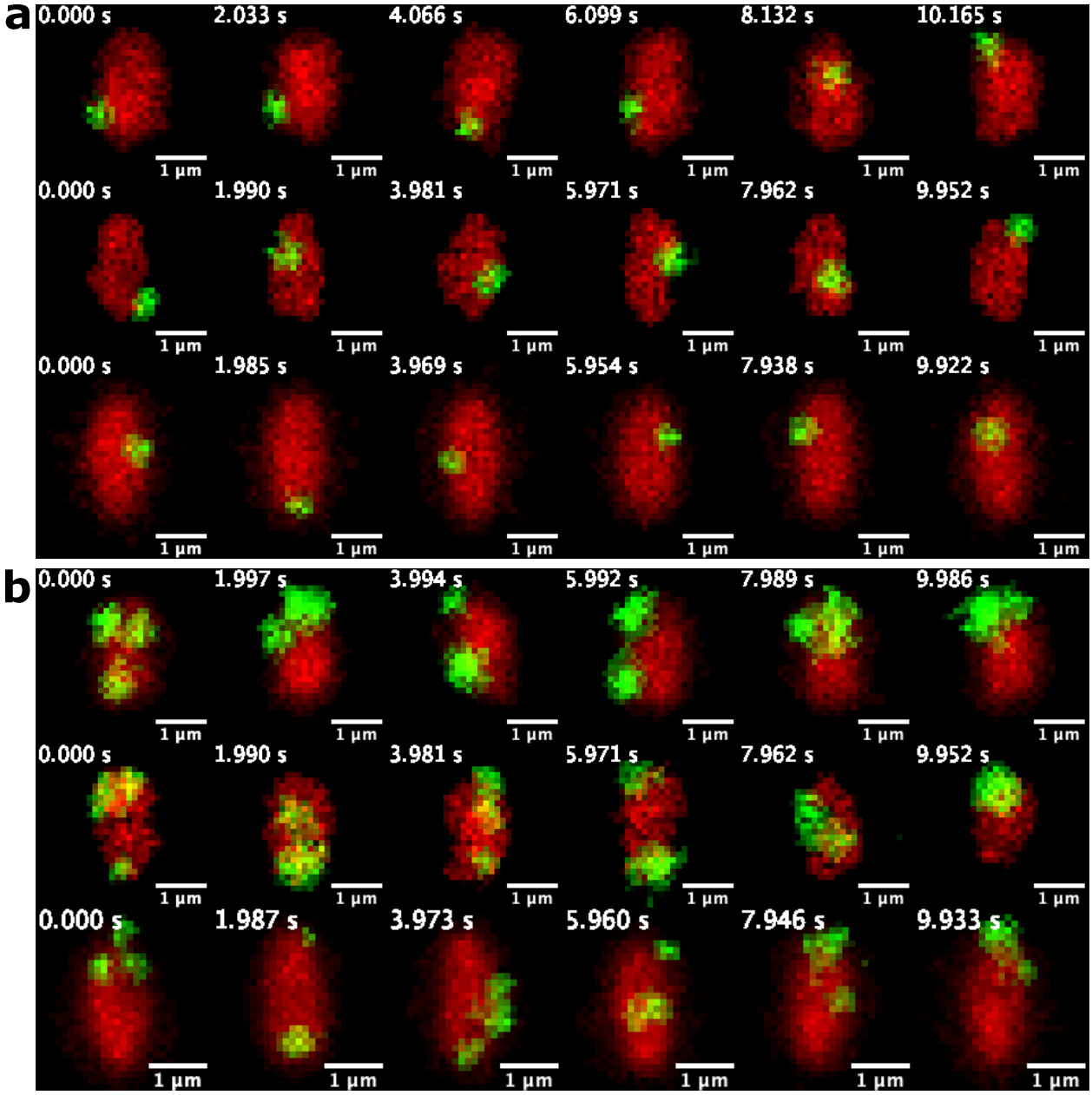

Figure 5.2: Montage of fluorescent images of single- and multi-plasmid–T_4-DNA experiments. a) Images from the single plasmid–T_4-DNA experiment. From the top row to the bottom row correspond to cavities with flat, half-circle and elliptical caps ($e = 0.9$). b) Images from the three plasmid–T_4-DNA experiment. From the top row to the bottom row correspond cavities with flat, half-circle and elliptical caps ($e = 0.9$).

For cavities with flat caps, the corner preference of plasmids is observed for all plasmid numbers explored (i.e. 1, 2, or 3 confined plasmids), matching our montage observation

(see Fig. 5.3a). This is caused by the lower T_4-DNA concentration at the cavity corners compared with the rest of the cavity. The spatial distribution of the plasmids can be estimated using $P(\mathbf{r}) \sim exp(-U(\mathbf{r})/k_BT)$ where $U(\mathbf{r})$ is the free energy function. The free energy is the summation of the volume exclusion term and the wall potential term [21]. The volume exclusion term is proportional to the T_4-DNA concentration $\rho(\mathbf{r})$ from the mean-field theory [34]. The wall potential term is a short-range potential with a decay length close to the radius of the plasmid. We have found the exact details of the wall potential are not significant, altering only the slope of the plasmid distribution edge [21].

We calculate the concentration profile of the T_4-DNA using the mean-field method with ground-state dominance assumption [21, 34]. The concentration is normalized to the number of Kuhn units. The concentration profile of the T_4-DNA is shown in Fig. 5.4 We observe that the T_4-DNA concentration is maximized at the cavity center and has a minimum value at the cavity wall. (see Fig. 5.4) To demonstrate the corner concentration, we plot the T_4-DNA concentration along a cross-section in the vicinity of the wall (50 nm from the wall, see Fig. 5.4 red dashed line). The corners are labelled correspondingly. The T_4-DNA concentration profile can be seen in Fig. 5.4b. We observe that the T_4-DNA concentration is minimized at the cavity corners as expected. We also notice that the T_4-DNA concentration near the longer edge (see Fig. 5.4b path position $1\,\mu$m and $4\,\mu$m) is higher than the concentration at the shorter edge (see Fig. 5.4b path position $2.5\,\mu$m and $5.5\,\mu$m); therefore, the plasmids tend to stay at the shorter edge. This effect is caused by the cavity aspect ratio and leads to the pole preference [21].

Note the corner preference result indicates multi-plasmid clusters in bacteria can form at locations in addition to the pole, given the confined cellular volume has a "sharp" geometry excluding the nucleoid. *In vivo* studies [16, 17] show that the hcn plasmid clusters usually appear at a specific position, i.e. half- and quarter- plane of the cell. Our in vitro study suggests that there may be "sharp" intracellular structures, likely the newly formed pinch shape cell membrane. This picture is supported by the *in vivo* observation that the

hcn plasmid clusters form at the half- and quarter- plane when the cell membrane starts pinching inward, which makes the cluster formation synchronize with the cell phase [16]. In addition, this curvature effect can also assist the successful partitioning of the replicated plasmids.

In the presence of T_4-DNA, the plasmid distribution becomes more uniform as the plasmid number increases. This behaviour can be appreciated by extracting the histogram cross-sections; these give the variation of plasmid probability density across the cavity (see Fig. 5.3b). For single plasmid–T_4-DNA trapping experiments, the cross-section along both the major axis and minor axis shows higher peaks at the cavity periphery than the three plasmids–T_4-DNA experiments, indicating the plasmid distribution becomes more uniform as the plasmid number increases. We attribute this phenomenon to the exclusion between plasmids. The exclusion between plasmids tends to force each plasmid out of the free energy minimum. Note R_g of the plasmid around 100 nm [35], which is considerably smaller than the lateral size of the cavity in both the major and minor directions. This is remarkable since the exclusion between plasmids is much smaller than the exclusion between plasmid and T_4-DNA. Under the background of T_4-DNA, the exclusion between plasmids can still be observed by the histogram.

5.3.3 Multi plasmid distribution in absence of T_4-DNA

In the absence of T_4 DNA we observe that the plasmids show a slight preference for the cavity circumference when multiple plasmids are present in the cavity. The preference appears as a ring shape corridor around the cavity circumference in the plasmid position histogram (see Fig. 5.3c for the cavity with $e = 0.9$ ends). We attribute this effect to depletion interactions, which have the effect of creating a weak attraction between large particles and the boundary [36]. Classically, depletion interactions arise due to the reduction of excluded volume when two larger particles reduce their separation in the presence of smaller inert particles. The same effect can also give rise to the attraction between par-

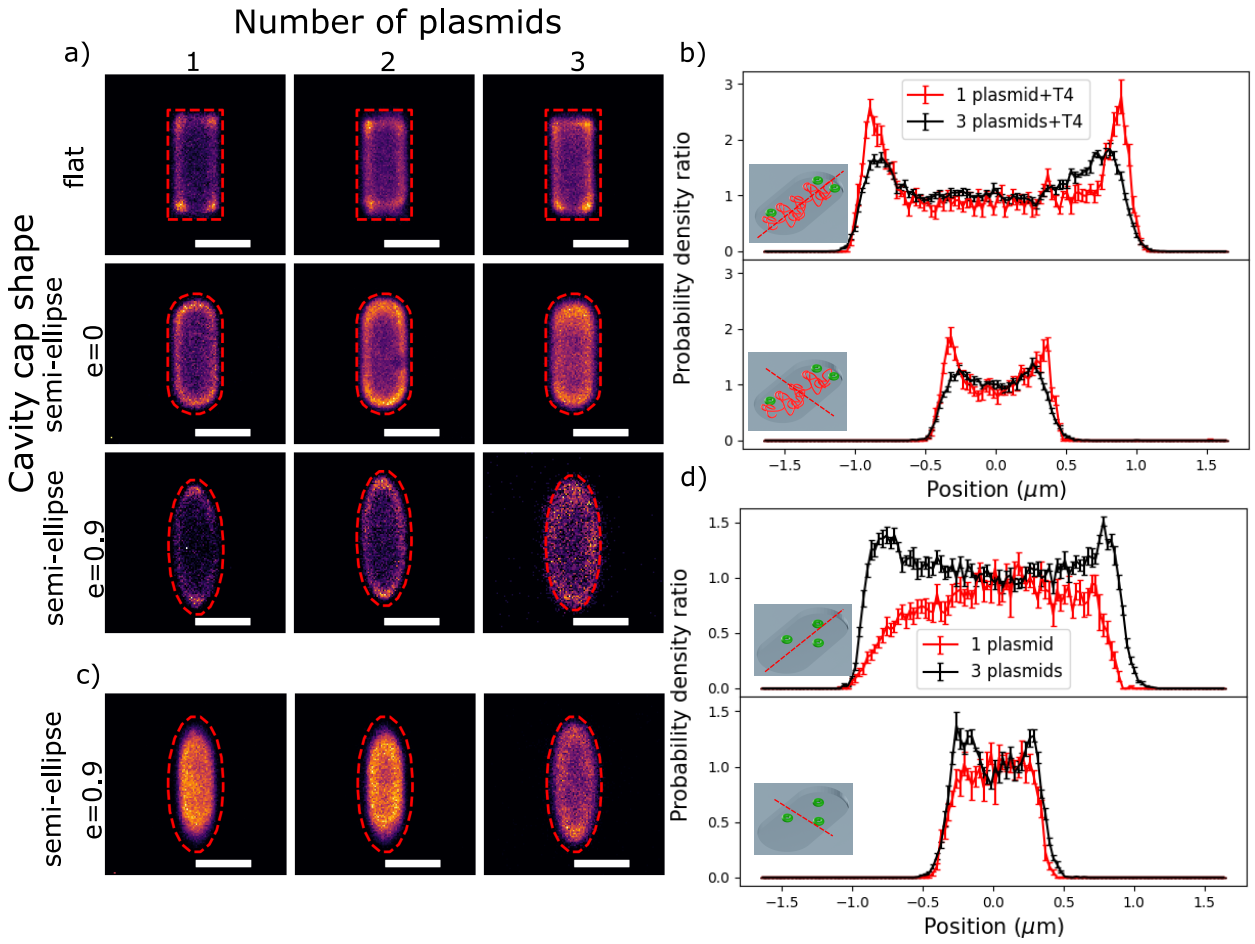

Figure 5.3: Spatial distribution of single- two- and three-plasmid–T_4-DNA experiments with different cavities. a) Histogram of plasmid position in plasmid–T_4-DNA experiment. Scale bars are all $1\ \mu$m. b) The cross-section of the plasmid histogram for plasmid–T_4-DNA experiment in cavity with semi-circle ends. The cross-section is normalized to the probability density at the cavity center; therefore, it measures the contrast of the probability density. c) Histogram of plasmid position in plasmid without T_4-DNA experiment. Scale bars are all $1\ \mu$m. d) The cross-section of the plasmid histogram for plasmid–T_4-DNA experiment in cavity with semi-circle ends.

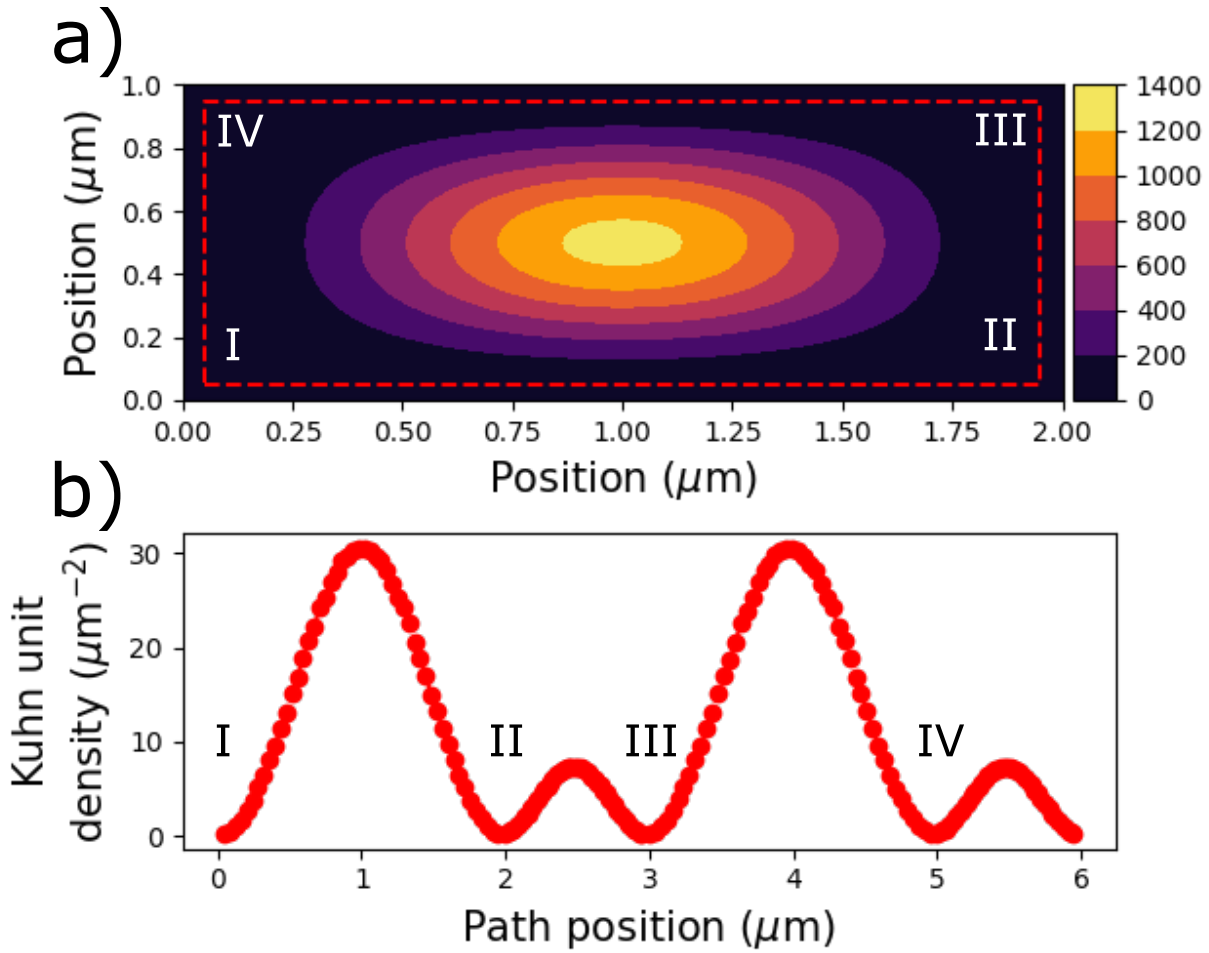

Figure 5.4: Mean-field self-consistent concentration profile of the T_4-DNA solution in a square box. a) The contour plot of the T_4-DNA concentration. The concentration is normalized to the number of Kuhn units on the T_4-DNA. b) The concentration profile along the red dash path in a). I,II,III and IV correspond to the corners with the same label.

ticles and confining surfaces [36]. What is noteworthy about the depletion interactions observed in our system is that they appear to be induced in the presence of only one additional plasmid. Note that, in the absence of attractive depletion interactions, we would expect that the particle distribution to be uniform in the cavity in the absence of T_4 DNA (as is indeed the case for a single confined plasmid).

Additional evidence supporting the role of depletion interactions is obtained from observing how the average plasmid distance from the boundary is altered by varying plas-

mid number. In particular, increasing the number of plasmids in the absence of T_4 DNA reduces the distance between the distribution edge and the wall (see Fig. 5.3d). This finding supports a depletion-based mechanism as we expect the depletion force to increase as additional plasmids are introduced into the system. We can quantify the distance between the plasmid distribution edge and the wall by fitting the cross-section of the plasmid histograms with a general Gaussian function (see inset of Fig. 5.5). We define the position of the distribution edge as the point where the probability density falls off to one half its peak value. The results are shown in Fig. 5.5, demonstrating clearly that for cavities with the same end-cap geometry, the distance between the distribution edge and the wall decreases as the plasmid number increases. This arises from the entropic wall depletion effect where the depletion force is proportional to the number of plasmids.

5.3.4 Polar dwell time for two plasmids in presence of T_4-DNA

One quantity characterizing the multiple plasmid dynamics and their interactions is the two-plasmid polar dwell time: the time duration over which both plasmids stay inside a polar free energy pocket. The dwell measurement starts when we observe two plasmids in the same pole and stops when either plasmid or both plasmids escape the pole. The plasmid is considered to be in the pole region when its position along the major axis x is greater than $0.35\,\mu m$ (The caivty is divided into three regions, i.e. two poles and one waist, with the same length along major axis. $x = 0$ at the cavity center. Approximately a pole region takes $\frac{1}{3}$ of the cavity full length). Histograms of the two plasmids dwell times measured for cavities with variable end-cap geometry are shown in Fig. 5.6; the histograms have a double-exponential form. The longer time-scale corresponds to the mean dwell time of the plasmid at the cavity poles and arises from the increased free energy barrier between the cavity pole region and the cavity waist region. The shorter time scale arises from plasmid trajectories that briefly cross the boundary at $0.35\,\mu$m and then return towards the cavity center without experiencing the potential pocket at the

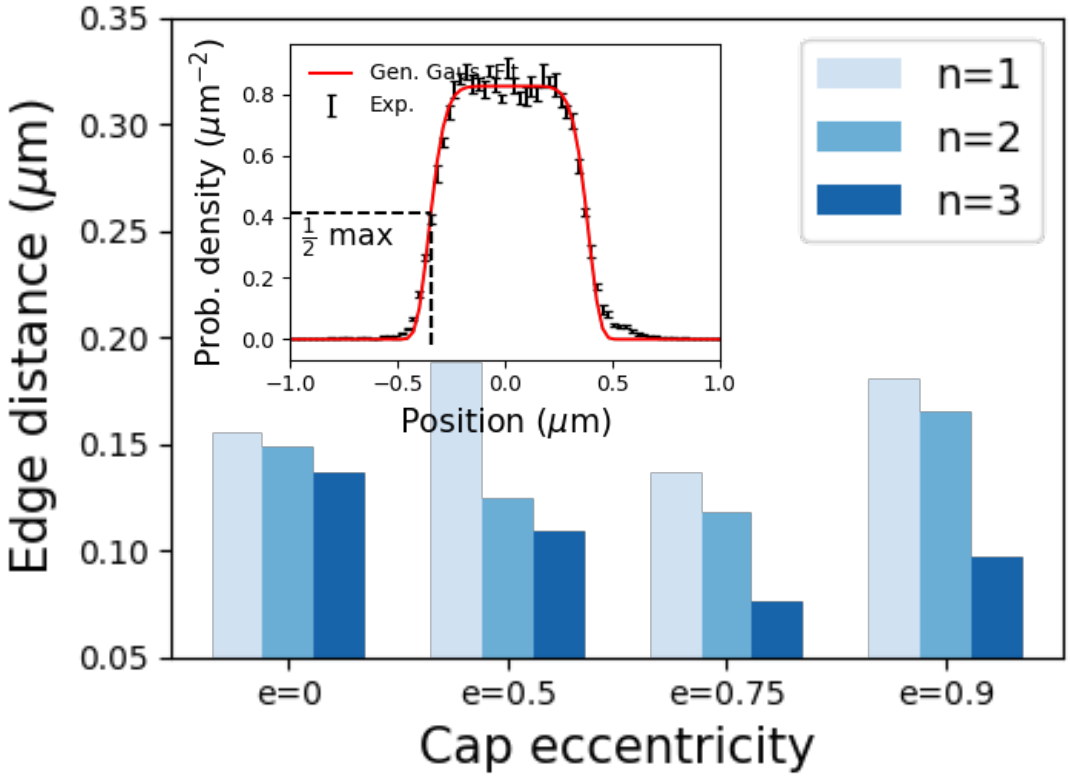

Figure 5.5: The distance between the edge of plasmid distribution and the cavity wall for cavities with variable end-cap geometry and plasmid number. The distance between the cavity wall and the distribution edge decreases as the number of plasmids increases. The inset shows the definition of the plasmid distribution edge. The red solid line is the general Gaussian fitting. The black dashed line shows our definition of the distribution edge.

poles [21]. The dwell time decay constant is defined by the probability dropping to e^{-1} and are shown in Fig. 5.6b).

The observed two-plasmid dwell-times are lower than the reference (non-interaction) dwell times. The reference time is obtained from the single plasmid–T_4-DNA experiment with the same geometry cavity. We extract the dwell time of the single plasmid, and the reference is $\frac{1}{2}$ of the single plasmid case since the escaping events of the two plasmids in the reference are independent. This can be easily seen in Fig. 5.6b, where we show the average two-plasmid dwell-times extracted from exponential fits to the histograms. Note

that the difference between observed and reference two-plasmid dwell times depends on the cavity geometry (see Fig. 5.6b). The observed two-plasmid dwell times are lower than the reference dwell time constants due to the existence of plasmid-plasmid interactions in the form of volume exclusion between the plasmids. Once a plasmid occupies the pole region, these interactions make it more likely than "random chance" for the second plasmid to escape. Note the dwell time difference between the reference and the experiment is shorter than the frame time. This technique thus has the potential to probe subtle changes of the system condition, (e.g. effects arising from ionic strength and crowding).

The two-plasmid dwell time constant also increases as the cap becomes "sharper". We attribute the increase of the dwell time to the deeper free energy well arising from the end-cap curvature and the entropic wall depletion arising from the extra plasmid. These two mechanisms both lead to longer dwell time at poles.

5.3.5 State transition matrix

The state transition matrix formalism provides a more general approach for characterizing system dynamics. In a state transition matrix approach, the system is coarse-grained into well-defined states and individual transition rates are introduced between the different states, populating elements of the transition state matrix M. The system experiences a sequence of transitions from one state to another according to certain probabilistic rules. The possible route of transition can also be shown as a Markov chain, where the future state only depends on the current state.

To adopt the transition matrix approach to our system, we sub-divide the plasmid positions into three possible regions including two poles and one middle region. The regions use the definition of the cavity poles adopted in the previous section. By listing the possible combinations of two plasmids residing in the coarse-grained regions, we classify each frame into one of the six possible states listed in Fig. 5.7a). The sequence of states $\{S^t\}$ are extracted from videos and M is calculated by counting the number of state transitions

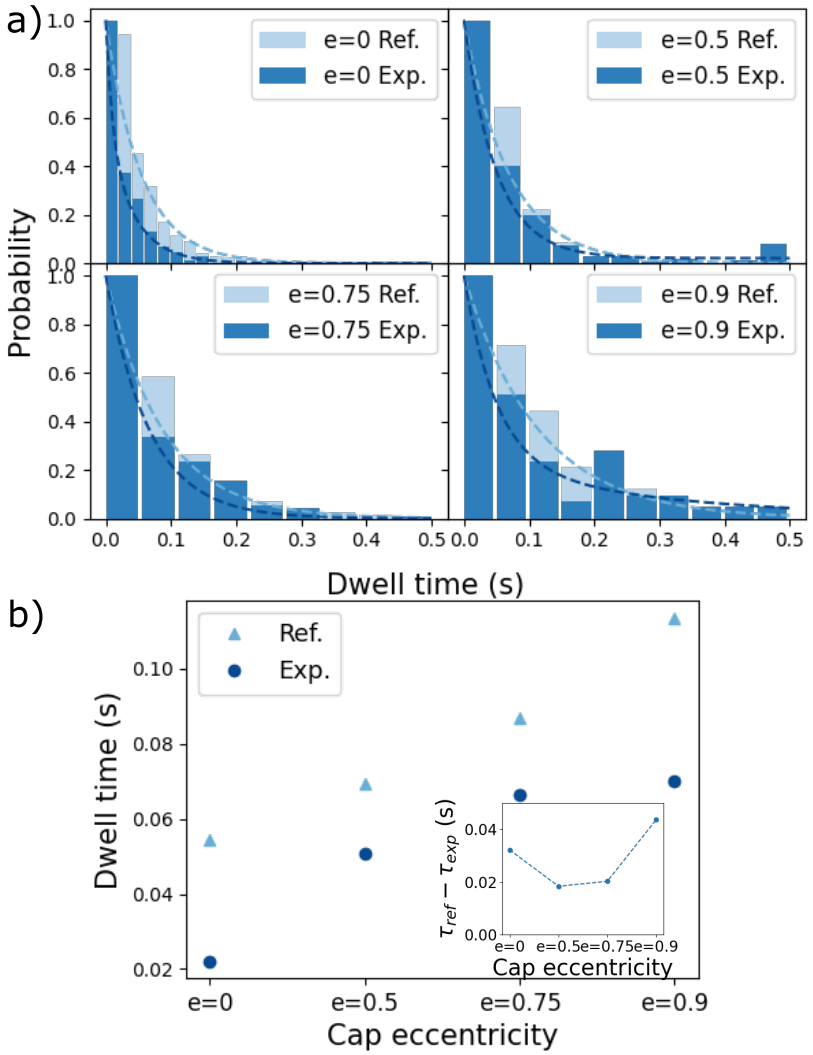

Figure 5.6: The histogram of polar two-plasmid dwell time in presence of T_4-DNA. a) Histograms of the dwell time for escape events from cavities with variable end-cap geometry. The histograms are fitted to a double exponential model (shown as a dashed line). b) Average polar two-plasmid dwell time obtained from double exponential fitting. Triangles (light blue) indicate reference two-plasmid dwell times and circles (dark blue) indicate measured two-plasmid dwell times. The inset gives the difference between the reference two-plasmid dwell time and the experimental two-plasmid dwell time.

between frames. Note the frame time for the videos varies due to the exposure condition, which affects the transition probability. We address this time variation using interpolation between the sequence of states (with the interpolation frame rate set to 50ms). An

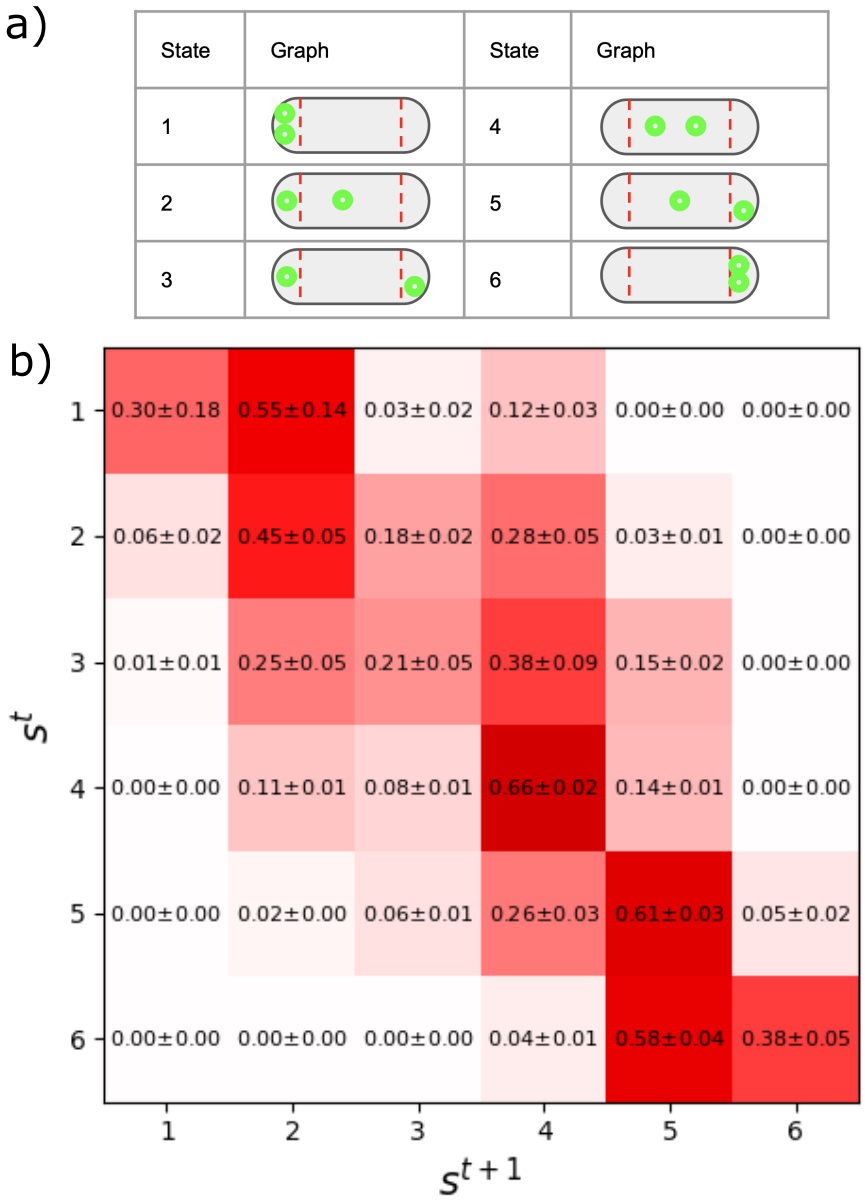

Figure 5.7: Schematic of the system state and a sample state transition matrix. a) Cartoons of the system state. The plasmids are represented by the green marker. b) A sample of the state transition matrix. S^t represents the system state at frame t.

example of a computed state transition matrix M is shown in Fig. 5.7b. Transitions which requires an intermediate state, for example from $S^t = 1$ to $S^{t+1} = 6$, are rarely observed, indicating the camera frame speed ($\sim$ 20 ms to 60 ms) is sufficiently fast to capture the full transition process.

Dynamics in presence of T_4 DNA characterized via state transition matrix

First, we use the state transition matrix formalism to characterize multiple plasmid dynamics in the presence of T_4 DNA. Note that the diagonal terms in M (see Fig. 5.7b) represent the stay probability, i.e. probability per frame that the system stays in the same state for two consecutive frames. The stay probability $\mathbf{M}_{\mathrm{i,i}}$ is related to the dwell time $t_{\mathrm{i,dwell}}$ by $t_{\mathrm{i,dwell}} \propto 1/\mathbf{M}_{\mathrm{i,i}}$. We observe that the presence of the T_4-DNA molecule increases the stay probability for the majority of the states, with state 4 the one exception (here there is no change, see Fig. 5.8). We argue that the observed behaviour of the stay probability in the presence of T_4-DNA of M is caused by two effects: enhanced friction in the presence of T_4 and volume exclusion introduced by the T_4-DNA. The friction between the plasmid and the T_4-DNA slows down the plasmid diffusion (smaller diffusion coefficient D), leading to a higher probability of observing the system in the same state. The volume exclusion favors the plasmid moving to regions of high T_4-DNA concentration; thus, the plasmid has a lower chance to be observed in the T_4-DNA concentrated region (center of cavities) in consecutive frames. The consequence of these two effects is a higher stay probability in the presence of T_4 for all states except state 4, where the effect of enhanced friction and exclusion leads to no overall change in stay probability (Fig. 5.8).

To determine if this proposed physical scenario can explain our observations, we perform Monte-Carlo dynamics simulations [21] to quantify the competition between friction and volume exclusion. Our simulation approach models the plasmids as undergoing Brownian motion in the free energy landscape established by volume exclusion with the T_4 DNA and the confining potential of the cavity walls (neglecting depletion interactions for simplicity). In particular, the free energy landscape for the Brownian walker is given by $F(r) = a\rho(\mathbf{r}) + U_{\mathrm{wall}}$, where we choose the hard-wall potential as U_{wall}. The T_4-DNA concentration $\rho(\mathbf{r})$ is estimated using the mean-field approach [21, 33]. The repulsive term of the Flory energy is $vk_bT\rho$, where v is the excluded volume and ρ is the polymer solution concentration with unit of Kuhn monomers. By running Monte-Carlo

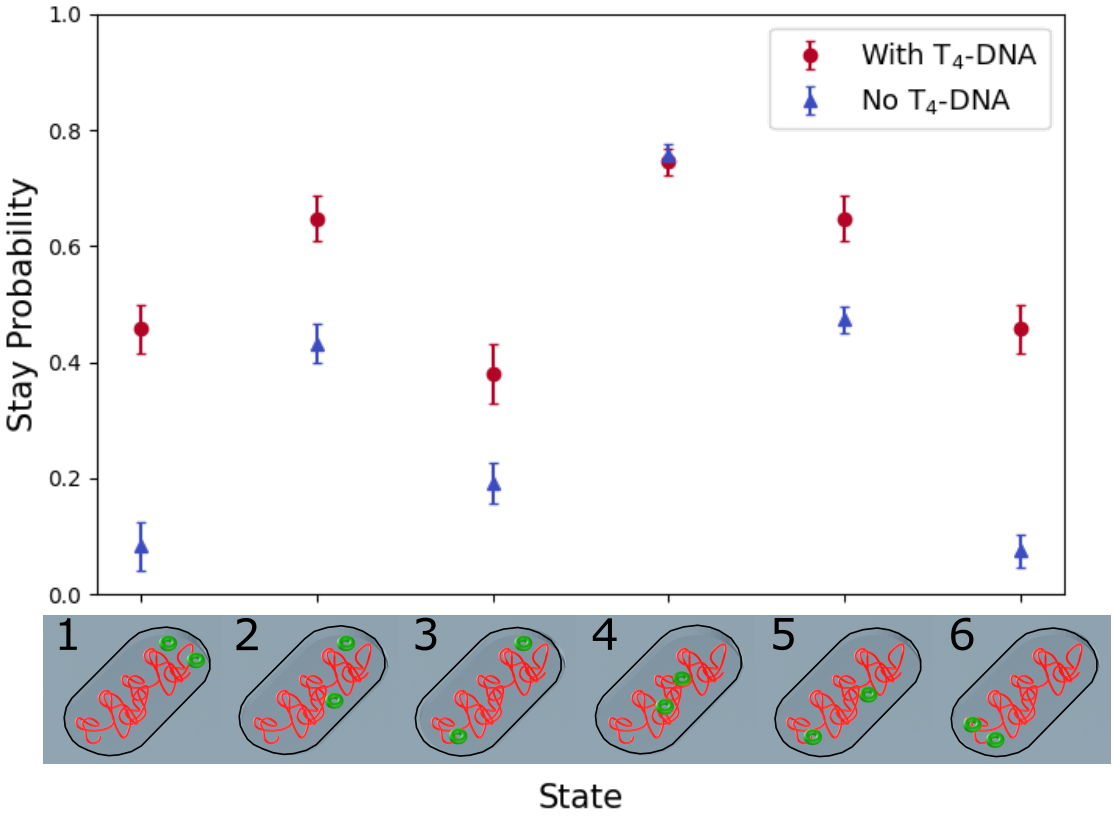

Figure 5.8: The stay probability for the two-plasmid system with and without a T_4-DNA. The illustration of states are shown as x labels. Data points from the two-plasmid–T_4 experiments are shown by the red markers. Data points from the two-plasmid experiments are shown by the blue markers.

dynamics simulation with potential landscape of varying v, we can investigate the effect of the volume exclusion. The friction between the plasmid and the T_4-DNA is explored by varying the diffusion constant (i.e. $D = k_B T/\xi$ with ξ the friction factor) [21]. For each parameter condition, we run 5 times simulation with $n = 3e5$ steps. The dwell time is calculated by averaging all cases captured in 5 simulations. We assume the time difference between two adjacent frames is $20\,ms$ to match our camera. Note that while the diffusion constant and the volume exclusion can be investigated as decoupled in simulation,

they are not strictly independent in free solution according to the Stokes-Einstein relation $D \sim v^{-1/3}$. However, the correlation between the friction and the diffusion constant may become more subtle in the presence of T_4-DNA, which acts like a section of a larger polymer solution to the diffusing plasmid, giving rise to increased friction (so the scaling between D and v may not hold exactly in our experiment [21]). We plot the map of the stay probability. Symmetric states, for example, state 1 and state 6, are merged for simplicity. Our experiment conditions are labelled on the map. For experiments in the presence of T_4-DNA, the radius of the plasmid is estimated as 70 ± 3 nm [21]. The diffusion coefficient is measured as $0.075 \pm 0.0125 \mu$m^2 from the mean-squared displacement calculation [21] and is extracted by fitting the short lag time regime ($< 0.2\,s$) with a linear function ($\mathrm{MSD}(dt) = 4D \cdot dt$). For experiments in the absence of T_4-DNA, the exclusion radius is set to 0 so that the plasmids will not experience the exclusion of T_4-DNA. The diffusion coefficient is extracted from experiments in the absence of T_4-DNA by performing linear fitting. The error bar shows the standard error of the mean for different videos.

We observe that by increasing the diffusion coefficient D, the stay probability decreases. This matches our intuition as we expect the plasmid to escape from a given state more readily if it has a higher diffusion constant. The exclusion radius r is calculated from $v = \frac{4}{3}\pi r^3$. The dependence of the stay probability on the strength of self-exclusion is determined by the number of plasmids present in the cavity center region, where the T_4 DNA concentration is high. For states where no plasmids are present in the center region (states 1, 3 and 6, Fig. 5.8), increasing excluded volume strength increases the stay probability (see Fig. 5.9a,c). This arises because the strong excluded volume in the center region tends to exclude plasmids from this region, increasing the stay probability of states with plasmids present at the poles. When there are two plasmids in the center region (state 4, Fig. 5.8), then the stay probability decreases with increasing excluded volume magnitude (Fig. 5.9d, plasmids are easily ejected from the center region). When only one plasmid is present in the center region, then varying excluded volume strength does not obviously

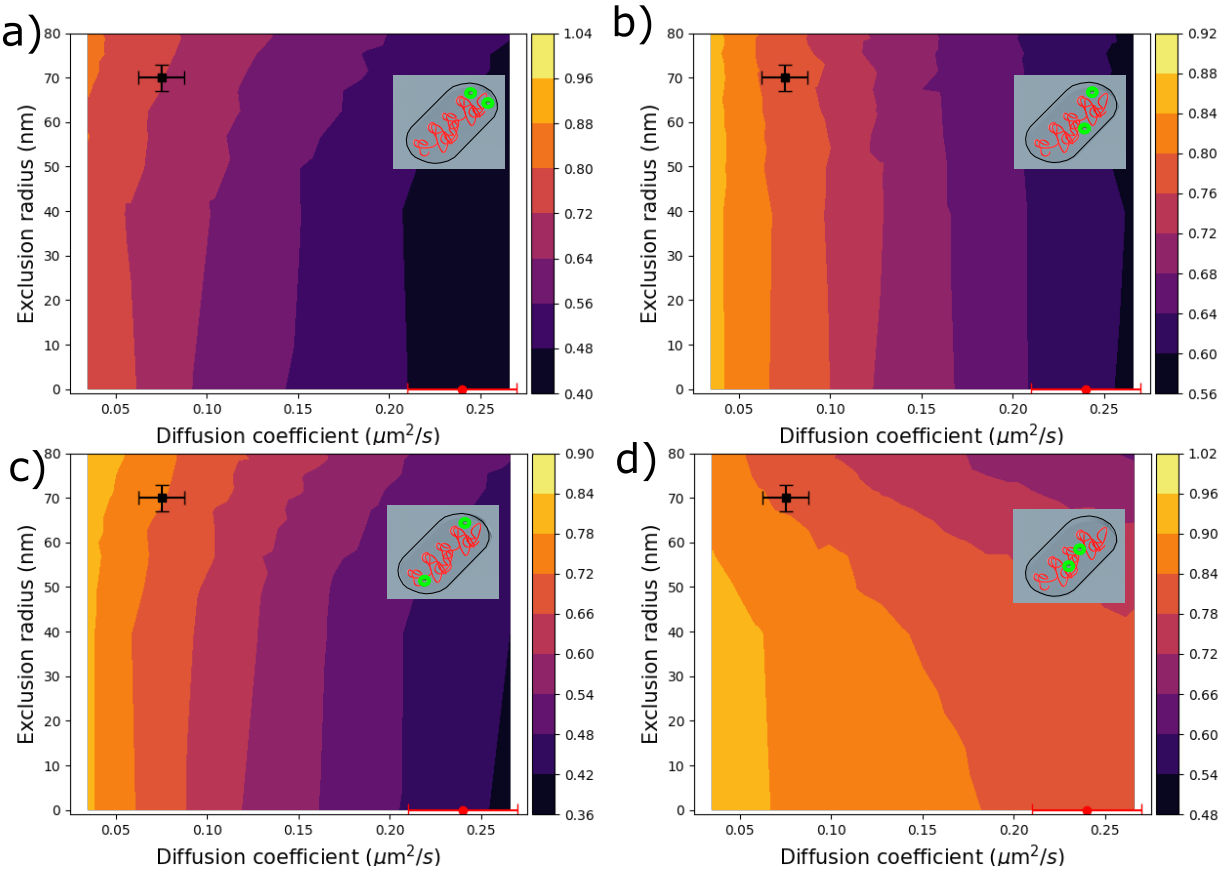

Figure 5.9: The simulated stay-probability map with varying diffusion and excluded volume parameters. The position of the actual experimental systems explored is shown in the map. The system including two plasmids in the presence of T_4 is indicated by the black marker; the system including two plasmids in the absence of T_4 is indicated by the red marker. Stay-probability map a-d show the stay probability corresponding to additional system states. Symmetric states are merged for simplicity.

affect stay probability (see Fig. 5.9b). This result can be understood as resulting from a balance of the tendency of high excluded volume to maintain polar confinement and eject plasmids from the center region. Our simulated stay-probability map qualitatively captures the trend of the stay probability variation and the competition between the effect of exclusion and friction is clarified.

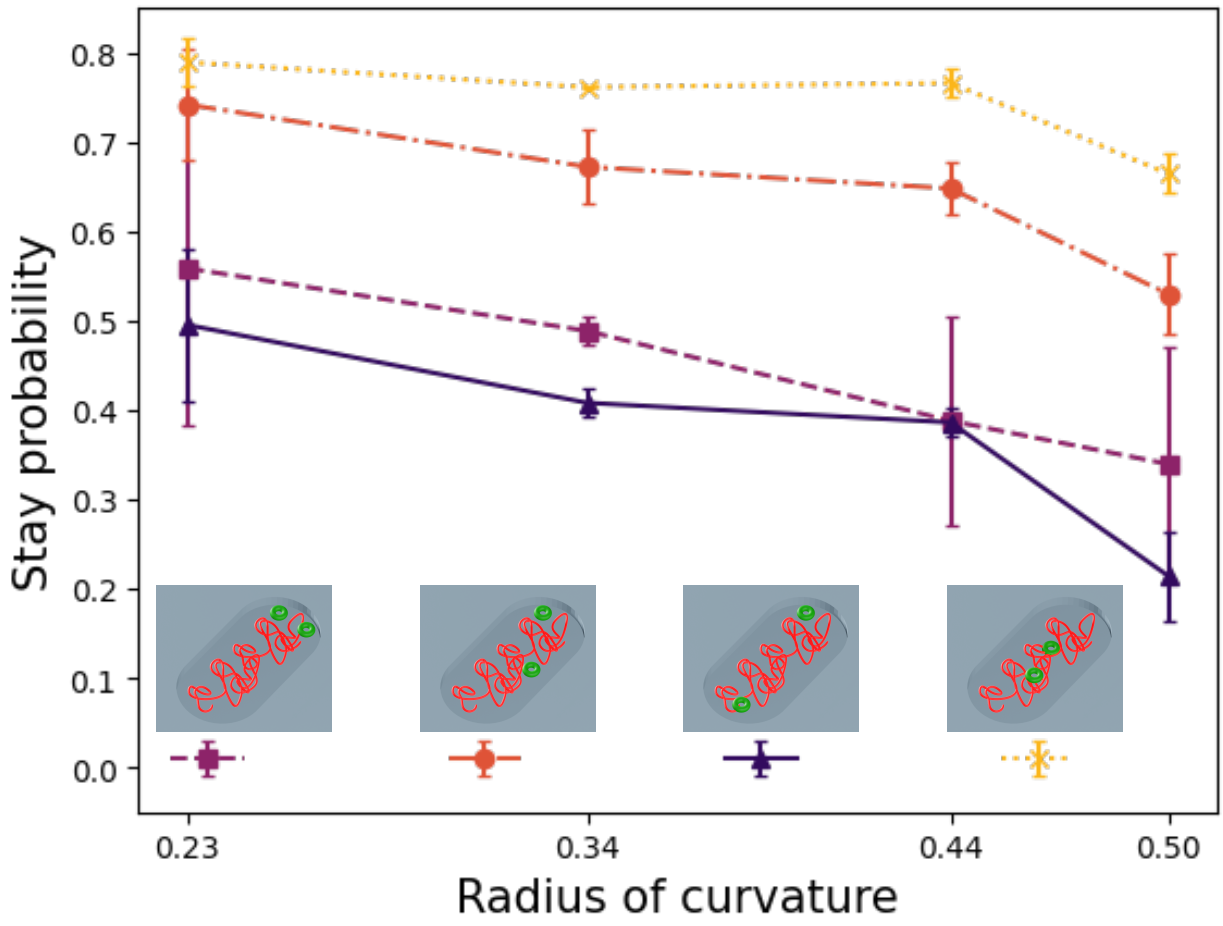

Figure 5.10: The comparison of the state transition probability of the two plasmid–T_4-DNA system for cavities with different cap curvature. The different color marks represent the dwell time of corresponding states. The radius of curvature is the averaged curvature over the boundary of the pole region. The error bar gives the standard error of the mean from the experimental videos.

Use state transition matrix to characterize effect of varying end-cap curvature

We observe the probability of the system staying in the same states increases as the end-cap radius of curvature increases (see Fig. 5.10a). The curved wall applies entropic depletion force to the plasmids, leading to the accumulation of the plasmid at the cavity boundary especially close to the cap [21, 36]. This measures the entropic depletion from the dynamics perspective. However, besides the entropic wall depletion, the concentra-

tion of T_4-DNA also varies due to the cavity curvature, which further complicates the dynamics picture. We think the increase of the stay probability arises primarily from the change of the T_4-DNA conformation. While it is hard to separate the concentration effect and wall curvature effect, these two effects both lead to a deeper free energy well close to the pole, which leads to a longer plasmid dwell time [21].

Reference

[1] Anthony A Hyman, Christoph A Weber, and Frank Jülicher. "Liquid-liquid phase separation in biology". In: *Annu. Rev. Cell Dev. Biol* 30.1 (2014), pp. 39–58.

[2] Salman F Banani et al. "Biomolecular condensates: organizers of cellular biochemistry". In: *Nature reviews Molecular cell biology* 18.5 (2017), pp. 285–298.

[3] Adam Klosin et al. "Phase separation provides a mechanism to reduce noise in cells". In: *Science* 367.6476 (2020), pp. 464–468.

[4] Clifford P Brangwynne et al. "Germline P granules are liquid droplets that localize by controlled dissolution/condensation". In: *Science* 324.5935 (2009), pp. 1729–1732.

[5] Elizabeth S. Egan, Michael A. Fogel, and Matthew K. Waldor. "Divided genomes: negotiating the cell cycle in prokaryotes with multiple chromosomes". In: *Molecular Microbiology* 56.5 (2005), pp. 1129–1138.

[6] Suckjoon Jun and Andrew Wright. "Entropy as the driver of chromosome segregation". In: *Nature Reviews Microbiology* 8.8 (2010), p. 600.

[7] Axel Arnold and Suckjoon Jun. "Time scale of entropic segregation of flexible polymers in confinement: implications for chromosome segregation in filamentous bacteria". In: *Physical Review E* 76.3 (2007), p. 031901.

[8] Youngkyun Jung and Bae-Yeun Ha. "Overlapping two self-avoiding polymers in a closed cylindrical pore: Implications for chromosome segregation in a bacterial cell". In: *Physical Review E* 82.5 (2010), p. 051926.

[9] Youngkyun Jung et al. “Interchain ordering and segregation of polymers under confinement”. In: *Macromolecules* 45 (2012), pp. 3256–3262.

[10] James M Polson and Logan G Montgomery. “Polymer segregation under confinement: Free energy calculations and segregation dynamics simulations”. In: *The Journal of chemical physics* 141.16 (2014), p. 164902.

[11] Tai-Ming Hsu and Yi-Ren Chang. “High-Copy-Number plasmid segregation—single-molecule dynamics in single cells”. In: *Biophysical journal* 116.5 (2019), pp. 772–780.

[12] Charlène Planchenault et al. “Intracellular positioning systems limit the entropic eviction of secondary replicons toward the nucleoid edges in bacterial cells”. In: *Journal of molecular biology* 432.3 (2020), pp. 745–761.

[13] Samuel Million-Weaver and Manel Camps. “Mechanisms of plasmid segregation: Have multicopy plasmids been overlooked?” In: *Plasmid* 75 (2014), p. 27.

[14] Kurt Nordström and Stuart J Austin. “Mechanisms that contribute to the stable segregation of plasmids”. In: *Annual review of genetics* 23.1 (1989), pp. 37–69.

[15] Kurt Nordström and Kenn Gerdes. “Clustering versus random segregation of plasmids lacking a partitioning function: a plasmid paradox?” In: *Plasmid* 50.2 (2003), pp. 95–101.

[16] Joe Pogliano et al. “Multicopy plasmids are clustered and localized in Escherichia coli”. In: *Proceedings of the National Academy of Sciences* 98.8 (2001), pp. 4486–4491.

[17] Shiyin Yao, Donald R Helinski, and Aresa Toukdarian. “Localization of the naturally occurring plasmid ColE1 at the cell pole”. In: *Journal of bacteriology* 189.5 (2007), pp. 1946–1953.

[18] Rodrigo Reyes-Lamothe et al. “High-copy bacterial plasmids diffuse in the nucleoid-free space, replicate stochastically and are randomly positioned at cell division”. In: *Nucleic Acids Research* 42.2 (2014), pp. 1042–1051.

[19] Yong Wang, Paul Penkul, and Joshua N Milstein. "Quantitative localization microscopy reveals a novel organization of a high-copy number plasmid". In: *Biophysical journal* 111.3 (2016), pp. 467–479.

[20] Xavier Capaldi et al. "Probing the organization and dynamics of two DNA chains trapped in a nanofluidic cavity". In: *Soft matter* 14.42 (2018), pp. 8455–8465.

[21] Zezhou Liu et al. "Confinement anisotropy drives polar organization of two DNA molecules interacting in a nanoscale cavity". In: *Nature communications* 13.1 (2022), pp. 1–12.

[22] Marıa-Antonia Sánchez-Romero et al. "Location and dynamics of an active promoter in Escherichia coli K-12". In: *Biochemical Journal* 441.1 (2012), pp. 481–485.

[23] Bruno Antonny. "Mechanisms of membrane curvature sensing". In: *Annual review of biochemistry* 80 (2011), pp. 101–123.

[24] Kerwyn Casey Huang and Kumaran S Ramamurthi. "Macromolecules that prefer their membranes curvy". In: *Molecular microbiology* 76.4 (2010), pp. 822–832.

[25] Kumaran S Ramamurthi et al. "Geometric cue for protein localization in a bacterium". In: *Science* 323.5919 (2009), pp. 1354–1357.

[26] Tristan S Ursell et al. "Rod-like bacterial shape is maintained by feedback between cell curvature and cytoskeletal localization". In: *Proceedings of the National Academy of Sciences* 111.11 (2014), E1025–E1034.

[27] Géraldine Laloux and Christine Jacobs-Wagner. "How do bacteria localize proteins to the cell pole?" In: *Journal of cell science* 127.1 (2014), pp. 11–19.

[28] Imman I Hosseini et al. "Nanofluidics for simultaneous size and charge profiling of extracellular vesicles". In: *Nano Letters* 21.12 (2021), pp. 4895–4902.

[29] Abhijat Goyal, Vincent Hood, and Srinivas Tadigadapa. "High speed anisotropic etching of Pyrex® for microsystems applications". In: *Journal of non-crystalline solids* 352.6-7 (2006), pp. 657–663.

[30] Jing Tang et al. "Revisiting the conformation and dynamics of DNA in slitlike confinement". In: *Macromolecules* 43.17 (2010), pp. 7368–7377.

[31] Tapas Kanungo et al. "An efficient k-means clustering algorithm: Analysis and implementation". In: *IEEE transactions on pattern analysis and machine intelligence* 24.7 (2002), pp. 881–892.

[32] Po-Keng Lin et al. "Static conformation and dynamics of single DNA molecules confined in nanoslits". In: *Physical Review E* 76.1 (2007), p. 011806.

[33] Pierre-Gilles De Gennes and Pierre-Gilles Gennes. *Scaling concepts in polymer physics*. Cornell university press, 1979.

[34] Michael Rubinstein, Ralph H Colby, et al. *Polymer physics*. Vol. 23. Oxford university press New York, 2003.

[35] David R Latulippe and Andrew L Zydney. "Radius of gyration of plasmid DNA isoforms from static light scattering". In: *Biotechnology and bioengineering* 107.1 (2010), pp. 134–142.

[36] AD Dinsmore et al. "Hard spheres in vesicles: curvature-induced forces and particle-induced curvature". In: *Physical Review Letters* 80.2 (1998), p. 409.

Chapter 6

Discussion and conclusion

6.1 Discussion and conclusion

Our first work illustrates that physical principles may play a role in more complex phenomena in bacteria. The two-λ-DNA experiment shows how entropy-driven chain demixing can segregate two equal-size molecules in anisotropic confinement, which has been proposed as a possible mechanism promoting chromosomal segregation in bacteria. The single-plasmid–T_4-DNA experiment illustrates a principle that may help explain the observed distribution of high-copy number (where hcn plasmids usually have more than 10 copies per cell) plasmids.

From a purely physical perspective, the shape-dependent organization of two confined λ-DNA molecules arises from the enhanced repulsion under strong confinement. When polymer chains are confined in a 2D slit-like geometry, the repulsion between chains is greatly enhanced due to the concentration of the chain increasing. The free energy cost of a chain overlapping has been probed via molecular dynamics and Monte-Carlo simulation. The free energy crosses over from $F \sim n^{dv/(dv-1)}$ to $\sim n^{d/(d-2)}$, where $v = 3/(d+2)$ is the Flory exponent [19], as the confinement transits from bulk to slit. However, to our knowledge model experimental system which contains a precisely cali-

brated degree of complexity, still waits to be conducted. While a simulation methodology might produce a qualitative description, a model experimental system is critical for calibrating the simulation and providing simulations with quantitatively correct results. For example, the qualitative conclusions regarding the entropic segregation, the chain conformation and the free energy scaling can be drawn from simulations. However, to ensure that quantitative aspects are also right, for example, the detailed segregation dynamics (pole-swapping) and the free energy scaling exponent, experiments are greatly needed.

Our second work shows our nanocavity system and transition matrix approach have the potential to characterize molecular interaction in a precisely defined environment, which may shed light on complex molecular dynamics in cells. Our approach allows us to increase the system complexity in a step-by-step fashion, for example adding molecules one by one to observe how the addition of each system component alters the dynamics. The transition matrix approach enables us to extract the transition rates between different dynamic states defined by spatial location and occupancy number. By comparing the transition rates for systems of increasing complexity, we can then determine the relative contribution of different interactions to the overall dynamics. Here we demonstrated this possibility by exploring the effect of increasing plasmid number, but we could look at other macromolecules, for example, the interaction between the localized aggregates of unfolded/mis-folded proteins [84, 85]. In principle, it is possible to isolate the protein aggregates from E. coli via centrifugation and label them differentially. By monitoring the dwell time for each molecule and then constructing the reference dwell time, we can compare the reference to the measured dwell time to indicate the polarity of the interaction. The transition matrix approach can also be refined further by applying much finer coarse-gaining. This might lead to the possibility of characterizing the interaction potential with some degree of spatial detail.

To expand the point of protein aggregates, one may ask "how does the protein aggregate accumulated at the cell pole affect the plasmid localization? Is it possible that

the protein aggregates cause the plasmid localization?" Note the misfolded protein accumulation phenomena usually appear in special circumstances, such as high temperature, exposure to antibiotics and starvation. The environmental pressure causes bacteria to enter the persister state, which is a dormant state that allows the bacteria to survive and potentially resume growth when conditions improve. While protein aggregates only appear under certain circumstances, localization of plasmids arise under normal growth condition, which is distinct from the strained environment. However, interesting interactions between the protein aggregates and the plasmids may occur in the persister state. For example, both protein aggregates and the plasmids may be excluded by the nucleoid, then they interact inside the cell pole. Adding protein aggregates to our system and observing if there is polar organization and plasmid displacement to the alternate pole is a potential experiment. This proposed experiment can test the hypothesis that biological phenomena may arise from physical interactions mediated in a confined environment.

There are questions commonly asked about both presented works. In particular, questions are related to how to properly interpret our "bottom-up" in vitro experiment result and provide implications on in vivo biological systems. For example: 1. How do proteins affect the segregation result? 2. How to interpret the timescale measured in our system? 3. How will the molecular crowding affect our result? 4. Is it possible to build up an artificial cell with our technology by increasing the complexity gradually?

Proteins explicitly and implicitly affect chromosome segregation and plasmid partitioning by changing the physical properties of DNA and cell morphology. Sophisticated partitioning machinery is encoded in bacterial chromosomes and low-copy number plasmids, which produces sequence-specific DNA binding protein (for example RacA in B.subtilis and PopZ in Caulobacter) that directly assists the partitioning by consuming energy. In addition, there are various proteins, for example, small acid-soluble DNA-binding proteins (SASPα and SASPβ) for plasmids and nucleoid-associated proteins such as MukBEF, HU and HNS for chromosomes, that change the DNA property directly by

changing DNA supercoiling structures. From our perspective, the *correlation length* (blob size) increases from the compaction caused by DNA supercoiling, which ensures successful chromosome segregation and promotes the volume exclusion between nucleoid and plasmids. In fact, studies [86, 87, 88] have shown the degree of chromosome segregation disruption of muk$^-$ E.coli can be controlled by the level of supercoiling. Proteins for both cases are NOT designated to ensure chromosome segregation and partitioning. However, they promote segregation by changing the DNA structures.

One of the pressing issues making the entropic chromosome segregation mechanism controversial among biologists is the time scale of the spontaneous mixing/demixing process. Do two initially intermingled polymers spontaneously segregate on a reasonable time scale when confined in a cell-like structure? Our device can confine a DNA chain that is originally in the mixed state, i.e. two DNAs are stained differentially and merged into one chain. Given the fact that the membrane can be controlled in $\sim$5 nm precision [83], we can raise the membrane by a few nanometers and introduce a DNA cutter specifically targetting the merge point. By observing the demixing process in real-time, it is possible to measure the time scale of the spontaneous demixing process. In our current experiment, we did not observe mixing configuration for two-λ-DNA experiment, which indicates the demixing time is much shorter than the frame time in our confinement geometry.

Another factor that may affect chromosome segregation and plasmid partitioning is molecular crowding in bacteria. The bacteria are filled with small macromolecules like proteins and RNAs. Those small macromolecules do not actively modulate the mixing/demixing process. However, the conformation of the DNA chain may change accordingly which in turn alters the mixing/demixing. From our first work, we observe the T_4-DNA are compacted with high crowder concentration. The compacted chains become denser and it becomes less likely for chains to penetrate each other, therefore the demixing configuration is enhanced. However, from another perspective, macromolecule crow-

ders apply an effective osmotic pressure, which compacts chains together that promotes mixing. The actual result caused by crowders is actually a balance between these two pictures. An interesting experiment would be to introduce dextran into a two-λ-DNA system and observe the degree to which they are forced to overlap.

Entropic chain segregation and partitioning are passive processes. Such passive nature certainly has implications on primal life [65]. Szostak et al. [89] have proposed a self-replicating vesicle which replicates as a protocell. The lipid vesicles are spherical and allow the contained DNA and RNA to replicate. Remarkably, the vesicles can divide autonomously and the daughter population shares a similar size distribution as the parental generation. Our first work suggests if the polymer exclusion is strong enough to break the spherical symmetry of the vesicle, it may lead to vesicle fission. Compared with the lipid vesicle, our cavity system does have a pre-defined volume and geometry. While replication of the artificial cell may not be feasible for our cavities, we can study the geometry distribution of the replicated vesicles under confinement with various conditions. We potentially can draw a phase diagram similar to the one proposed by S. Jun et al. [12]. This may answer how the morphology of primal cells evolves under confinement.

In our second work, we developed a nanofluidic model system to explore the interactions of multiple plasmid molecules in anisotropic cavities. We introduced a larger DNA molecule (based on T_4-DNA) that occupies the cavity center and modeled the effect of a bacterial chromosome. In the presence of T_4-DNA, we observed that by increasing the plasmid number, the spatial distribution of the plasmids becomes more uniform. We attributed this to excluded volume interactions between the plasmids that drive the plasmids out of the circumferential free energy well they occupy along the cavity periphery. In addition, in the absence of T4, we noticed that when there is more than one plasmid present the plasmids tend to accumulate along the cavity periphery. We attributed this phenomenon to depletion interaction induced by the additional plasmids with respect to each other [76]. The state transition matrix provides a more general approach to charac-

terize system dynamics. In the state transition matrix approach, we coarse grained the system dynamics into distinct states defined by polar versus central cavity positioning and plasmid number. The stay probability measures how likely the system will remain in a given state for a short duration, i.e. one video frame of time. We observed generally that the stay probabilities are higher in the presence of T_4-DNA, with the exception of the state where both plasmids are centrally positioned. We attributed this finding to the combined effects of enhanced friction in the presence of the background T_4-DNA and excluded volume interactions between the plasmids and the T_4-DNA, which we showed can be clarified via the Monte-Carlo simulation.

6.2 Future work

Our nanofluidic model allows a vast collection of additional experiments by adding simple possible ingredient one by one. Our addition of dextran particles into two-chain confinement system is an example of how such ingredient-wise investigation is performed. We could add proteins and ATP to study the active DNA manipulation process, for example, adding SMC proteins to study the DNA loop extrusion. We could add DNA and structural protein step-by-step to study how the local interactions of DNA, proteins, confinement and other possible ingredients lead to macroscale-emergent features of a real chromosome.

Our device also has the potential to incorporate other nanoconfinement technologies. For example, we can introduce a solid-state nanopore in the membrane. It is unlikely to overestimate the interest in such devices. Our device could be used to individually introduce multiple stained DNA chains via the pore to increase the DNA concentration in the cavity. This could be used to probe experimentally the critical concentration that DNA chains transit from dilute to semi-dilute (partially mixing) to concentrated solution (correlation length is on the order of monomer size) in vitro. This experiment is of great

interest both for polymer physics to draw the phase diagram and for biology to fully understand the packing process of DNA chains in bacteriophage capsids. This process also can be studied in a reverse manner to investigate the threading of the DNA chain. Will DNA chains thread through the nanopore spontaneously? If so, the potential barrier can be measured by applying a minimum voltage across the pore to stop the threading. From a biology point of view, we can perform single-cell lysing, single molecule extraction and purification via this structure. A cell can be trapped and lysed within the cavity. The target molecule can be stained and extracted through the pore, while the unwanted debris can be filtered in the cavity. Trans-pore ionic current can be measured during the extraction process to identify if the threading molecule is the target one.

In addition, the thin silicon nitride membrane offers the possibility of integrating nanocavities with other technologies such as nanopores. In theory, it is possible to introduce a portion of a molecule from the other side of the membrane into the cavity via the pore. The small portion of the molecule would interact with the "probe" molecule which is confined in the cavity. By analyzing the conformation change of the "probe" molecule, information about the molecule of interest can be extracted. Our future work will focus on making pores on the membrane and incorporate optical measurement with electrical measurement.

Chapter 7

Appendices

We provide the supplementary materials for the two manuscripts here for reference.

7.1 Supplementary Information for "Confinement Anisotropy Drives Polar Organization of Two DNA molecules Interacting in a Nanoscale Cavity"

Supplementary Note 1

In this section we present details for how the dwell time in a given polar-proximal state was extracted for the system containing two λ-DNA molecules. While we can fit directly to the histogramed dwell time data shown in Fig. 3**c** in the manuscript, we believe it is preferable to fit to the corresponding cumulative dwell time histogram. The reason is that results obtained from fitting to the histograms may be biased by the particular bin size selected to create the histogram, while the cumulative histogram does not require a particular bin size to be determined. Supplemental Fig. 7.1 shows results of fitting the cumulative of a single exponential to the cumulative dwell time histogram for all cavities

investigated (using a least-squares method). The mismatch between the fitted model and cumulative data at high dwell times arises from the low statistics at very long dwell times.

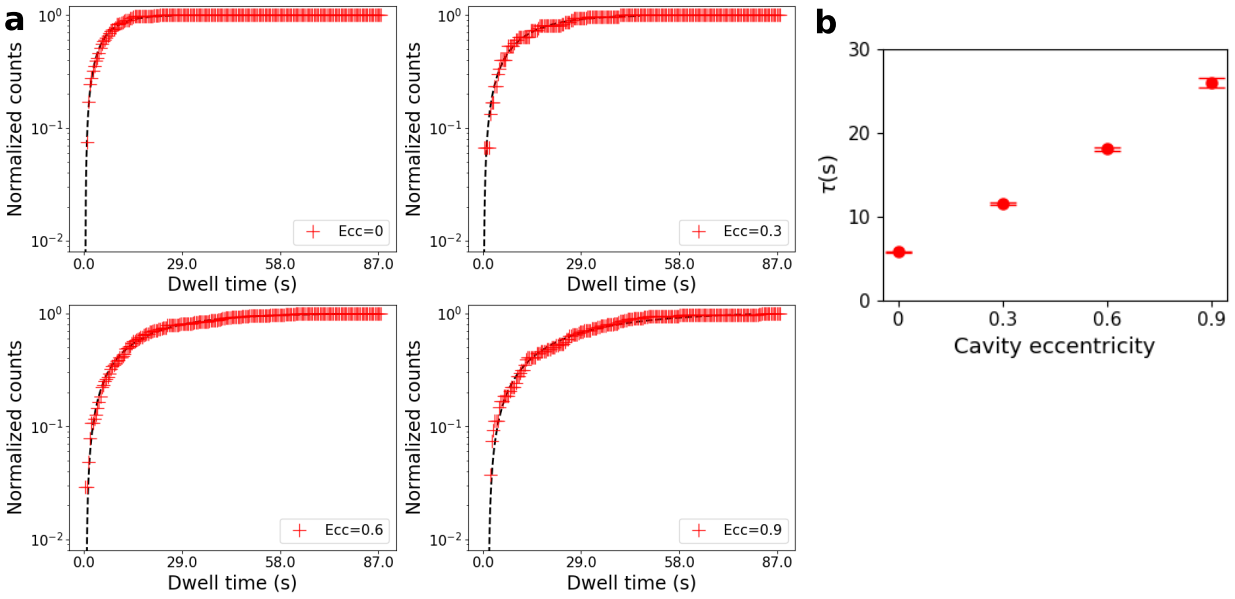

Figure 7.1: Cumulative dwell time fitting for the two DNA confinement. **a**. Results of cumulative fitting for evaluation of the dwell time τ of the two-chain system in a given polar-proximal state. The blue points give the cumulative dwell time histogram; the dashed red line the exponential fit. Note that the cumulative histograms have been normalized by the total number of counts. **b**. Obtained dwell time versus cavity eccentricity. The error bars denote the fitting covariance.

Supplementary Note 2

We use an open-source finite element PDE solver, FreeFEM, to solve the numerical model for the T_4-DNA concentration in an elliptical cavity. The PDE to be solved is:

$$E\Psi = -\xi^2 \Delta\Psi + \Psi^3, \tag{7.1}$$

where E is an eigenvalue related to the total system free energy, Ψ is the T_4-DNA concentration profile and ξ is the correlation length. The value of ξ does not change the concentration profile of the ground state solution visibly when ξ is on the order of $1\,\mu$m. ξ of a T_4-DNA is measured to be $3.96\,\mu$m[62]. Dirichilet boundary conditions ($\Psi = 0$) are applied the ellipse edges. We address the non-linear Ψ^3 term by a classical iteration method. The PDE is linearized via:

$$E\Psi_{k+1} = -\xi^2 \Delta\Psi_{k+1} + \Psi_{k-1,k}^2 \Psi_{k+1}, \tag{7.2}$$

where $\Psi_{k-1,k} = \frac{1}{2}\left(\Psi_{k-1} + \Psi_k\right)$ and Ψ_k is the solution for the k^{th} iteration. The termination condition is $\int (\Psi_{k+1} - \Psi_{k-1,k})^2 d\Omega < \epsilon$, where ϵ is set to $1e^{-16}$ in our case. The square of the ground-state of the solution is the concentration profile of T_4-DNA.

Supplementary Note 3

To show that the plasmid circumferential ring-shaped distribution and pole preference are not sensitive to the choice of the wall depletion function, we investigate the Weeks-Chandler-Andersen (WCA) potential[90] as an alternative model for the plasmid-boundary interaction. The WCA potential is formulated as:

$$V_{\text{WCA}}(r) = \begin{cases} 4\epsilon\left[(\frac{\sigma}{r})^{12} - (\frac{\sigma}{r})^{6} + \frac{1}{4}\right] & \text{if } r < \sigma 2^{\frac{1}{6}} \\ 0 & \text{otherwise} \end{cases}$$

where σ characterizes the effective distance over which the potential decreases from the wall and ϵ characterizes the strength of the potential. By replacing the exponential function in Eq. (1) in the manuscript with the WCA function, we fit the model by the same protocol (maximize the cosine similarity with Nelder-Mead alogrithm[91]). The result is shown in Fig. 7.2. The model matches our experiment qualitatively with the plasmid circumferential ring-shaped distribution and pole preference clear. The position of the segregation peak is captured by our model.

The WCA potential, similar to a hard-wall potential, overestimates the interaction between the plasmid and the cavity boundary, providing an upper limit for the plasmid's radius of gyration. The parameter $\sigma = 202 \pm 2\,\text{nm}$, extracted from cosine similarity fitting. The modeled position distribution and comparison with experiment are shown in Fig. 7.2**a-e**.

The radius of gyration of the plasmid extracted from the model with WCA wall potential gives a upper bound of the actual radius. As shown in Fig. 7.2**f**, for exponential wall potential model, when $r = r_b$, the plasmid will have a potential energy more than $15k_BT$. On the contrary, for model with WCA wall potential function, the plasmid will have a potential energy less than $1k_BT$.

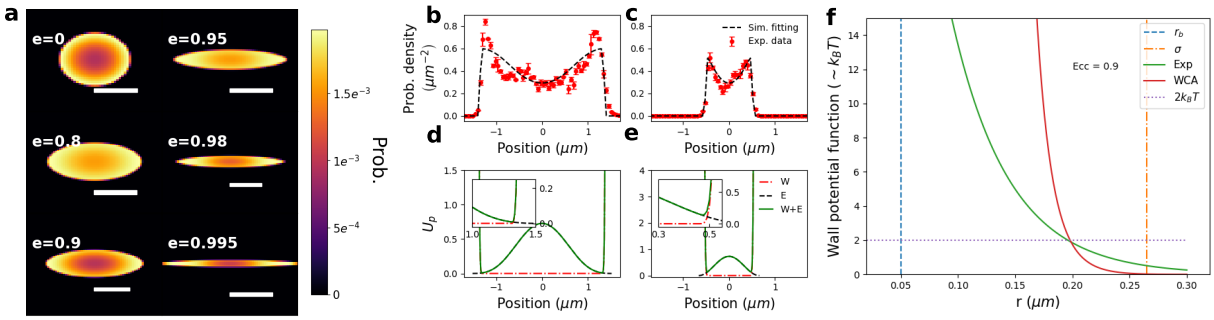

Figure 7.2: Simulation results from the model with WCA wall potential. **a**. Fitted position distribution of the confined plasmid in cavities containing a single T_4-DNA molecule with eccentricity ranging from $e = 0$ to $e = 0.995$. The scale bars from $e = 0$ to $e = 0.995$ correspond to 1 μm, 1 μm, 1.2 μm, 1.2 μm, 1.6 μm and 1.6 μm respectively. **b,c**. Plasmid probability density along the major (**b**) and minor (**c**) axis for $e = 0.9$. Experimental data are shown as red points, with the error bars showing the standard error of the mean of the binned counts (n=3 bins for each point). The center of the error bars denote the mean value of the 3 binned counts. Black dashed lines indicate the resulting fitted model plasmid probability density. **d,e**. Cross-sectional slices of the predicted potential along the major (**d**) and minor (**e**) axis for $e = 0.9$. The red dot-dashed line indicates the wall-potential; the black dashed line indicates the exclusion potential arising from the T_4-DNA; the green solid line indicates the superposition of both potentials. Note that the WCA wall potential is similar to a hard-wall potential, producing a sharper potential profile at the edge compared with the exponential wall-potential. **f**. Comparison of fitted WCA and exponential wall potential model profile. The red solid line indicates the WCA wall potential. The green solid line indicates the exponential wall potential. The blue dashed line indicates $r = r_b$. The orange dot-dashed line indicates $r = \sigma$. The purple dotted line indicates wall potential at $2\,k_BT$.

Supplementary Note 4

Here we compare the experimental and model plasmid distribution in greater detail. Overall the simulation matches our experimental results qualitatively, with the plasmid circumferential ring-shaped distribution and pole preference evident (see Fig. 4**b** and Fig. 5**a** in manuscript). To provide a more quantitative comparison, we present the cross-section of the experimental and theoretical plasmid probability distribution along the major- and minor- axis of the ellipse (see supplementary Fig. 7.3). Note that the positions of the peak plasmid probability agree well with the fitted model. Moreover, the potential difference ΔF between the peak and valley of the free energy barrier, which is reflected by the minor-axis cross-section of the plasmid distribution (see supplementary Fig. 7.3**d**), decreasing as the eccentricity increases, leading to the break of the distribution ring in the middle. We also show the same results for a model generated using the WCA wall potential (see supplementary Fig. 7.4).

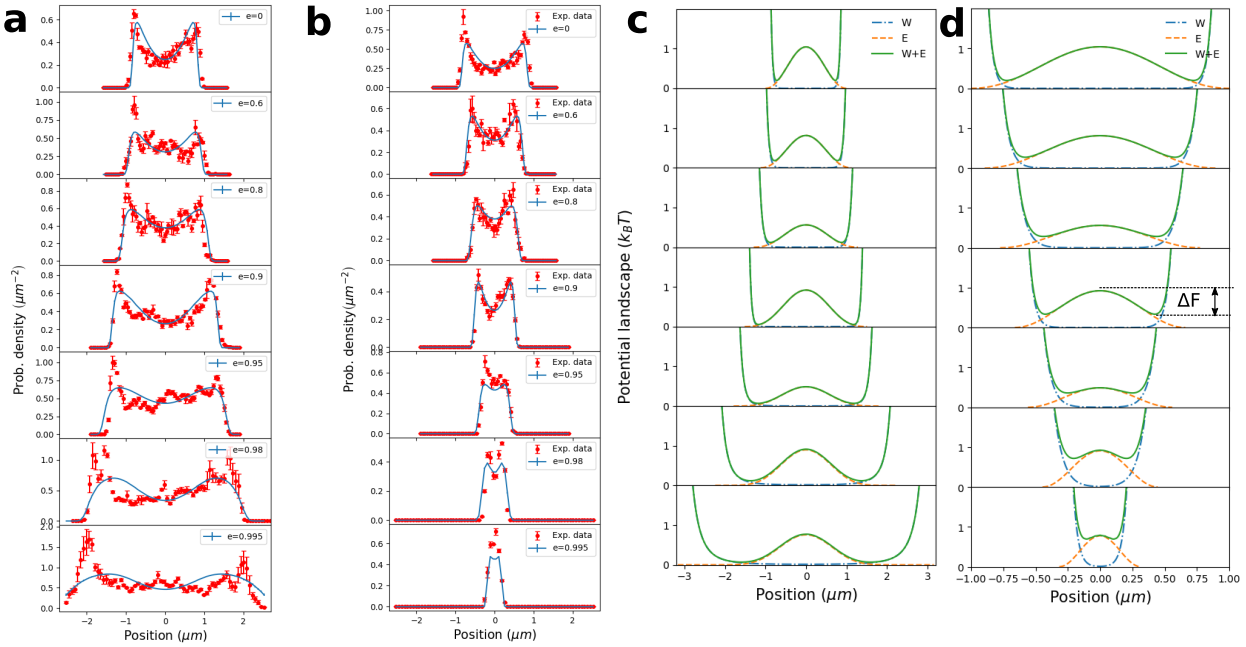

Figure 7.3: The cross-sections of the plasmid distribution and the free energy landscape from experiments and simulations with the exponential wall potential. **a**. Probability density for experimental and model plasmid position along the major axis cross-section. **b**. Probability density for experimental and model plasmid position along the minor axis cross-section. The box over which the cross-section is averaged is three bins wide ($\sim$ 150 nm). The error bars denote the standard error of the mean of the binned counts (n=3 bins for each point). The experimental data is represented by red solid circles with error bar indicating the standard error of the mean for the three adjacent bins. The blue solid line represents the simulation data for the same sampling area as the experimental data. **c**. Potential landscape obtained from simulation for a cross-section taken along the cavity major axis. **d**. Potential landscape obtained from simulation for a cross-section taken along the cavity minor axis. The blue dashed-dot line represents the wall potential. The orange dashed line represents the volume exclusive potential arising from the T_4-DNA. The green solid line gives the total potential (wall plus DNA).

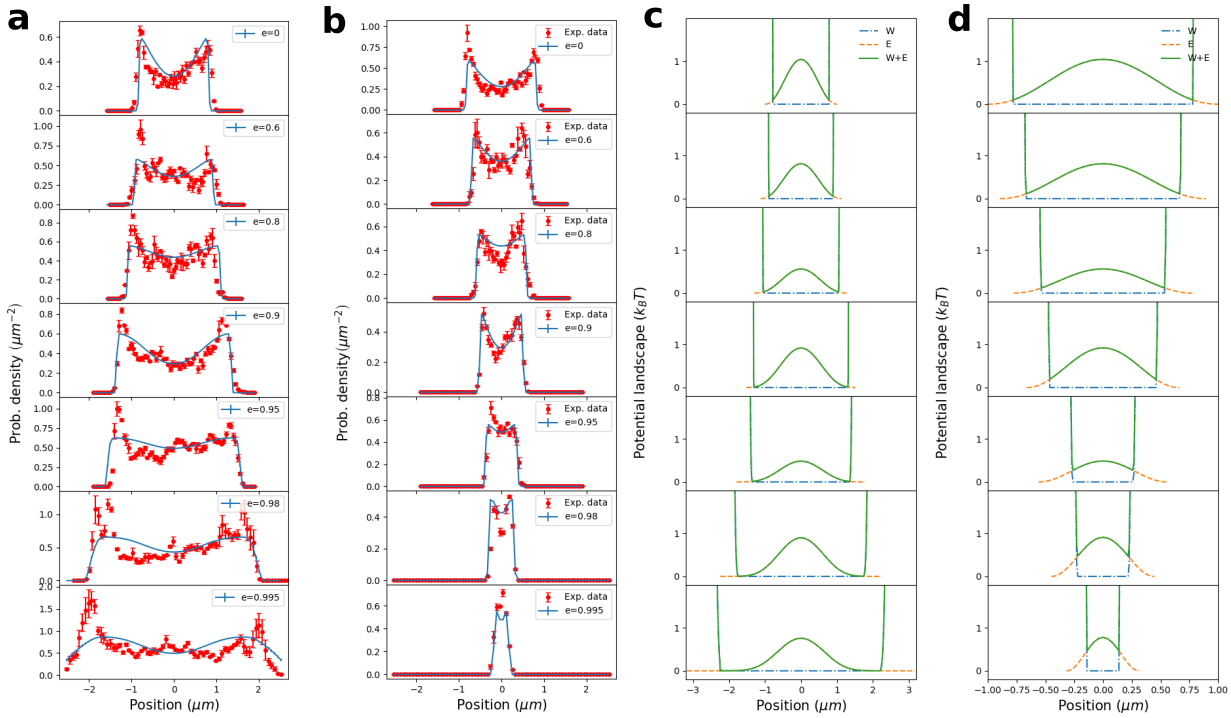

Figure 7.4: The cross-sections of the plasmid distribution and the free energy landscape from experiments and simulations with the WCA wall potential. **a**. Probability density for experimental and model plasmid position along the major axis cross-section. **b**. Probability density for experimental and model plasmid position along the minor axis cross-section. The box over which the cross-section is averaged is three bins wide ($\sim$ 150 nm). The error bars denote the standard error of the mean of the binned counts (n=3 bins for each point). The experimental data is represented by red solid circles with error bar indicating the standard error of the mean for the three adjacent bins. The blue solid line represents the simulation data for the same same sampling area as the experimental data. **c**. Potential landscape obtained from simulation for a cross-section taken along the cavity major axis. **d**. Potential landscape obtained from simulation for a cross-section taken along the cavity minor axis. The blue dashed-dot line represents the wall potential. The orange dashed line represents the volume exclusive potential arising from the T_4-DNA. The green solid line gives the total potential (wall plus DNA).

Supplementary Note 5

We also fit to a cumulative histogram to extract the polar dwell time of the plasmid while confined with T_4-DNA. To account for the short and long-time scale observed in the histogram (see Fig. 6**a** in manuscript), we use a double-exponential model. This describes our experimental data well(see Fig. 7.5).

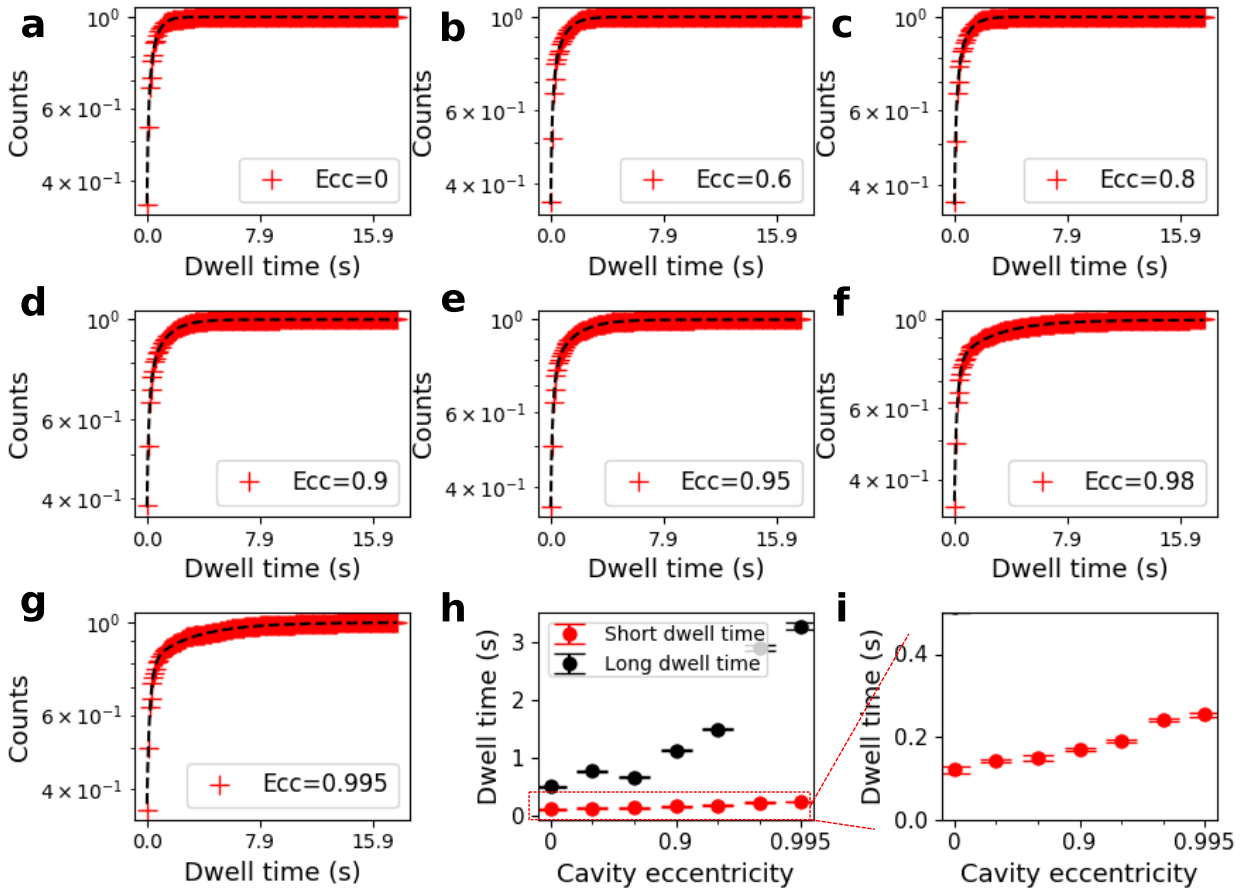

Figure 7.5: The cumulative dwell time fittings for the plasmid–T_4-DNA experiments. **a-g**. We extract the plasmid polar dwell times by fitting the cumulative curve for a double-exponential model to the cumulative plasmid dwell time histogram. Note that the cumulative histograms have been normalized by the total number of counts. The black crosses are the experimental data. The red dashed line is the fitted double-exponential model. **h-i**. The two different time-scales extracted from the double-exponential fitting of the dwell time histogram. The black solid circle indicates the long dwell time and the red solid circle indicates the short dwell time. The errorbars are extracted from the fitting covariance. **i** is a close-up of the graph of panel **h**.

We further investigate the events yielding the two different time scales. To do this, we plot separately the histogram of the plasmid position for events corresponding to the two different time-scales. For short-time scale events, we show the positions of plasmids which stay inside the pole region less than 0.3 s (this upper bound corresponds to the short

average dwell time extracted from double-exponential fitting). For the long-time events, we show the positions of plasmids which stay inside the pole region longer than the corresponding long average dwell time extracted from double-exponential fitting. The results are shown in Fig. 7.6. Note that the events corresponding to the short-time scale are concentrated at the border of the pole region (e.g. $|x| = l/3$), while the long-time scale events are concentrated at the free-energy pocket created by the T_4-DNA and the cavity wall.

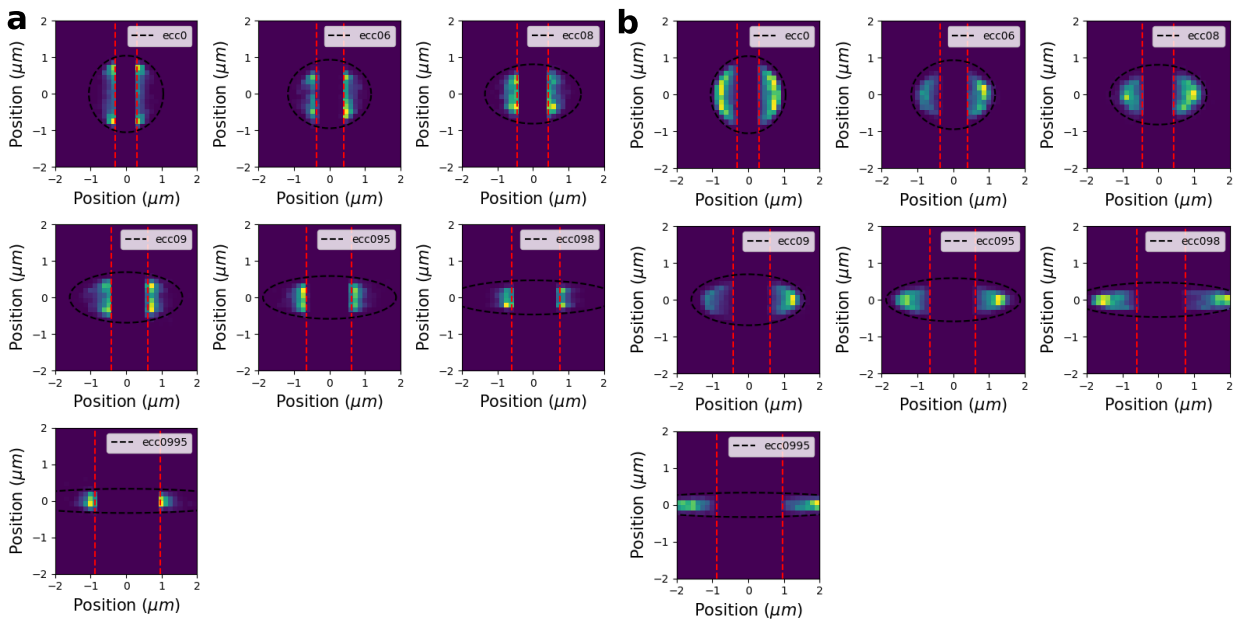

Figure 7.6: Spatial distribution of the short dwell time events and long dwell time events. **a**. Plasmid position distribution for events corresponding to the short time scale (dwell time less than 0.3 s). **b**. Plasmid position distribution for events corresponding to the long time scale (dwell time longer than the long average dwell time extracted from double-exponential fitting).

Supplementary Note 6

We extract the mean-squared displacement (MSD) of the plasmid confined in the cavity with the T_4-DNA. The MSD is shown in Fig. 7.7**a** and is separated into its two orthogonal components along the major-axis (Fig. 7.7**b**) and the minor-axis (Fig. 7.7**c**) of the cavity. Qualitatively, the MSD is dominated by the major-axis component due to its larger spatial extent compared with the minor-axis. The major-axis component of the MSD does not greatly change in the short-time regime (less than 1 s) while the minor-axis component shows a decreasing diffusivity as the eccentricity increases.

The plasmid undergoes sub-diffusion indicated by the scaling exponent $\alpha < 1$, where $\mathrm{MSD}(\tau) \sim t^{\alpha}$. By fitting the MSD for lag time less than 1 s with the least-squared method, we extract α and the result is shown in Fig. 7.7**d**. We denote the corresponding exponents extracted from the orthogonal components as α_{major} and α_{minor}. We observe that α is dominated by α_{major} as the increasing of the eccentricity. α_{major} does not have a obvious trend with the eccentricity (Fig. 7.7**b**), while α_{minor} shows a monotonic decreasing as the eccentricity. The decreasing of the diffusivity agrees with the stronger confinement in the minor-axis direction, inducing a higher average T_4-DNA concentration in minor-axis direction.

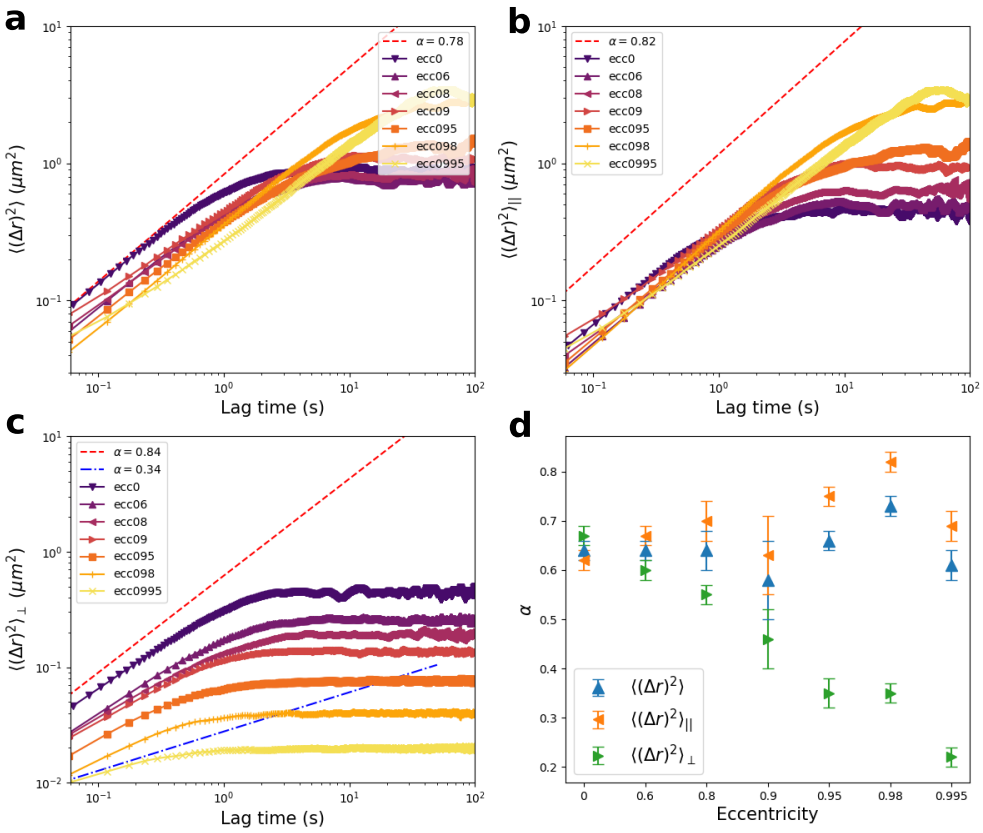

Figure 7.7: Ensemble-averaged MSD of the plasmid confined in the cavity. **a**. The full MSD of the confined plasmid. **b**. The MSD along the cavity major-axis. **c**. The MSD along the cavity minor-axis. The red dashed lines in (**a**,**b**) indicate the α extracted from the fitting averaged over all curves for varying eccentricity. The red dashed line in **c** indicates the scaling exponent for the cavity with eccentricity 0 and the blue dashed line indicates the scaling exponent for the cavity with eccentricity 0.995. **d**. Scaling exponents extracted from fitting to the MSD results. The blue triangles indicate the exponent for full MSD. The orange triangles give the scaling exponent for the MSD major-axis component. The green triangles give the scaling exponent for the minor-axis component. The error bar shows the standard error of the mean of α over captured videos (n is the number of captured videos. $n = 5$ for $e = 0$, $n = 7$ for $e = 0.6$, $n = 8$ for $e = 0.8$, $n = 9$ for $e = 0.9$, $n = 15$ for $e = 0.95$, $n = 9$ for $e = 0.98$, $n = 16$ for $e = 0.995$).

Supplementary Note 7

To determine if the sub-diffusive behavior of the plasmid arises from the structure of the potential landscape, we performed a Monte-Carlo dynamics simulations as a comparison. In this simulation, the 2D free energy landscape was extracted from $F_{\text{CM}}(\mathbf{r}) = -k_B T \log P_{\text{plasmid}}(\mathbf{r})$, where $P_{\text{plasmid}}(\mathbf{r})$ is the fitted probability distribution of the plasmid position in the cavity (i.e. shown in Fig. 5**a** in the manuscript). We then modeled the plasmid's dynamics as Brownian diffusion in potential landscape $F_{\text{CM}}(\mathbf{r})$, which was implemented by performing a random walk in this landscape. Each plasmid was modeled as a random walker making a fixed step of length $a = 0.1\,\mu$m. To determine the step direction, we sampled the local potential for a random walker at a given point $\mathbf{r}$ by making $n_{\text{test}} = 5$ random test steps $\mathbf{r}_i$ with uniform probability around a circle of radius a centered at point $\mathbf{r}$. The potential was evaluated for each of the test steps from the free energy landscape via $U_i = F_{\text{CM}}(\mathbf{r}_i)$, and then a partition function:

$$z_{test} = \sum_{i=1}^{n_{test}} e^{-\frac{U_i}{k_B T}} \tag{7.3}$$

is constructed. The test step for the proceeding simulation move is selected with probability $P_i = e^{-\frac{U_i}{k_B T}}/z_{test}$, which ensures that the resulting equilibrium walker position distribution $P_{\text{walker}}(\mathbf{r})$ is Boltzmann distributed (i.e. $P_{\text{walker}}(\mathbf{r}) \sim e^{-\frac{U(\mathbf{r})}{k_B T}}$). For each cavity eccentricity, we perform 250 runs with 3000 steps. The simulated MSD is shown below:

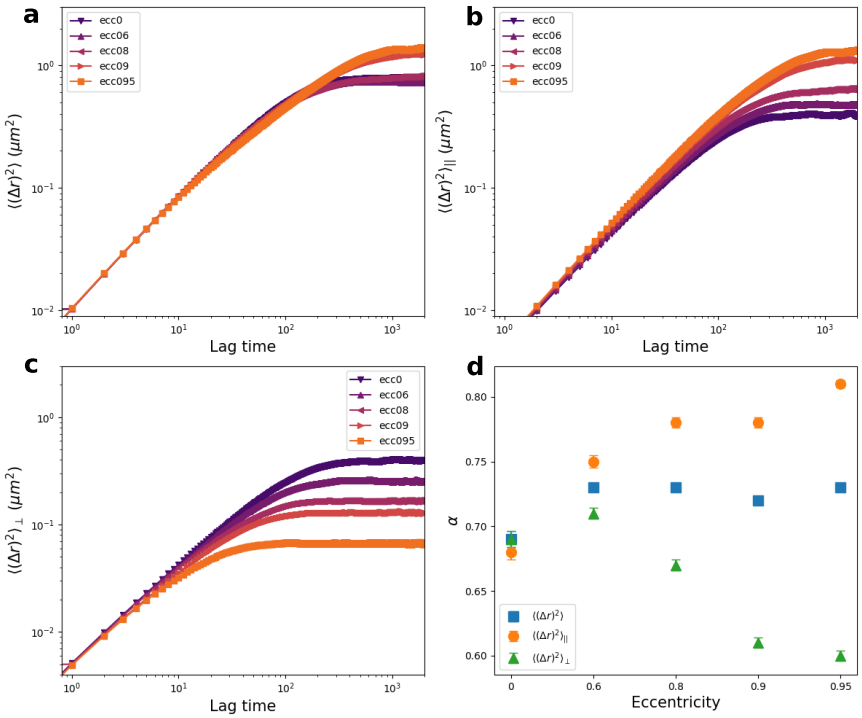

Figure 7.8: Ensemble-averaged MSD of a random walker moving in a 2D free energy landscape $F_{\mathrm{CM}}(\mathbf{r})$. **a**. The full MSD of the 2D random walker. **b**. The MSD along the cavity major-axis. **c**. The MSD along the cavity minor-axis. **d**. Scaling exponents extracted from the Monte-Carlo dynamics simulations. The blue squares indicate the exponent for the full MSD. The orange solid circles indicate the scaling exponent for the major-axis MSD component. The green triangles indicate the exponent for the minor-axis MSD component. The error bar shows the standard-error of the mean of the fitted α over $n = 250$ clips with 3000 steps.

Scaling exponents of the simulated MSD are extracted from the Monte-Carlo (MC) simu-

lation. To ensure that the time range fitted in simulation matches to the time range fitted in experiment ($\sim 1\,\mathrm{s}$), we calibrate our simulation time-scale by matching the simulated MSD times to the experimental result (Fig.7.7). We set the lag time at the point where the simulated MSD reaches 90% of its saturated value equal to the experimental lag time at the same percentage of the saturated value. The calibrated MSD plots and the corresponding exponent fitting is shown in Fig. 7.9: The MSD extracted from the MC simulation has

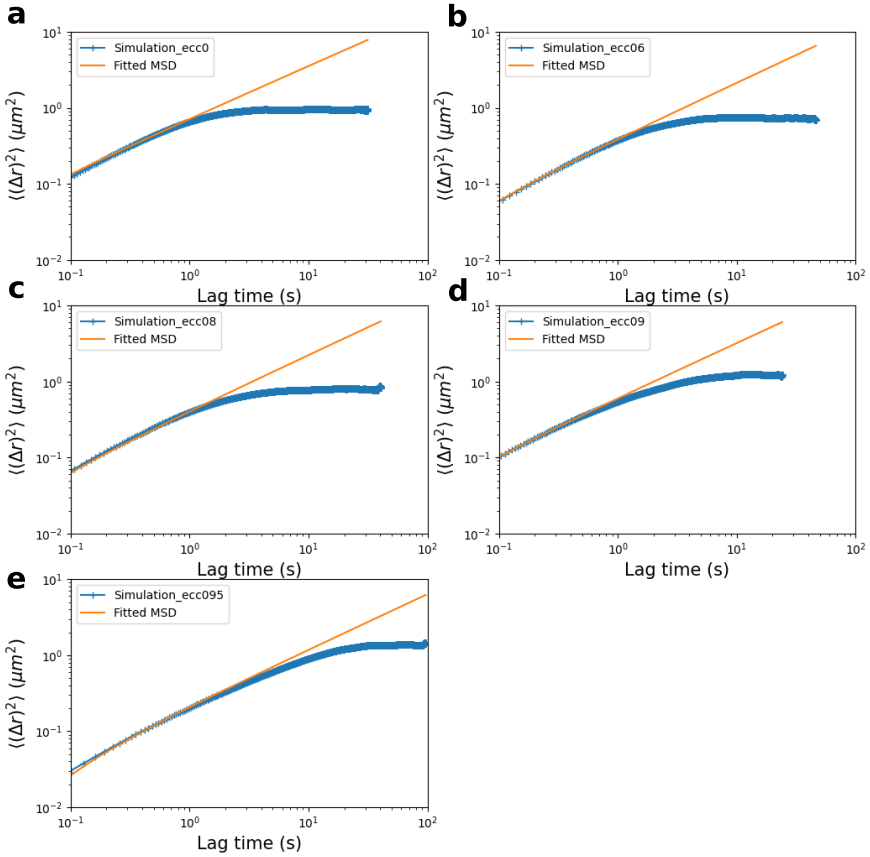

Figure 7.9: MSD of the MC simulation after time-scale calibration (blue lines) and the corresponding fit (orange lines) to extract the diffusion exponent. The fit to simulation is performed over the same short-time regime ($\leq 1\,\mathrm{s}$) as the fit against the experimental MSD. Panels **a–e** correspond to MSD of the MC simulation for cavities with eccentricity $e = 0$ to $e = 0.95$.

a scaling exponent smaller than unity, a sub-diffusive behavior which is observed in our experiment (See Fig. 7.7**d**, Fig. 7.8**d**). We observe that the scaling exponents from the simulation share the same trend of the experimental value. Specifically, $\alpha^{\mathrm{MC}}_{\mathrm{major}}$ increases as the increasing of the eccentricity while $\alpha^{\mathrm{MC}}_{\mathrm{minor}}$ decreases as the increasing of the eccentricity. This suggests that the sub-diffusivity is largely a geometrical effect arising from the non-uniform potential landscape created by the T_4-DNA. However, the exponents from the simulation are larger than the experimental value, particularly for the perpendicular MSD component, indicating that the experiment may be uncovering dynamic behaviour that does not result purely from the particular structure of the free energy landscape. Potentially, this discrepancy arises from how the plasmid diffusion is altered by the local polymer network created by the T_4-DNA molecule, which could alter the plasmid friction factor when the plasmid transits regions of high polymer concentration, such as experienced when the plasmid crosses the cavity central axis.

In addition, to understand the origin of the two time-scales in Fig. 6 of the manuscript, we perform an equivalent dwell time analysis on the data generated by the Monte-Carlo dynamics simulations. The result is shown below:

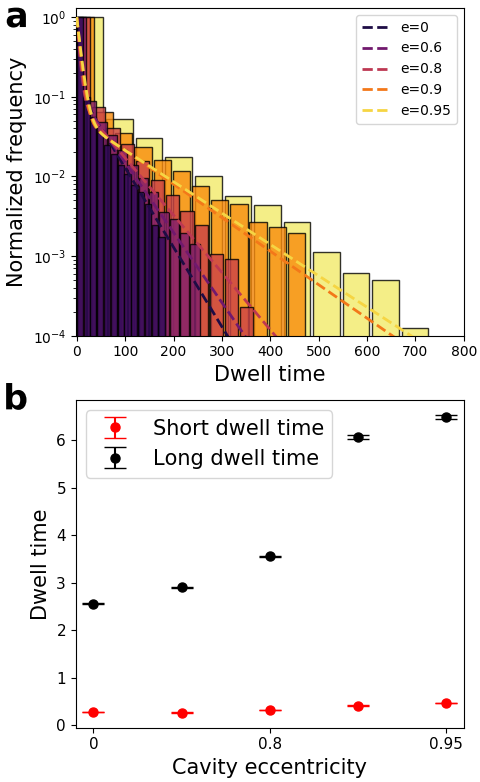

Figure 7.10: The dwell time analysis for the Monte-Carlo dynamics simulations data. **a**. Dwell time histograms of the 2D random walker for cavities of varying eccentricity with double-exponential fits. **b**. Resulting average dwell times extracted from double-exponential fits to the dwell time histograms, with the black circles corresponding to the long average dwell time and the red circles corresponding to the shorter average dwell time. The errorbars are extracted from the fitting covariance.

The qualitative similarity of our experimental results and simulation suggests that the distinct short and long dwell times result from the particular form of the potential landscape.

Supplementary Note 8

The device is fabricated by a three-step lithograph process illustrated in Fig. 7.11. The elliptical cavity is defined by an ebeam lithography procees followed by an RIE process. ZEP520A resist is spun and a thin chromium discharge layer is sputtered. Then the wafer is exposed. After exposure, the chromium layer is removed by chromium etchant and the resist is developed. We use an RIE recipe based on etch parameters suggested by Goyal et al.[82] with which we can produce smooth borofloat surfaces with R_a less than 5% of the etching depth. The microchannel is transferred to the borofloat substrate by the UV lithography process. S1818 photoresist is applied to the substrate, where the elliptical cavities are printed. A contact UV exposure followed by RIE defines the microchannel. The etched borosilicate wafer is bonded to a silicon wafer containing a 100 nm LPCVD silicon nitride film (ordered from the Cornell Nanofabrication facility). The last UV lithograph process with RIE is used to define the access window on the silicon nitride. Lastly, silicon is etched away in KOH solution to release the free-standing membrane in the device center.

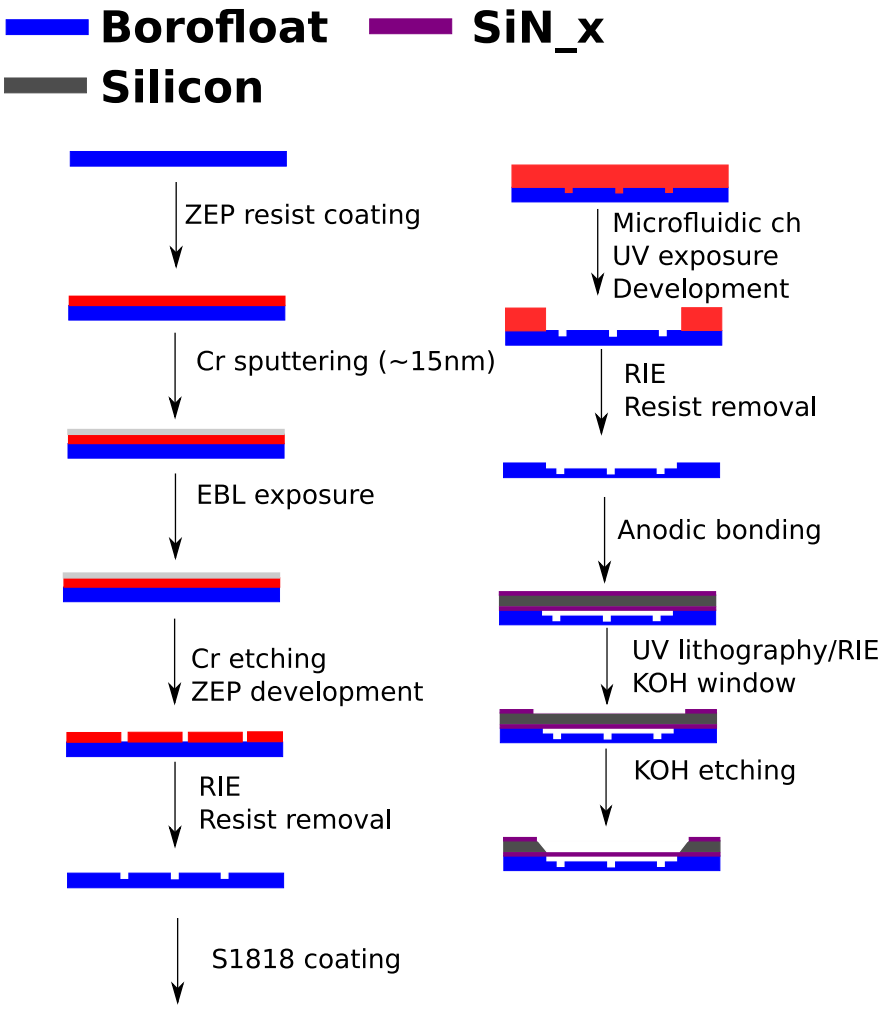

Figure 7.11: Device fabrication work flow. The device dimensions are exaggerated for clarity.

7.2 Supplementary Information for "Multiple Chains Confined in a Nanoscale Cavity: How Entropic Force Alters Plasmid Behavior"

7.2.1 K-Means Clustering Based Multi-particle Tracking

We validate the accuracy of our K-Means clustering based tracking method by compositing artificial plasmid images. We place plasmids randomly within the frame size and note down the actual position of each plasmid. We convolute the plasmid position with the point-spreading function to construct a simulated image. We feed this simulated image to our K-means based tracker. Finally, we compare the actual position with the tracked position visually and calculate the tracking error by averaging the misplacement over 100k frames. The average error for the two plasmids tracking is $0.05\,\mu$m and the average error for the three plasmids tracking is $0.1\,\mu$m. In both case, the error is below the pixel size ($0.11\,\mu$m) of the camera.

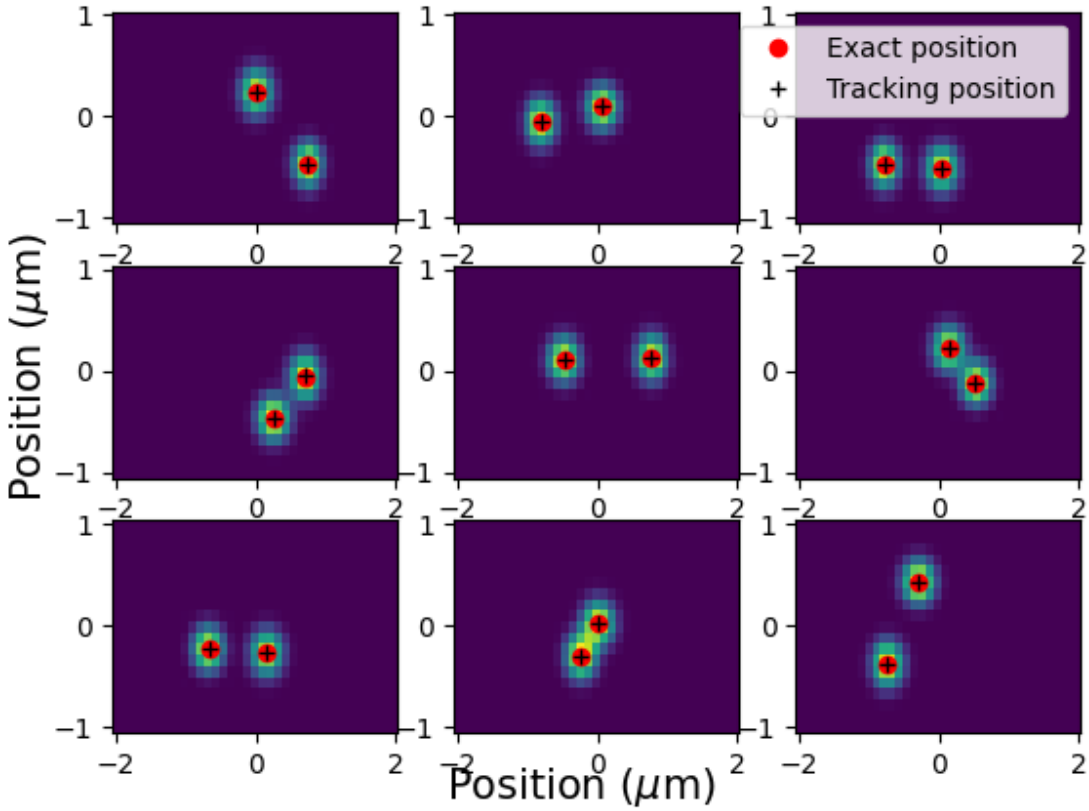

Figure 7.12: K-means clustering based tracking for simulated two plasmids images. The red dots are the actual position of the plasmids. The crosses mark the tracked position.

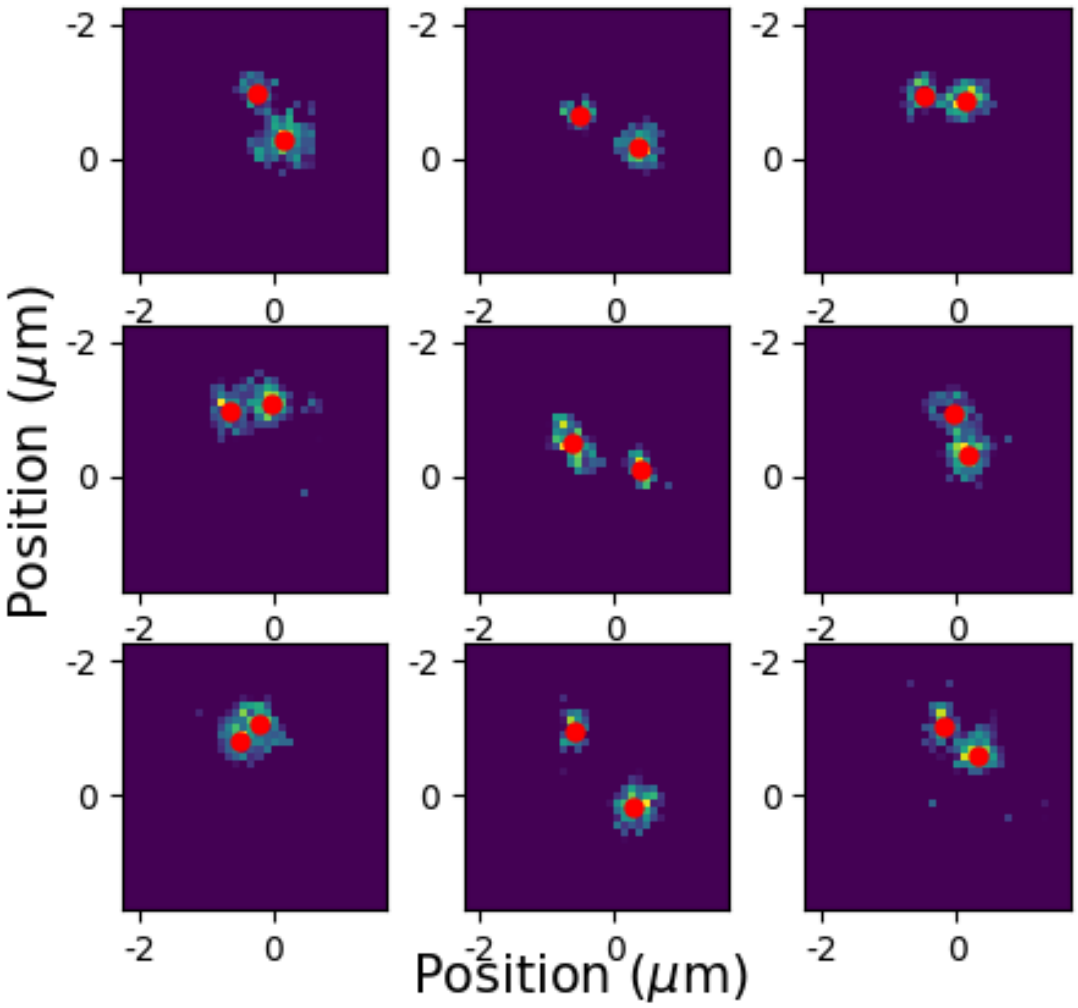

Figure 7.13: K-means clustering based tracking for experimental two plasmids images. The red dots are the tracked positions.

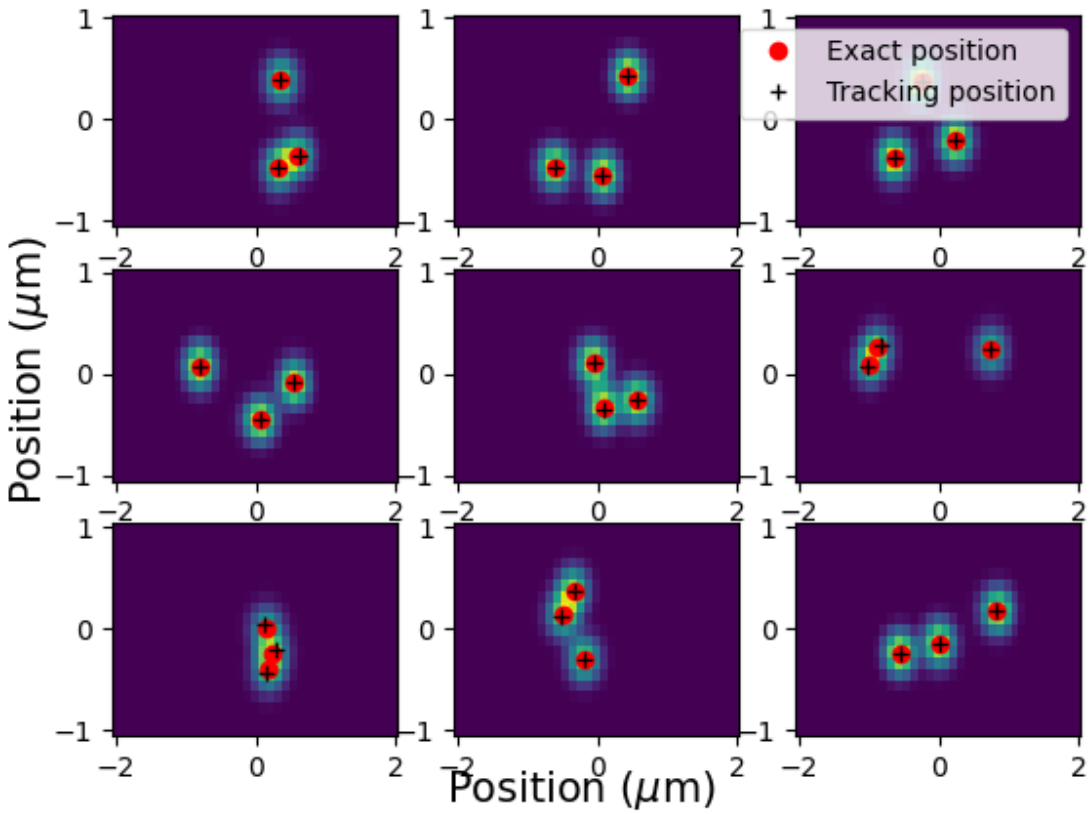

Figure 7.14: K-means clustering based tracking for simulated three plasmids images. The red dots are the actual position of the plasmids. The crosses mark the tracked position.

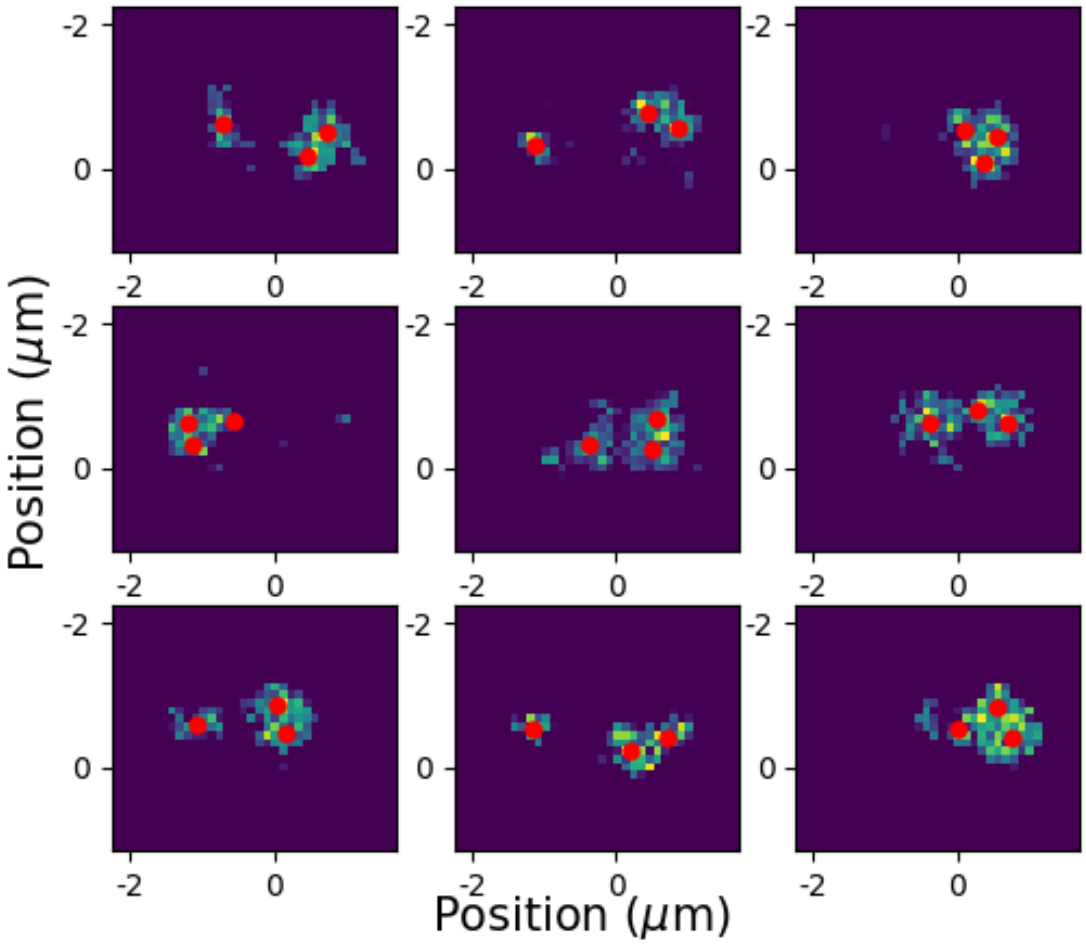

Figure 7.15: K-means clustering based tracking for experimental three plasmids images. The red dots are the tracked positions.

Reference

[1] Michael Rubinstein, Ralph H Colby, et al. *Polymer physics*. Vol. 23. Oxford university press New York, 2003.

[2] Paul M Chaikin, Tom C Lubensky, and Thomas A Witten. *Principles of condensed matter physics*. Vol. 10. Cambridge university press Cambridge, 1995.

[3] Osamu Mishima and H Eugene Stanley. "The relationship between liquid, supercooled and glassy water". In: *Nature* 396.6709 (1998), pp. 329–335.

[4] Stephen Harrington et al. "Liquid-liquid phase transition: Evidence from simulations". In: *Physical Review Letters* 78.12 (1997), p. 2409.

[5] Osamu Mishima and H Eugene Stanley. "Decompression-induced melting of ice IV and the liquid–liquid transition in water". In: *Nature* 392.6672 (1998), pp. 164–168.

[6] James N Glosli and Francis H Ree. "Liquid-liquid phase transformation in carbon". In: *Physical Review Letters* 82.23 (1999), p. 4659.

[7] Yoshinori Katayama et al. "A first-order liquid–liquid phase transition in phosphorus". In: *Nature* 403.6766 (2000), pp. 170–173.

[8] Sarah L Veatch and Sarah L Keller. "Organization in lipid membranes containing cholesterol". In: *Physical review letters* 89.26 (2002), p. 268101.

[9] Clifford P Brangwynne et al. "Germline P granules are liquid droplets that localize by controlled dissolution/condensation". In: *Science* 324.5935 (2009), pp. 1729–1732.

[10] Adam Klosin et al. “Phase separation provides a mechanism to reduce noise in cells”. In: *Science* 367.6476 (2020), pp. 464–468.

[11] Bae-Yeun Ha and Youngkyun Jung. “Polymers under confinement: single polymers, how they interact, and as model chromosomes”. In: *Soft Matter* 11.12 (2015), pp. 2333–2352.

[12] Suckjoon Jun and Andrew Wright. “Entropy as the driver of chromosome segregation”. In: *Nature Reviews Microbiology* 8.8 (2010), p. 600.

[13] Yong Wang, Paul Penkul, and Joshua N Milstein. “Quantitative localization microscopy reveals a novel organization of a high-copy number plasmid”. In: *Biophysical journal* 111.3 (2016), pp. 467–479.

[14] Masao Doi. *Soft matter physics*. Oxford University Press, 2013.

[15] Anthony A Hyman, Christoph A Weber, and Frank Jülicher. “Liquid-liquid phase separation in biology”. In: *Annual Review of Cell and Developmental Biology* 30.1 (2014), pp. 39–58.

[16] Pierre-Gilles De Gennes and Pierre-Gilles Gennes. *Scaling concepts in polymer physics*. Cornell university press, 1979.

[17] Youngkyun Jung et al. “Ring polymers as model bacterial chromosomes: confinement, chain topology, single chain statistics, and how they interact”. In: *Soft Matter* 8.7 (2012), pp. 2095–2102.

[18] James M Polson and Deanna R-M Kerry. “Segregation of polymers under cylindrical confinement: effects of polymer topology and crowding”. In: *Soft Matter* 14.30 (2018), pp. 6360–6373.

[19] Suckjoon Jun, Axel Arnold, and Bae-Yeun Ha. “Confined space and effective interactions of multiple self-avoiding chains”. In: *Physical review letters* 98.12 (2007), p. 128303.

[20] Elizabeth S. Egan, Michael A. Fogel, and Matthew K. Waldor. "Divided genomes: negotiating the cell cycle in prokaryotes with multiple chromosomes". In: *Molecular Microbiology* 56.5 (2005), pp. 1129–1138.

[21] Samuel Million-Weaver and Manel Camps. "Mechanisms of plasmid segregation: Have multicopy plasmids been overlooked?" In: *Plasmid* 75 (2014), p. 27.

[22] Kevin D. Young. "The selective value of bacterial shape". In: *Microbiology and Molecular Biology Reviews* 70.3 (2006), pp. 660–703.

[23] Anthony E. Walsby. "Archaea with square cells". In: *Trends in Microbiology* 13 (2005), p. 193.

[24] Arthur Kornberg, Tania A Baker, et al. *DNA replication*. Vol. 3. Wh Freeman New York, 1992.

[25] Rodrigo Reyes-Lamothe, Emilien Nicolas, and David J Sherratt. "Chromosome replication and segregation in bacteria". In: *Annual review of genetics* 46.1 (2012), pp. 121–143.

[26] G Scott Gordon and Andrew Wright. "DNA segregation: putting chromosomes in their place". In: *Current biology* 8.25 (1998), R925–R927.

[27] Hironori Niki and Sota Hiraga. "Polar localization of the replication origin and terminus in Escherichia coli nucleoids during chromosome partitioning". In: *Genes & development* 12.7 (1998), pp. 1036–1045.

[28] Nancy Kleckner et al. "The bacterial nucleoid: nature, dynamics and sister segregation". In: *Current opinion in microbiology* 22 (2014), pp. 127–137.

[29] Xindan Wang, Paula Montero Llopis, and David Z Rudner. "Organization and segregation of bacterial chromosomes". In: *Nature Reviews Genetics* 14.3 (2013), pp. 191–203.

[30] Juin Kim et al. “A polymer in a crowded and confined space: effects of crowder size and poly-dispersity”. In: *Soft Matter* 11.10 (2015), pp. 1877–1888.

[31] Jamie C Baxter and Barbara E Funnell. “Plasmid partition mechanisms”. In: *Plasmids: biology and impact in biotechnology and discovery* (2015), pp. 133–155.

[32] Rodrigo Reyes-Lamothe et al. “High-copy bacterial plasmids diffuse in the nucleoid-free space, replicate stochastically and are randomly positioned at cell division”. In: *Nucleic Acids Research* 42.2 (2014), pp. 1042–1051.

[33] Jean-Yves Bouet and Barbara E Funnell. “Plasmid localization and partition in Enterobacteriaceae”. In: *EcoSal Plus* 8.2 (2019).

[34] Yong Wang. “Spatial distribution of high copy number plasmids in bacteria”. In: *Plasmid* 91 (2017), pp. 2–8.

[35] Kurt Nordström and Stuart J Austin. “Mechanisms that contribute to the stable segregation of plasmids”. In: *Annual review of genetics* 23.1 (1989), pp. 37–69.

[36] Kurt Nordström and Kenn Gerdes. “Clustering versus random segregation of plasmids lacking a partitioning function: a plasmid paradox?” In: *Plasmid* 50.2 (2003), pp. 95–101.

[37] David K Summers and David J Sherratt. “Multimerization of high copy number plasmids causes instability: ColE 1 encodes a determinant essential for plasmid monomerization and stability”. In: *Cell* 36.4 (1984), pp. 1097–1103.

[38] Youngkyun Jung and Bae-Yeun Ha. “Overlapping two self-avoiding polymers in a closed cylindrical pore: Implications for chromosome segregation in a bacterial cell”. In: *Physical Review E* 82.5 (2010), p. 051926.

[39] Ling Juan Wu et al. “Geometric principles underlying the proliferation of a model cell system”. In: *Nature communications* 11.1 (2020), pp. 1–13.

[40] Baihui Liang et al. "Artificial modulation of cell width significantly affects the division time of Escherichia coli". In: *Scientific reports* 10.1 (2020), pp. 1–9.

[41] Bae-Yeun Ha and Youngkyun Jung. "Polymers under confinement: single polymers, how they interact, and as model chromosomes". In: *Soft Matter* 11 (2015), pp. 2333–2352.

[42] Youngkyun Jung et al. "Interchain ordering and segregation of polymers under confinement". In: *Macromolecules* 45 (2012), pp. 3256–3262.

[43] Tai-Ming Hsu and Yi-Ren Chang. "High-Copy-Number plasmid segregation—single-molecule dynamics in single cells". In: *Biophysical journal* 116.5 (2019), pp. 772–780.

[44] Walter Reisner et al. "Statics and dynamics of single DNA molecules confined in nanochannels". In: *Physical Review Letters* 94.19 (2005), p. 196101.

[45] Walter Reisner et al. "Nanoconfinement-enhanced conformational response of single DNA molecules to changes in ionic environment". In: *Physical review letters* 99.5 (2007), p. 058302.

[46] Lasse H Thamdrup, Anna Klukowska, and Anders Kristensen. "Stretching DNA in polymer nanochannels fabricated by thermal imprint in PMMA". In: *Nanotechnology* 19.12 (2008), p. 125301.

[47] Pawel Utko et al. "Injection molded nanofluidic chips: Fabrication method and functional tests using single-molecule DNA experiments". In: *Lab on a Chip* 11.2 (2011), pp. 303–308.

[48] Walter Reisner et al. "Single-molecule denaturation mapping of DNA in nanofluidic channels". In: *Proceedings of the National Academy of Sciences* 107.30 (2010), pp. 13294–13299.

[49] Jiali Li et al. "DNA molecules and configurations in a solid-state nanopore microscope". In: *Nature materials* 2.9 (2003), pp. 611–615.

[50] Bala Murali Venkatesan and Rashid Bashir. “Nanopore sensors for nucleic acid analysis”. In: *Nature nanotechnology* 6.10 (2011), pp. 615–624.

[51] Marc A Unger et al. “Monolithic microfabricated valves and pumps by multilayer soft lithography”. In: *science* 288.5463 (2000), pp. 113–116.

[52] Daniel J Berard et al. “Convex lens-induced nanoscale templating”. In: *Proceedings of the National Academy of Sciences* 111.37 (2014), pp. 13295–13300.

[53] Min Ju Shon and Adam E Cohen. “Mass action at the single-molecule level”. In: *Journal of the American Chemical Society* 134.35 (2012), pp. 14618–14623.

[54] Walter Reisner, Jonas N Pedersen, and Robert H Austin. “DNA confinement in nanochannels: physics and biological applications”. In: *Reports on Progress in Physics* 75.10 (2012), p. 106601.

[55] Andrew D Bates, Anthony Maxwell, et al. *DNA topology*. Oxford University Press, USA, 2005.

[56] John A Schellman and Dirk Stigter. “Electrical double layer, zeta potential, and electrophoretic charge of double-stranded DNA”. In: *Biopolymers: Original Research on Biomolecules* 16.7 (1977), pp. 1415–1434.

[57] Masao Doi, Samuel Frederick Edwards, and Samuel Frederick Edwards. *The theory of polymer dynamics*. Vol. 73. oxford university press, 1988.

[58] Theo Odijk. “The statistics and dynamics of confined or entangled stiff polymers”. In: *Macromolecules* 16.8 (1983), pp. 1340–1344.

[59] Theo Odijk. “Similarity applied to the statistics of confined stiff polymers”. In: *Macromolecules* 17.3 (1984), pp. 502–503.

[60] Liang Dai et al. “A systematic study of DNA conformation in slitlike confinement”. In: *Soft Matter* 8.10 (2012), pp. 2972–2982.

[61] Ahmed Khorshid et al. “Dynamic compression of single nanochannel confined DNA via a nanodozer assay”. In: *Physical review letters* 113.26 (2014), p. 268104.

[62] Yue Qi et al. “Compression of nanoslit confined polymer solutions”. In: *Macromolecules* 51.2 (2018), pp. 617–625.

[63] Clive AJ Fletcher. “Computational galerkin methods”. In: *Computational galerkin methods*. Springer, 1984, pp. 72–85.

[64] Frédéric Hecht. “New development in FreeFem++”. In: *Journal of numerical mathematics* 20.3-4 (2012), pp. 251–266.

[65] Suckjoon Jun and Bela Mulder. “Entropy-driven spatial organization of highly confined polymers: lessons for the bacterial chromosome”. In: *Proceedings of the National Academy of Sciences* 103.33 (2006), pp. 12388–12393.

[66] Jyotsana Lal, Sunil K Sinha, and Loıc Auvray. “Structure of polymer chains confined in Vycor”. In: *Journal de Physique II* 7.11 (1997), pp. 1597–1615.

[67] Youngkyun Jung et al. “Intrachain ordering and segregation of polymers under confinement”. In: *Macromolecules* 45.7 (2012), pp. 3256–3262.

[68] Tatyana Romantsov, Itzhak Fishov, and Oleg Krichevsky. “Internal structure and dynamics of isolated Escherichia coli nucleoids assessed by fluorescence correlation spectroscopy”. In: *Biophysical journal* 92.8 (2007), pp. 2875–2884.

[69] Shuang Deng, Richard A Stein, and N Patrick Higgins. “Organization of supercoil domains and their reorganization by transcription”. In: *Molecular microbiology* 57.6 (2005), pp. 1511–1521.

[70] Kyle JM Bishop et al. “Nanoscale forces and their uses in self-assembly”. In: *small* 5.14 (2009), pp. 1600–1630.

[71] Ce Zhang et al. “Macromolecular crowding induced elongation and compaction of single DNA molecules confined in a nanochannel”. In: *Proceedings of the National Academy of Sciences* 106.39 (2009), pp. 16651–16656.

[72] PD Kaplan et al. “Entropically driven surface phase separation in binary colloidal mixtures”. In: *Physical Review Letters* 72.4 (1994), p. 582.

[73] PD Kaplan, Luc P Faucheux, and Albert J Libchaber. “Direct observation of the entropic potential in a binary suspension”. In: *Physical review letters* 73.21 (1994), p. 2793.

[74] Daniel L Sober and John Y Walz. “Measurement of long range depletion energies between a colloidal particle and a flat surface in micellar solutions”. In: *Langmuir* 11.7 (1995), pp. 2352–2356.

[75] AD Dinsmore, AG Yodh, and DJ Pine. “Entropic control of particle motion using passive surface microstructures”. In: *Nature* 383.6597 (1996), pp. 239–242.

[76] AD Dinsmore et al. “Hard spheres in vesicles: curvature-induced forces and particle-induced curvature”. In: *Physical Review Letters* 80.2 (1998), p. 409.

[77] Yoori Kim et al. “Nanochannel confinement: DNA stretch approaching full contour length”. In: *Lab on a Chip* 11.10 (2011), pp. 1721–1729.

[78] Jing Tang et al. “Revisiting the conformation and dynamics of DNA in slitlike confinement”. In: *Macromolecules* 43.17 (2010), pp. 7368–7377.

[79] Cees Dekker. “Solid-state nanopores”. In: *Nanoscience And Technology: A Collection of Reviews from Nature Journals* (2010), pp. 60–66.

[80] Zhifu Yin and Helin Zou. “Experimental and numerical study on PDMS collapse for fabrication of micro/nanochannels”. In: *Journal of Electrical Engineering* 67.6 (2016), p. 414.

[81] Marjan Shayegan et al. “Probing inhomogeneous diffusion in the microenvironments of phase-separated polymers under confinement”. In: *Journal of the American Chemical Society* 141.19 (2019), pp. 7751–7757.

[82] Abhijat Goyal, Vincent Hood, and Srinivas Tadigadapa. “High speed anisotropic etching of Pyrex® for microsystems applications”. In: *Journal of non-crystalline solids* 352.6-7 (2006), pp. 657–663.

[83] Imman I Hosseini et al. “Nanofluidics for simultaneous size and charge profiling of extracellular vesicles”. In: *Nano Letters* 21.12 (2021), pp. 4895–4902.

[84] Olivia Goode et al. “Heterologous protein expression favors the formation of protein aggregates in persister and viable but nonculturable bacteria”. In: *ACS Infectious Diseases* 7.6 (2021), pp. 1848–1858.

[85] Frederic D Schramm, Kristen Schroeder, and Kristina Jonas. “Protein aggregation in bacteria”. In: *FEMS microbiology reviews* 44.1 (2020), pp. 54–72.

[86] James A Sawitzke and Stuart Austin. “Suppression of chromosome segregation defects of Escherichia coli muk mutants by mutations in topoisomerase I”. In: *Proceedings of the National Academy of Sciences* 97.4 (2000), pp. 1671–1676.

[87] Victor F Holmes and Nicholas R Cozzarelli. “Closing the ring: links between SMC proteins and chromosome partitioning, condensation, and supercoiling”. In: *Proceedings of the National Academy of Sciences* 97.4 (2000), pp. 1322–1324.

[88] Erik D Andrulis et al. “Esc1, a nuclear periphery protein required for Sir4-based plasmid anchoring and partitioning”. In: *Molecular and cellular biology* 22.23 (2002), pp. 8292–8301.

[89] Jack W Szostak, David P Bartel, and P Luigi Luisi. “Synthesizing life”. In: *Nature* 409.6818 (2001), pp. 387–390.

[90] Hans C Andersen, John D Weeks, and David Chandler. “Relationship between the hard-sphere fluid and fluids with realistic repulsive forces”. In: *Physical Review A* 4.4 (1971), p. 1597.

[91] Pauli Virtanen et al. “SciPy 1.0: fundamental algorithms for scientific computing in Python”. In: *Nature methods* 17.3 (2020), pp. 261–272.